Measurement of the Muon Decay Asymmetry Parameter

With the *TWIST* Spectrometer

by

Blair Jamieson

B.A.Sc., The University of British Columbia, 1997
M.Sc., The University of British Columbia, 1999
B.Ed., The University of British Columbia, 2000

A THESIS SUBMITTED IN PARTIAL FULFILMENT OF
THE REQUIREMENTS FOR THE DEGREE OF

Doctor of Philosophy

in

The Faculty of Graduate Studies

(Physics)

The University Of British Columbia

January 24, 2006

Abstract

Muon decay, a purely leptonic decay, is a relatively simple interaction to study when looking for physics not explained by the standard theory of electroweak interactions. In particular, the muon decay asymmetry parameter is directly related to the degree to which weak interactions violate parity, or mirror, symmetry. At the Tri-University Meson Facility (TRIUMF), the TRIUMF Weak Interaction Symmetry Test ($\mathcal{TWIST}$) spectrometer was used to measure the energy and angle spectrum of decay positrons from muon decay. By measuring a large part of the muon decay spectrum, $\mathcal{TWIST}$ can simultaneously determine three of the muon decay parameters with a high degree of accuracy. This thesis presents the first direct $\mathcal{TWIST}$ measurement of the muon decay asymmetry parameter $P_\mu\xi$ which was determined to be 1.0003 $\pm$0.0006(stat) $\pm$0.0038(syst). The uncertainty on this measurement is a factor of two lower than a previous direct measurement. This measurement is consistent with the standard model of particle physics, and further constrains physics beyond the standard model.

Blair Jamieson
jamieson@triumf.ca

Contents

List of Tables

List of Figures

Acknowledgements

If it was not for the hard work and encouragement of my family this work would never have been finished. My parents and in-laws were very helpful in providing baby sitting while I wrote this thesis. My wife has been very patient with me as I have been distracted with finishing this degree.

Thank you to everyone in the $\mathcal{TWIST}$ collaboration who made this experiment possible. You have all been very helpful and thoughtful about various aspects of making this measurement. Special thanks are due to M. Hasinoff, D. Mischke, C. Gagliardi and M. Nozar for helping with editing this thesis on short notice.

This work was supported by a grant from the Natural Sciences and Engineering Research Council (NSERC) of Canada, and the US Department of Energy. Results were made possible by the use of WestGrid computing facility (www.westgrid.ca).

Part I

Introduction, Physics Motivation and Apparatus

Chapter 1

Introductory Topics

This thesis describes a measurement of the muon decay parameter $P_\mu\xi$, which is the product of the polarization of the decaying muon, P_μ, and the muon decay asymmetry parameter, ξ, that measures the strength of the asymmetry in decay angle of the positrons from muon decay.

Part I of this thesis is divided into two chapters. The first chapter begins with the history of muon discovery, followed by descriptions of: how muons are produced, where this measurement fits into the standard model (SM), muon decay, previous measurements of $P_\mu\xi$, how $P_\mu\xi$ is related to the asymmetry, particle energy loss, and physics motivation for the measurement. In the second Chapter, the apparatus used for the measurement of $P_\mu\xi$ is detailed.

Part II describes the analysis strategy, data used for the measurement, simulations needed to make the measurement, and estimates and descriptions of the systematic uncertainties associated with the measurement of $P_\mu\xi$.

Part III presents the results of the measurement, discusses the physics implications of the measurement, and states the conclusions.

1.1 Discovery of the Muon

Mu mesons, now called muons (μ), were first discovered in cosmic rays in 1936 by Carl D. Anderson and Seth Neddermeyer who were looking for the Yukawa particle[1]. The Yukawa particle had been predicted a year earlier as the mediator of the strong force holding nucleons (protons, neutrons) in the nucleus[2].

The Yukawa particle was to carry the force between nuclei. We now know that the force carrier can be thought of as a pion or rho meson, while the fundamental strong force carriers are the colour charged neutral gluons being exchanged between colour charged quarks. The mass of the muon is close to that predicted for the Yukawa particle, but did not have the right properties to be the Yukawa particle.

Tomonaga and Akari had predicted that slow negatively charged muons would be absorbed by nuclei through strong interactions, and that positively charged muons would be repelled by the Coulomb repulsion and eventually decay in matter [3]. Contrary to this prediction, an experiment by Conversi *et al.* found that negative cosmic ray, μ^-, "mesons" decay in carbon [4]. Fermi, Teller, and Weisskopf found that muon absorption in lead was 12 orders of magnitude too small for it to be the Yukawa meson. The Yukawa meson was discovered and named the pion in 1947 by C.F. Powell [5].

Muons were reclassified as leptons based on their similarity to electrons (but 200 times

heavier). At the time they were thought of as very odd. All of the things that everyday matter was made of could be explained with protons, neutrons, electrons, photons, and the pion. The confusion over how the muon fit in was stated succinctly by I.I. Rabi when he said, "Who ordered that", in reference to the muon.

1.2 Muon Production

In the 1950s pions and muons were being produced by colliding high energy protons with material. This section reviews how muons are produced at particle accelerators like TRIUMF (Tri-University Meson Facility).

Mesons have been produced and observed in large numbers in laboratories where high-energy particle collisions can be achieved with the aid of a particle accelerator. It is now known that each type of meson consists of a quark bound to an anti-quark. Of course the quark and anti-quark do not have to be of the same type, and in some cases the meson is a superposition of two different quark anti-quark states. For example the η meson is [6]:

$$|\eta >= \frac{1}{\sqrt{3}}|\bar{u}u + \bar{d}d - \bar{s}s > . \tag{1.1}$$

Protons must have enough energy to overcome the Coulomb (electric charge) repulsion from the nuclei in the nucleus of the atom so that the protons can get close enough to exchange gluons with enough energy to produce a pion. Figure 1.1a shows the two up quarks and one down quark in each proton, where one proton has an energy of 500 MeV (as is the case at the TRIUMF cyclotron), and the other proton is in a nucleus.

In quantum chromodynamics (QCD), the gluon acts as the colour force carrier between quarks. An overview of QCD is presented in Section 1.3.2. Quarks and gluons can only be found in colourless combinations. The fact that individual quarks cannot be observed is explained by asymptotic freedom, where the quarks are confined to colourless combinations. If you strike a nucleon hard enough, rather than extracting a bare quark, colourless combinations of quarks are produced (mesons and baryons). The process of creating a pion and neutron in a ^{12}C target is shown schematically in Figure 1.1b:

$$p + p \rightarrow \pi^+ + p + n. \tag{1.2}$$

In this pion production reaction, a proton in a ^{12}C nucleus is transformed into a neutron thereby transforming that atom into ^{12}B as in Figure 1.1c. It should be noted that most pion production is via inelastic scattering off of the whole nucleus (quasi-elastic scattering) rather than by converting ^{12}C into ^{12}B.

The muons are produced in π^+ decay, via a virtual W boson, into a μ^+, $\bar{\nu}_e$ and a ν_μ ($\pi^+ \rightarrow \mu^+ \nu_\mu$).

Details on muon decay are in Section 1.4, and elaboration on the spin and polarization of muons from pion decay is in Section 1.5.

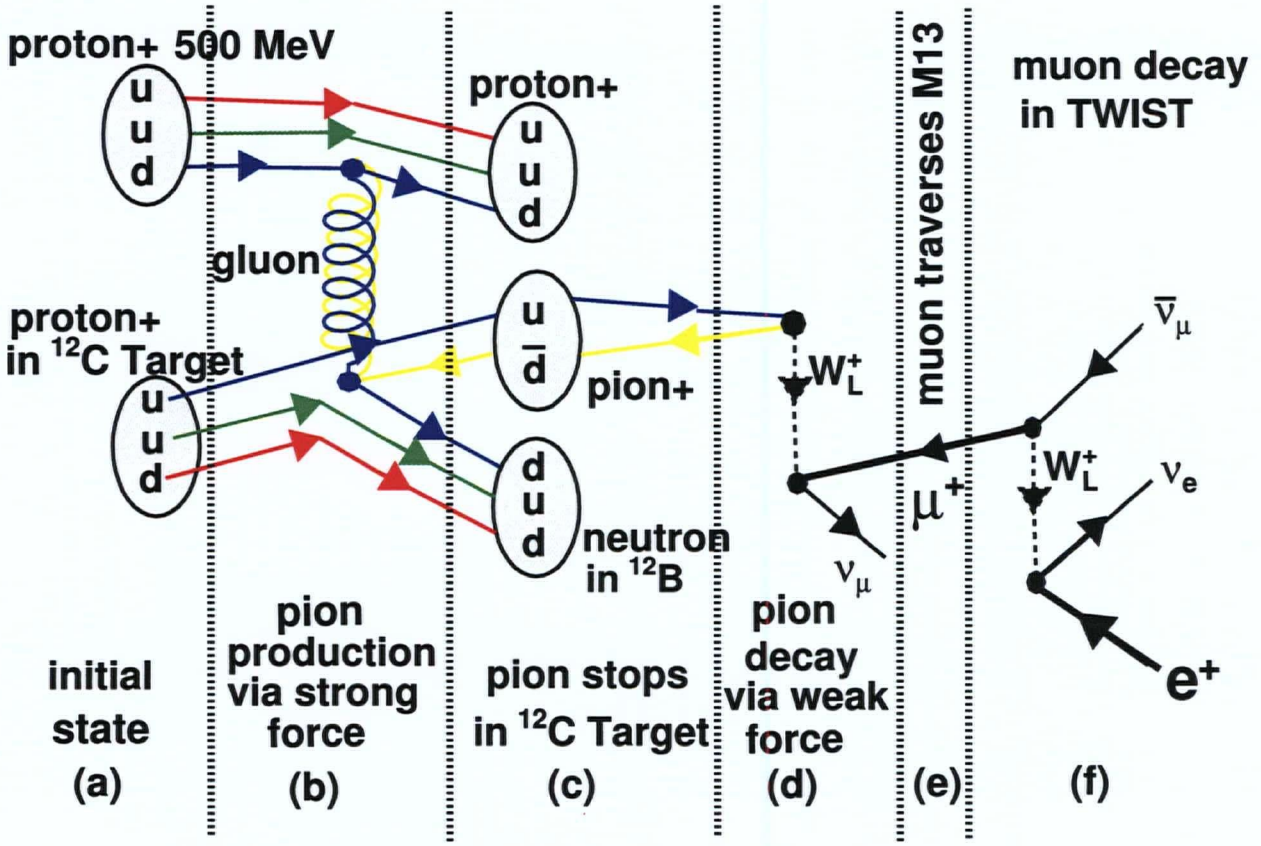

Figure 1.1: One possible standard model picture of muon production and decay. (a) Shows the colourless combination of quarks making up a proton in a ^{12}C nucleus, and a proton with 500 MeV of energy. (b) The blue down quark of the energetic proton emits a blue/anti-blue gluon which turns into an anti-blue anti-down quark and blue down quark inside the proton in ^{12}C. (c) In this picture the proton is split into a π^+ and a neutron in ^{12}B. Usually the pion is produced by quasi-elastic collisions leaving the ^{12}C intact. (d) The π^+ decays with a mean lifetime of 26 ns, via a virtual W boson, into a μ^+, anti-electron neutrino and a muon neutrino. (e) The muon momentum is selected by the combination of dipoles and quadrupoles that make up the M13 channel at TRIUMF. This selects muons with momentum 29.6 MeV/c $\pm$0.2 MeV/c, which is near the 29.87 MeV/c of muons that come from the decay of pions at rest. (f) The muon stops at the target in the center of the $\mathcal{TWIST}$ detector and decays with a mean lifetime of 2.197 μs into an anti-muon neutrino and a W boson. The W decays into an electron neutrino and a positron.

1.3 The Standard Model of Particle Physics

The standard model of particle physics is a combination of the Glashow Weinberg Salam (GWS) and quantum chromodynamic (QCD) models describing particle interactions. It is the simplest model capable of explaining all experimental data in particle physics down to 10^{-19} m. General relativity (GR) is not part of the standard model, but is the framework that describes the only other known force in nature (gravity). The GWS model describes the electromagnetic and weak nuclear forces, QCD governs the strong force, and GR provides a description of the gravitational force.

The relative characteristics of the forces described by these models are shown in Table 1.1. One goal of particle physics is to unify these three models of four forces into a single coherent model that describes nature. The GWS model includes unification of the electromagnetic and weak interactions.

Interaction	Mediator	Relative Strength	Theory
Strong	$g_{i=1...8}$ (gluons)	1	Chromodynamics
Electromagnetic	γ (photon)	10^{-3}	Electrodynamics
Weak	$W^{\pm}$, Z^{o}	10^{-13}	Flavourdynamics
Gravitational	Graviton	10^{-42}	Geometrodynamics

Table 1.1: Force carrier, relative strength, and theory describing the interactions [7].

This section outlines the elementary particles of the standard model and their interactions.

1.3.1 Elementary Particles

The elementary point-like particles of the standard model are quarks, leptons, and force-carrying particles. The particles can be grouped into three different mass hierarchies called families. The lowest mass family makes up all of ordinary matter (and antimatter). The particles in the lowest mass family are the electron, e^{-}, the electron neutrino, ν_e, the up quark, u, down quark, d, and their antiparticles. The second family consist of the muon, μ^{-}, the muon neutrino, ν_μ, the charm quark, c, and the strange quark, s. The heaviest family includes the tau, τ, the tau neutrino, ν_τ, the top quark, t, and the bottom quark b. The three families in order of increasing mass are:

$$\begin{array}{ccc} 1 & 2 & 3 \\ \begin{pmatrix} e^{-} \\ \nu_e \end{pmatrix} & \begin{pmatrix} \mu^{-} \\ \nu_\mu \end{pmatrix} & \begin{pmatrix} \tau^{-} \\ \nu_\tau \end{pmatrix} \\ \begin{pmatrix} u \\ d \end{pmatrix} & \begin{pmatrix} c \\ s \end{pmatrix} & \begin{pmatrix} t \\ b \end{pmatrix} \end{array} \tag{1.3}$$

Each particle has a set of unique conserved quantities which are labeled by its quantum numbers. A minimal set of quantum numbers are the baryon number, lepton number, charge, and spin. All of the force carrier particles have integer spin, $\hbar$, which makes them bosons, and all of the quarks and leptons have half integer spin, $\hbar/2$. Quarks have baryon number $\frac{1}{3}$ and a lepton number of 0, while leptons have baryon number 0 and lepton number 1. The u(d) type quarks carry an electric charge of $+\frac{2}{3}(-\frac{1}{3})$ while the $e^-(\nu_e)$ carries an electric charge of $-1(0)$.

For each of the elementary point-like fermions there exists a spin $\frac{1}{2}\hbar$ particle of identical mass but opposite baryon number, lepton number and electric charge. These are designated anti-particles and are either labeled with an overbar or as the opposite charge (ie. $\bar{u}$ and e^+). A well known problem in particle physics is the antimatter asymmetry of the universe, meaning that the universe has been observed to have $\sim 10^9$ more matter than antimatter.

QCD and electroweak interactions are discussed in more detail in the following sections since they are more relevant to this thesis.

1.3.2 Quantum Chromodynamics

QCD is the standard model description of the strong nuclear force in terms of quarks and gluons. It is based on the gauge group $SU(3)_C$ where the quarks carry a colour charge, R (red), G (green) or B (blue).

Quarks interact by the exchange of spin 1 gauge bosons called gluons, g_i. Gluons carry a combination of colour and anticolour, and only interact with colour carrying particles: ie. quarks and other gluons. There are eight varieties of gluons corresponding to the eight possible combinations that carry colour [7]. A ninth possible combination, carries no colour, so it cannot be exchanged between quarks or couple to other gluons. Leptons do not carry colour, so they do not participate in strong nuclear interactions.

The perturbative calculations for electroweak interactions that can be done in terms of Feynman diagrams fail for low energy QCD. This is because the expansion of the matrix elements in terms of the strength of the strong force, α_s^2, diverge because $\alpha_s > 1$. In QCD, the strong force is thought of as a spring-like force between quarks. If the quarks are close together, the spring is relaxed, and there is no force pulling on the quarks. If the quarks are pulled apart, the "spring" is stretched and the quarks are pulled back together. To do calculations for low energy QCD, different models and more complex calculations are needed. This is the topic of Lattice QCD, and will not be discussed any further here.

1.3.3 Electroweak Interaction

The GWS Model is based on the gauge group $SU(2)_L \times U(1)_Y$. In this model, an explicit left-right asymmetry is introduced to account for the observed parity violation. Left-handed particles (right-handed antiparticles) transform as doublets under $SU(2)$ while right-handed particles (left-handed antiparticles) are singlets as follows:

$$\chi_L = \begin{pmatrix} f \\ f' \end{pmatrix}_L, \quad \chi_R = f_R, \text{ and } \quad \chi'_R = f'_R. \tag{1.4}$$

The first family of fermion left-handed doublets consists of the up- and down-quark $(u,d)_L$, the electron and electron neutrino $(\nu_e, e)_L$. The particles in the first family of right-handed singlets are u_R, d_R, e_R, and ν_{eR}.

Symmetries of the model include the isospin (T) and hypercharge (Y). The electric charge of particles is a combination of these symmetries defined by $q = T_3 + \frac{Y}{2}$. The electroweak quantum numbers for the elementary particles are shown in Table 1.2.

Quark	T	T_3	Y	$q\ (T_3 + \frac{Y}{2})$
u_L	$\frac{1}{2}$	$\frac{1}{2}$	$\frac{1}{3}$	$\frac{2}{3}$
d_L	$\frac{1}{2}$	$-\frac{1}{2}$	$\frac{1}{3}$	$-\frac{1}{3}$
u_R	0	0	$\frac{4}{3}$	$\frac{2}{3}$
d_R	0	0	$-\frac{2}{3}$	$-\frac{1}{3}$
Lepton				
e_L^-	$\frac{1}{2}$	$-\frac{1}{2}$	-1	-1
e_R^-	0	0	-2	-1
ν_e	$\frac{1}{2}$	$\frac{1}{2}$	-1	0

Table 1.2: Quantum numbers for the first family particles that interact via the electroweak force.

The electroweak part of the standard model Lagrangian is given by:

$$\mathcal{L}_{EW} = \sum_k i\bar{\chi}_k \gamma_\mu D^\mu \chi_k - \tfrac{1}{4} W^{j\mu\nu} W^j_{\mu\nu} - \tfrac{1}{4} B^{\mu\nu} B_{\mu\nu}, \tag{1.5}$$

where,

$$\begin{aligned} D_\mu &= \partial_\mu - ig\vec{\sigma}/2 \cdot \vec{W}_\mu - ig'\tfrac{Y}{2} B_\mu, \\ W^j_{\mu\nu} &= \partial_\mu W^j_\nu - \partial_\nu W^j_\mu + g\epsilon^{jkl} W^k_\mu W^l_\nu, \text{ and} \\ B_{\mu\nu} &= \partial_\mu B_\nu - \partial_\nu B_\mu. \end{aligned} \tag{1.6}$$

W^j_μ is an $SU(2)$ vector gauge field and B_μ is a $U(1)$ gauge field, g and g' are coupling constants for the weak interaction, $\vec{\sigma}$ are the Pauli spin matrices, and χ_L and ψ are the vector fields. After spontaneous symmetry breaking, the gauge fields can be related to the physically observed mass eigenstates, $W^\pm$ (charged weak bosons), Z^o (neutral weak boson) and A (photon) via:

$$W^\pm_\mu = \sqrt{\frac{1}{2}}(W^1_\mu \mp iW^2_\mu),$$

$$\begin{aligned} Z^o_\mu &= \cos\theta_W W^3_\mu - \sin\theta_W B_\mu, \text{ and} \\ A_\mu &= \sin\theta_W W^3_\mu + \cos\theta_W B_\mu. \end{aligned} \tag{1.7}$$

θ_W is the experimentally determined weak angle ($\sin\theta_W = tan^{-1}(g'/g) \approx 0.23$) [8]. Furthermore, the couplings g and g' can be expressed in terms of the electromagnetic coupling, e, and the weak angle,

$$g = \frac{e}{\sin\theta_W} \qquad \text{and} \qquad g' = \frac{e}{\cos\theta_W}. \tag{1.8}$$

In the GWS model the charged weak bosons couple only to left-handed particles (right-handed antiparticles). Due to the observation of only left-handed weak interactions it is said that parity, or mirror symmetry, is maximally violated in weak interactions.

In Equation 1.3 the particles were labeled as if the weak eigenstates were the mass eigenstates. In general, the weak and mass eigenstates should be related by a rotation matrix so the mass eigenstates d, s and b in Equation 1.3 should be replaced by the weak eigenstates d', s' and b', respectively.

The rotation matrix for quarks is known as the Cabibbo-Kobayashi-Maskawa (CKM) matrix. The CKM matrix is nearly diagonal, and has been experimentally measured:

$$\begin{pmatrix} d' \\ s' \\ b' \end{pmatrix} = \begin{pmatrix} V_{ud} & V_{us} & V_{ub} \\ V_{cd} & V_{cs} & V_{cb} \\ V_{td} & V_{ts} & V_{tb} \end{pmatrix} \begin{pmatrix} d \\ s \\ b \end{pmatrix} \tag{1.9}$$

$$= \begin{pmatrix} 0.9739 - 0.9751 & 0.221 - 0.227 & 0.0029 - 0.0045 \\ 0.221 - 0.227 & 0.9730 - 0.9744 & 0.039 - 0.044 \\ 0.0048 - 0.014 & 0.037 - 0.043 & 0.9990 - 0.9992 \end{pmatrix} \begin{pmatrix} d \\ s \\ b \end{pmatrix}.$$

The comparable matrix for leptons is not yet well determined and is the subject of much study in the particle physics community. Recent results show that, unlike the CKM matrix, the neutrino mixing matrix is far from diagonal[9]:

$$\begin{pmatrix} \nu_e \\ \nu_\mu \\ \nu_\tau \end{pmatrix} = \begin{pmatrix} 0.72 - 0.88 & 0.46 - 0.68 & < 0.22 \\ 0.25 - 0.65 & 0.27 - 0.73 & 0.55 - 0.84 \\ 0.10 - 0.57 & 0.41 - 0.80 & 0.52 - 0.83 \end{pmatrix} \begin{pmatrix} \nu_1 \\ \nu_2 \\ \nu_3 \end{pmatrix}. \tag{1.10}$$

$\left\|g^S_{RR}\right\| < 0.067$	$\left\|g^V_{RR}\right\| < 0.034$	$\left\|g^T_{RR}\right\| \equiv 0$
$\left\|g^S_{RL}\right\| < 0.424$	$\left\|g^V_{RL}\right\| < 0.104$	$\left\|g^T_{RL}\right\| < 0.104$
$\left\|g^S_{LR}\right\| < 0.088$	$\left\|g^V_{LR}\right\| < 0.036$	$\left\|g^T_{LR}\right\| < 0.036$
$\left\|g^S_{LL}\right\| < 0.550$	$\left\|g^V_{LL}\right\| > 0.960$	$\left\|g^T_{LL}\right\| \equiv 0$

Table 1.3: Coupling constant limits [8, 10].

1.4 Muon Decay

In the standard model of particle physics, muons decay via the weak vector minus axial vector (V-A) interaction into positrons plus neutrinos. V-A refers to the form of the operators in the Lagrangian for the interaction, where a vector operator can be written as the Dirac matrix γ_μ, and an axial vector operator is of the form $\gamma_5\gamma_\mu$. Thus a V-A operator is $\gamma_\mu(1-\gamma_5)$, and a V+A operator is $\gamma_\mu(1+\gamma_5)$. A brief review of the standard model is in Section 1.3. The muon decay reaction can be written, with a virtual W^+_L, as:

$$\begin{array}{ll} \mu^+ \rightarrow \bar{\nu_\mu} & W^+_L, \text{ and,} \\ & W^+_L \rightarrow \nu_e\, e^+. \end{array} \tag{1.11}$$

In this section the matrix element for a general four-fermion point interaction which allows for any interaction (not just the V-A W^+_L) is considered. This formulation gives us a positron spin integrated decay rate that depends on $P_\mu\xi$, and three other muon decay parameters. A review of the previous measurements of $P_\mu\xi$ is presented in this section. Finally to gain some insight into the parameter being measured, two methods of extracting an estimate of $P_\mu\xi$ from the asymmetry of the decay rate are presented.

1.4.1 General Four-Fermion Point Interaction

The decay of polarized muons into positrons and neutrinos can be described by a general derivative-free interaction. The matrix element of this four-point fermion interaction is given by [8]:

$$M = 4\frac{G_F}{\sqrt{2}} \sum_{\substack{\gamma = S,V,T \\ \epsilon,\mu = R,L}} g^\gamma_{\epsilon\mu} < \bar{e}_\epsilon|\Gamma^\gamma|\nu_e >< \bar{\nu}_\mu|\Gamma_\gamma|\mu_\mu > . \tag{1.12}$$

where $\gamma = S, V, T$ refer to the scalar, vector, and tensor interactions, and $\epsilon, \mu = L, R$ refer to the chirality of the electron or muon. Thus there are 10 complex amplitudes, or 19 independent real parameters, where $g^T_{LL} = 0$, and $g^T_{RR} = 0$. In the standard model (V-A), all of these parameters are zero except for $g^V_{LL} = 1$. Current ninety percent confidence level limits for the coupling constants are shown in Table 1.3.

The measurable muon decay parameters $(\rho, \delta, \xi, \eta)$ can be written in terms of the coupling constants [11]:

$$
\begin{aligned}
\rho &= \tfrac{3}{4} - \tfrac{3}{4}[\left|g_{RL}^{V}\right|^2 + \left|g_{LR}^{V}\right|^2 + 2\left|g_{RL}^{T}\right|^2 + 2\left|g_{LR}^{T}\right|^2 \\
&\quad + Re\left(g_{RL}^{S}g_{RL}^{T*} + g_{LR}^{S}g_{LR}^{T*}\right)], \\
\eta &= \tfrac{1}{2}Re[g_{RR}^{V}g_{LL}^{S*} + g_{LL}^{V}g_{RR}^{S*} + g_{RL}^{V}(g_{LR}^{S*} + 6g_{LR}^{T*}) + g_{LR}^{V}(g_{RL}^{S*} + 6g_{RL}^{T*})], \\
\xi &= 1 - \tfrac{1}{2}\left|g_{LR}^{S}\right|^2 - \tfrac{1}{2}\left|g_{RR}^{S}\right|^2 - 4\left|g_{RL}^{V}\right|^2 + 2\left|g_{LR}^{V}\right|^2 - 2\left|g_{RR}^{V}\right|^2 \\
&\quad + 2\left|g_{LR}^{T}\right|^2 - 8\left|g_{RL}^{T}\right|^2 + 4Re(g_{LR}^{S}g_{LR}^{T*} - g_{RL}^{S}g_{RL}^{T*}), \text{ and} \\
\xi\delta &= \tfrac{3}{4} - \tfrac{3}{8}\left|g_{RR}^{S}\right|^2 - \tfrac{3}{8}\left|g_{LR}^{S}\right|^2 - \tfrac{3}{2}\left|g_{RR}^{V}\right|^2 - \tfrac{3}{4}\left|g_{RL}^{V}\right|^2 - \tfrac{3}{4}\left|g_{LR}^{V}\right|^2 \\
&\quad - \tfrac{3}{2}\left|g_{RL}^{T}\right|^2 - 3\left|g_{LR}^{T}\right|^2 + \tfrac{3}{4}Re(g_{LR}^{S}g_{LR}^{T*} - g_{RL}^{S}g_{RL}^{T*}).
\end{aligned}
\tag{1.13}
$$

The muon decay parameters are often referred to as the Michel parameters, even though only the parameter ρ was introduced by Michel. In terms of the muon decay parameters, the differential decay rate of positively charged muons without explicit radiative corrections (RC), is:

$$
\frac{d^2\Gamma}{dx\,d\cos\theta} = \frac{m_\mu}{4\pi^3}W_{e\mu}^4 G_F^2\sqrt{x^2 - x_0^2}\,(F_{IS}(x) + P_\mu\cos\theta F_{AS}(x)) + \text{RC}. \tag{1.14}
$$

The angle θ, as written above, is the angle between the muon spin and decay positron momentum. In the $\mathcal{TWIST}$ coordinate system, a minus sign should appear in front of P_μ, since in $\mathcal{TWIST}$, θ is measured relative to the muon momentum. P_μ is positive since it is defined to be the degree of muon polarization (a magnitude). The positron reduced energy (x), maximum energy transfered to the positron ($W_{e\mu}$), and minimum positron reduced energy (x_0) are given by:

$$
\begin{aligned}
x &= E_e/W_{e\mu}, \\
W_{e\mu} &= \tfrac{m_\mu^2+m_e^2}{2m_\mu}, \text{ and} \\
x_0 &= \tfrac{m_e}{W_{e\mu}}.
\end{aligned}
\tag{1.15}
$$

The isotropic and anisotropic parts of the spectrum are:

$$
\begin{aligned}
F_{IS}(x) &= x(1-x) + \tfrac{2}{9}\rho(4x^2 - 3x - x_0^2) + \eta x_0(1-x), \text{ and} \\
F_{AS}(x) &= \tfrac{1}{3}\xi\sqrt{x^2 - x_0^2}\left[1 - x + \tfrac{2}{3}\delta(4x - 3 + (\sqrt{1 - x_0^2} - 1))\right].
\end{aligned}
\tag{1.16}
$$

The standard model values of the parameters are: $\rho = \delta = \frac{3}{4}$, $\eta = 0$, and $\xi = 1$. The differential decay rate for the standard model case is shown in Figure 1.2.

1.4.2 Previous $P_\mu\xi$ Measurements

This section describes the two previous best direct measurements of $P_\mu\xi$, and states the most stringent limit on the parameter being measured.

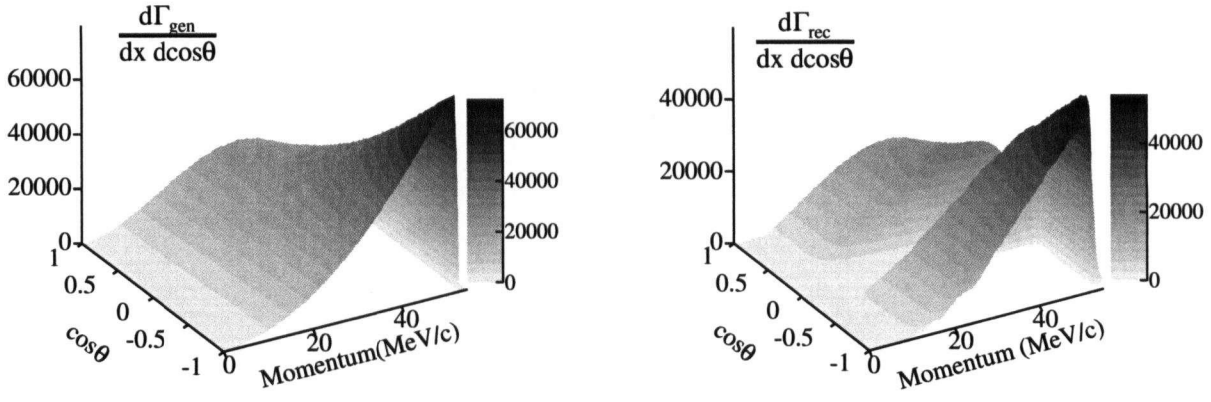

Figure 1.2: The theoretical distribution of positron angles and momenta with 100 % acceptance is shown on the left. Positrons that pass the $\mathcal{TWIST}$ detector acceptance have the distribution shown on the right.

$P_\mu\xi$ was determined in a direct measurement by Beltrami *et al.* in a μSR experiment at Paul Scherrer Institute (PSI) in Switzerland [12]. Muons from pion decays in flight were stopped in a Be target. The muon spin precessed in a 30 gauss transverse field, and decay positrons were counted in a scintillator telescope. The resulting spectrum was fit over a $3\tau_\mu$ time period yielding the asymmetry parameter, $P_\mu\xi = 1.0027 \pm 0.0079$ (stat) ± 0.0028(syst).

Imazato *et al.* measured $P_\mu\xi = 1.0013 \pm 0.0030$(stat)$\pm 0.0053$(syst) at KEK, in Tsukuba Japan, by performing a 105 G transverse field μSR experiment on muons from kaon decay [13]. The muons were stopped in a thin platinum target, and the subsequent decay positrons were counted in drift chambers. Since the muon polarization is prepared by kaon decay rather than pion decay, the result is quoted separately rather than being used in a calculation of an average value of $P_\mu\xi$.

The ratio of parameters, $P_\mu\xi\delta/\rho$, is determined by measuring the momentum endpoint in the direction antiparallel to P_μ. Jodidio *et al.* measured this parameter in an experiment at TRIUMF [14]. Muons were stopped in various metal foils (Ag, Al, Au and Cu) or liquid helium. The muon spin was held fixed by a magnetic field oriented parallel to the spin. Decay positrons with momentum approximately antiparallel to the spin were focused into a series of drift chambers located upstream and downstream of a region with a transverse field.

Using the Jodidio result of $P_\mu\xi\delta/\rho > 0.99682$ at the 90% confidence limit along with the new $\mathcal{TWIST}$ measurements of ρ and δ, an indirect limit on $P_\mu\xi$ can be obtained: $0.9960 < P_\mu\xi <= \xi < 1.0040$ (90% confidence limit) [15, 16].

1.4.3 Muon Decay Asymmetry in Angle (MDAA)

This section will describe how $P_\mu \xi$ is related to the asymmetry in angle of the decay positrons. This is done using two different definitions of asymmetry. The first involves the sum of counts upstream and downstream which will be referred to as the integral asymmetry, while the second involves the counts at $\cos\theta = \pm 1$ which will be called the asymmetry.

MDAA: Integral Asymmetry

The integral asymmetry (G) calculated using both upstream and downstream decay positrons is defined as the difference between the number of forward decays (F) and the number of backward decays(B) divided by their sum as in Equation 1.17.

$$G = \frac{F - B}{F + B} \tag{1.17}$$

To calculate the expected asymmetry, we can start with the expression for the differential decay rate in Equation 1.18[8]:

$$\frac{d\Gamma}{dx d\cos\theta} \propto 3x^2 - 2x^3 - P_\mu \xi \cos\theta(2x^3 - x^2). \tag{1.18}$$

Now we integrate over reduced energy from any lower limit p, to any upper limit q:

$$\frac{d\Gamma}{d\cos\theta} \propto \int_p^q [3x^2 - 2x^3 - P_\mu \xi \cos\theta(2x^3 - x^2)]dx, \text{ and} \tag{1.19}$$

$$\frac{d\Gamma}{d\cos\theta} \propto q^3 - p^3 - \frac{1}{2}(q^4 - p^4) - P_\mu \xi \cos\theta(\frac{q^4 - p^4}{2} - \frac{q^3 - p^3}{3}). \tag{1.20}$$

Next we set $r = q^3 - p^3$, and $s = q^4 - p^4$, then the number of forward counts (F) is given by integrating over $\cos\theta$ from a to b:

$$F \propto \int_a^b [r - s/2 - P_\mu \xi \cos\theta(s/2 - r/3)]d\cos\theta, \text{ and} \tag{1.21}$$

$$F \propto (r - s/2)(b - a) - P_\mu \xi (s/2 - r/3)(\frac{b^2}{2} - \frac{a^2}{2}). \tag{1.22}$$

Similarly, the number of backward counts (B) is found by integrating over $\cos\theta$ from -b to -a:

$$B \propto \int_{-b}^{-a} [r - s/2 - P_\mu \xi \cos\theta(s/2 - r/3)]d\cos\theta, \text{ and} \tag{1.23}$$

$$B \propto (r - s/2)(b - a) - P_\mu \xi (s/2 - r/3)(\frac{a^2}{2} - \frac{b^2}{2}). \tag{1.24}$$

The asymmetry is then given by:

$$G = \frac{F - B}{F + B} = \frac{-P_\mu \xi [3(q^4 - p^4) - 2(q^3 - p^3)](b + a)}{6[2(q^3 - p^3) - q^4 + p^4]}. \tag{1.25}$$

Using Equation 1.25, we can calculate the expected asymmetry for different cuts on reduced energy and momentum. The expected asymmetry of surface muons for $P_\mu\xi = 1$ and with different fiducial volume cuts is summarized in Table 1.4. Note that the analysis in this section has not accounted for radiative corrections which affect the polarization obtained by a few percent.

Table 1.4: Integral asymmetry of the decay positron spectrum for surface muon decays with $P_\mu\xi = 1$.

Description	p	q	a	b	G
Complete spectrum	0	1	0	1	$\frac{1}{6} = -0.167$
Large acceptance cuts	0.3	1	0.5	0.97	0.264

MDAA: Asymmetry

Here we use a popular definition of asymmetry as in Equation 1.17, where F and B are taken as the decay positron counts at 0 and 180 degree decay angles. Starting from the expressions already integrated over reduced energy in the previous section we find that F and B are:

$$F \propto r - s/2 - P_\mu\xi(s/2 - r/3), \text{ and} \tag{1.26}$$

$$B \propto r - s/2 + P_\mu\xi(s/2 - r/3). \tag{1.27}$$

The asymmetry in this section will be called A (rather than G). Then the asymmetry is given by:

$$A = \frac{-P_\mu\xi}{3}\left(\frac{3s - 2r}{2r - s}\right), \text{ and} \tag{1.28}$$

$$A = \frac{-P_\mu\xi}{3}\left(\frac{3(q^4 - p^4) - 2(q^3 - p^3)}{2(q^3 - p^3) - q^4 + p^4}\right). \tag{1.29}$$

Using the above definition of the asymmetry, the asymmetry for $0 < x < 1$ is 0.333 $P_\mu\xi$. For a fiducial region of $0.3 < x < 1$ the asymmetry is 0.360 $P_\mu\xi$. With this method, a spectrum of $\cos\theta$ of the decay positron can be fit, for any region of $\cos\theta$, to find a slope m, and intercept b. Then the asymmetry and estimated muon polarization P_μ^e, from the slope, m, and intercept, b, is given by:

$$A = \frac{m}{b}, \text{ and} \tag{1.30}$$

$$P_\mu^e\xi = -\frac{m}{3b}\left[\frac{2(q^3 - p^3) - q^4 + p^4}{3(q^4 - p^4) - 2(q^3 - p^3)}\right]. \tag{1.31}$$

Clearly the integral asymmetry (G) is simpler to determine since no fit to a slope and intercept is needed. However the more popular definition (A) of the asymmetry makes it possible to calculate $P_\mu \xi$ when decays in only one direction are observed.

1.5 Brief Review of Muon Spin

The "effective" polarization of the muon, P_μ, comes from the average of the component of the spin parallel to the *TWIST* magnetic field. The largest component of the *TWIST* magnetic field is pointing in the downstream, $+z$, direction and the largest component of the muon spin is pointing in the upstream, $-z$, direction.

This section reviews particle spin, and spin propagation through a magnetic field. The production of a polarized beam of muons from the decay of pions at rest is also reviewed. The propagation of spins is used in our simulation to estimate the "effective" polarization of the muons that stop in an Al target.

1.5.1 Basics of Spin of Leptons

A fundamental property of leptons is their intrinsic spin angular momentum. The spin angular momentum is analogous to an orbital angular momentum due to the orbital motion about a nucleus. The magnetic dipole moment due to the spin of a charged lepton is given by:

$$\vec{M} = -\frac{ge\hbar}{2m}\vec{S} = -g\mu_B\vec{S}, \tag{1.32}$$

where $\mu_B = 9.2741 \times 10^{-24}$ J/T is the Bohr magneton, and $g \approx 2.0$ is a factor due to relativistic kinematics, called Thomas precession. The potential energy (U) of a charged lepton in an external magnetic field (B) is then given by:

$$U = -\vec{M} \cdot \vec{B}. \tag{1.33}$$

The torque ($\vec{\tau}$), and Force ($\vec{F}$) due to the intrinsic spin of a charged lepton in a magnetic field are:

$$\vec{\tau} = \vec{M} \times \vec{B}, \tag{1.34}$$

$$\begin{aligned} \vec{F} &= \vec{\nabla}(\vec{M} \cdot \vec{B}), \text{ and} \\ F_{x_i} &= \vec{M} \cdot \tfrac{\partial \vec{B}}{\partial x_i}. \end{aligned} \tag{1.35}$$

In a uniform magnetic field, the partial derivative of the magnetic field in different directions are zero, therefore there is no net force on the particles due to spin. However there is a torque, which will cause the spin vector to precess about the axis of the magnetic field. If the particles are in an inhomogeneous field, such as in a Stern-Gerlach type apparatus, there is also a force proportional to the gradient of the magnetic field.

1.5.2 Quantization of Spin

In the Stern-Gerlach experiment it was found that the deflection of electrons was concentrated into two different spatial positions, rather than into a continuous blob. This was direct evidence for the quantization of spin. The result also proved that since there were only two spatial positions, the quantum number (s) for the spin of the electron must be (2s+1)=2, or s=1/2. In analogy with orbital angular momentum, the magnitude of the spin is given by the quantum number:

$$|\vec{S}| = \sqrt{s(s+1)}\hbar = \frac{\sqrt{3}}{2}\hbar. \tag{1.36}$$

Along the direction of an external field (z axis), the component of the spin is given by:

$$S_z = \pm\frac{\hbar}{2}. \tag{1.37}$$

The spin is said to precess about the direction of the applied magnetic field. The time-averaged spins in the x and y directions are zero, while $<S_z>$ is $\hbar/2$. The geometry of the spin vector relative to the applied magnetic field is shown in Figure 1.3.

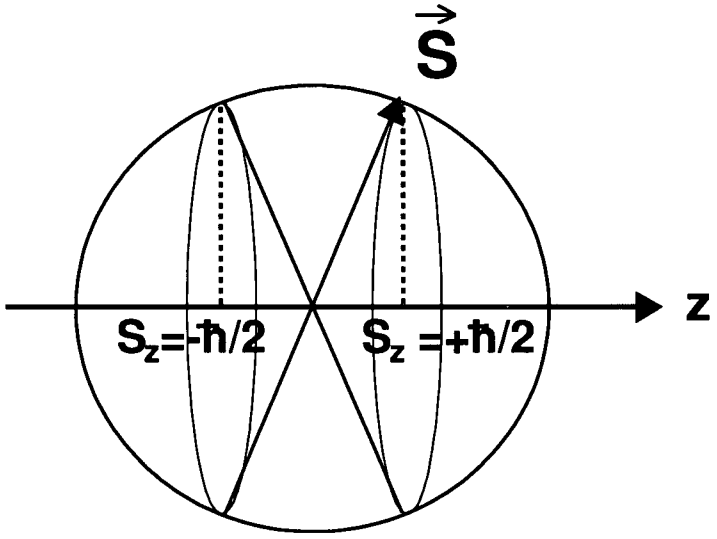

Figure 1.3: Vector diagram of a spin $\frac{1}{2}$ particle. The spin vector $\vec{S}$ precesses about the direction of the magnetic field (z axis). The allowed values of the spin projected onto the z axis are $\pm\hbar/2$.

The sign of the magnetic field does not matter, since this will only change the direction of precession of the spin of a single particle.

1.5.3 Motion of Spin in a Uniform External Magnetic Field

The equation governing the motion of the spin in a uniform magnetic field is:

$$\frac{d\vec{S}}{dt'} = \frac{ge}{2mc}\vec{S} \times \vec{B}', \tag{1.38}$$

where the prime means the quantity is defined in the rest frame of the particle, and $\vec{S}$ is the spin in that frame. Solving this equation for a uniform magnetic field in the z direction, and $S_z(0) = -\hbar/2$, with an arbitrarily chosen initial phase for the x and y components of the spin, we obtain:

$$\begin{gathered} S_x = \tfrac{\hbar}{2}\sin\gamma_z t,\ S_y = \tfrac{\hbar}{2}\cos\gamma_z t,\ S_z = -\tfrac{\hbar}{2},\ \text{and} \\ \gamma_z = \tfrac{ge}{2mc}B_z. \end{gathered} \tag{1.39}$$

Next we take the above conditions, apply a pulse of magnetic field in the x direction for a time $t = \pi/(2\gamma_z)$, and then measure the spin in the y direction. The result is that the spin will have precessed about the x axis by 90 degrees, so that the spin is now given by (neglecting any phase shift due to the field in the z direction, and neglecting the phase of the original x and y components of the spin):

$$S_x = \tfrac{\hbar}{2}\sin\gamma_z t,\ S_y = -\tfrac{\hbar}{2},\ \text{and}\ S_z = \tfrac{\hbar}{2}\cos\gamma_z t. \tag{1.40}$$

So the time averaged spin will be $S_y = -\hbar/2$ immediately after having applied the magnetic pulse in the x direction.

1.5.4 Surface Muon Spin

The spin of muons from the decay of pions at rest is anti-aligned with the momentum of the muon. This section explains how we select muons from pion decays at rest, and why these are highly polarized.

From conservation of momentum we find that the momentum of the muon from these decays is:

$$p_\mu^s = \frac{m_\pi^2 - m_\mu^2}{2m_\pi} = 29.792\ \text{MeV/c}. \tag{1.41}$$

Thus by momentum selection of particles near p_μ^s, we can obtain particles that come from pions that decay at rest near the surface of a pion production target. Pions created deeper in the production target will yield lower momentum muons due to energy loss in the target and pions that decay in flight will yield higher momentum muons.

In 1958, Maurice Goldhaber, Lee Grodzins, and Andrew Sunyar at Brookhaven National Laboratory showed that the electron neutrino has left-handed helicity, meaning that it behaves as if it is spinning along the direction of its motion in the sense of a left-handed screw[17]. The most direct measurement of muon neutrino helicity comes from inverse muon decay rates. Consequently the positively charged muons used in $\mathcal{TWIST}$ have left-handed helicity by conservation of angular momentum in the decay of pions at rest $\pi^+ \rightarrow \mu^+\nu_\mu$. This conservation of momentum and angular momentum is depicted in Figure 1.4.

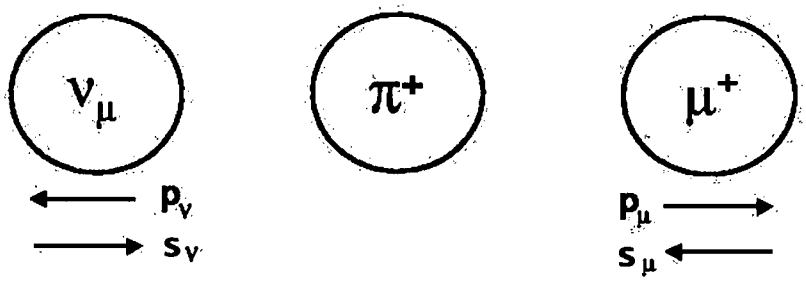

Figure 1.4: Conservation of momentum and angular momentum in pion decay at rest ($\pi^+ \rightarrow \mu^+\nu_\mu$).

1.5.5 The Bargman-Michel-Telegdi Equation

To quantitatively calculate the propagation of the spin as a relativistic particle with spin traverses a non-uniform field, we need the Bargmann-Michel-Telegdi (BMT) equation[18]. The BMT equation is a relativistic generalization of Equation 1.38 for particles traversing fields which are uniform in space[19]:

$$\frac{dS^\alpha}{d\tau} = \frac{e}{mc}\left[\frac{g}{2}F^{\alpha\beta}S_\beta + \frac{1}{c^2}\left(\frac{g}{2}-1\right)U^\alpha(S_\lambda F^{\lambda\mu}U_\mu)\right]. \tag{1.42}$$

S^α is the spin 4-vector, τ is the particle's proper time, g is the Landé factor, m is the particle mass, e is the particle charge, $F^{\alpha\beta}$ is the external field, and U^α is the particle 4-velocity. We can write this in the form of Thomas' equation, making the Thomas precession explicit:

$$\frac{d\vec{s}}{dt} = \frac{e}{mc}\vec{s}\times\left[\left(\frac{g}{2}-1+\frac{1}{\gamma}\right)\vec{B} - \left(\frac{g}{2}-1\right)\frac{\gamma}{\gamma+1}(\vec{\beta}\cdot\vec{B})\vec{\beta} - \left(\frac{g}{2}-\frac{\gamma}{\gamma+1}\right)\vec{\beta}\times\vec{E}\right]. \tag{1.43}$$

From this equation we can find the rate of change of the component of the spin, $\vec{s}$, parallel to the velocity, $\vec{\beta}$. This rate of change is:

$$\frac{d}{dt}(\hat{\beta}\cdot\vec{s}) = -\frac{e}{mc}\vec{s_{\perp}}\cdot\left[\left(\frac{g}{2}-1\right)\hat{\beta}\times\vec{B}+\left(\frac{g\beta}{2}-\frac{1}{\beta}\right)\vec{E}\right]. \tag{1.44}$$

So if we are considering only the effect of a magnetic field $\vec{B}$, we see that the full change is due to the transverse components of the magnetic field (ie. the field perpendicular to the direction of the particle's travel). Due to radiative corrections the standard model the muon value of g_μ is not identically two. The experimentally measured value of g_μ is:

$$a(\mu^{\pm}) = (\frac{g_\mu}{2}-1) = 0.0011659203(7). \tag{1.45}$$

Note that the first order radiative correction which is of order $\alpha/(2\pi) = 0.00116$ dominates the difference of g_μ from two.

1.6 Energy Loss and Muon Depolarization

Muon energy loss in the range of momentum from 30 MeV/c ($\beta\gamma = 0.28$) to 10 keV/c ($\beta\gamma = 0.0001$) is described by three different energy regions. In the lowest energy region, $0.001 < \beta\gamma < 0.005$, the muon velocity is comparable to the orbital velocity of electrons in atoms. The energy loss estimated by Lindhard uses a model that approximates the electronic structure of materials by a Fermi electron gas distribution[20]. In the intermediate energy region, $0.005 < \beta\gamma < 0.1$, there is no satisfactory theory, so energy loss is calculated using parameterized fits to data as done by Anderson and Ziegler[21]. For the highest muon energies used, $0.1 < \beta\gamma < 0.28$, the muon energy loss is calculated with the Bethe-Bloch equation with C/Z shell corrections of the Barkas form[22].

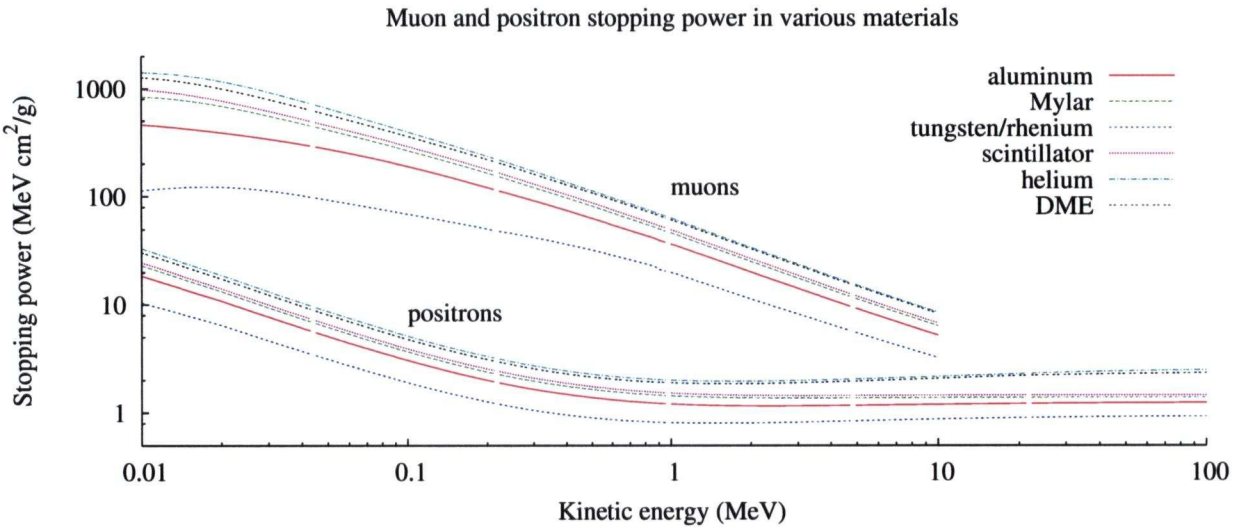

Figure 1.5: Stopping power of positrons and muons in several materials for the range of energies tracked in the simulation. Below the lowest energy on this plot, the stopping power for muons drops again and can be estimated using the Lindhard model.

Muon and positron stopping power as a function of kinetic energy is plotted for several materials in in Figure 1.5. The Bethe-Bloch equation with shell corrections is:

$$-\frac{1}{\rho}\left(\frac{dE}{dx}\right) = \frac{K}{A}z^2 Z \frac{1}{\beta^2}\left[\frac{1}{2}\ln\frac{2m_e c^2\beta^2\gamma^2 T_{\max}}{I^2} - \beta^2 - \delta/2 - C/Z\right], \tag{1.46}$$

where ρ is the material density, $K/A = 0.307075$ MeV g^{-1} cm^2 for $A = 1$ g/mol, z is the particle charge number, Z is the atomic number of the material, $\beta = v/c$ is the particle velocity, $T_{\max}$ is the maximum kinetic energy imparted to an electron in a single collision with the particle, $\delta/2$ is due to the density effect and C/Z is the shell correction. Higher energy effects such as the density correction and radiation losses are completely negligible for surface muons.

The mechanism for energy loss for surface muons is dominated by ionization losses. Depolarization that occurs in the scattering of polarized electrons was studied by Ford and Mullin in 1957[23], and by Iddings in 1964[24]. For polarized muons, the work of Lyuboshits, which relates the rotation angle of the polarization vector of a muon moving in an electric field to the rotation angle of the momentum of the particle, is considered[25]. Surface muons stopped in aluminum were predicted, in a technical note by Pierre Depommier, to depolarize by 4×10^{-5}[26]. Mechanisms for muon depolarization at the muon stopping location are discussed in Section 6.1.4.

1.7 Physics Motivation

1.7.1 Model Independent Tests

Measurements of the muon decay parameters can be used to determine the probabilities for the decay of a μ-handed muon into an ϵ-handed positron (μ,$\epsilon = L, R$). These probabilities, denoted by $Q_{\epsilon\mu}$, can be expressed in terms of the coupling constants, $g_{\mu\epsilon}$, in the following manner:

$$\begin{array}{rl} Q_{LL} = & \frac{1}{4}|g^S_{LL}|^2 + |g^V_{LL}|^2, \\ Q_{LR} = & \frac{1}{4}|g^S_{LR}|^2 + |g^V_{LR}|^2 + 3|g^T_{LR}|^2, \\ Q_{RL} = & \frac{1}{4}|g^S_{RL}|^2 + |g^V_{RL}|^2 + 3|g^T_{RL}|^2, \text{ and} \\ Q_{RR} = & \frac{1}{4}|g^S_{RR}|^2 + |g^V_{RR}|^2. \end{array} \tag{1.47}$$

Hence the probability of right-handed muons decaying into any-handed positrons is given by:

$$Q^\mu_R = Q_{RR} + Q_{LR} = \frac{1}{4}(|g^S_{LR}|^2 + |g^S_{RR}|^2) + |g^V_{LR}|^2 + 3|g^T_{LR}|^2 + |g^V_{RR}|^2. \tag{1.48}$$

In terms of the Michel parameters this probability can be written as:

$$Q^\mu_R = \frac{1}{2}(1 + \frac{1}{3}\xi - \frac{16}{9}\xi\delta). \tag{1.49}$$

Improved precision on the measurements of ξ and δ can thus be used to set limits on the existence of right-handed interactions.

1.7.2 Left-Right Symmetric Model Tests

The left-right symmetric (LRS) model has $SU(2)_L \times SU(2)_R \times U(1)$ as the gauge group [27]. In this model both V-A and V+A are present, and parity violation appears because of the difference in mass of the vector bosons. The LRS model contains four charged gauge bosons $W_1^\pm$, $W_2^\pm$, the photon, and two additional massive neutral gauge bosons. The W_1 and W_2 masses are m_1 and m_2 respectively.

To produce Dirac fermion masses one Higgs field is needed; an additional Higgs field needed to break the gauge symmetry down to $U_{EM}(1)$, can also generate Majorana neutrino [28] mass terms, making the neutrino its own antiparticle.

In terms of mass eigenstates, the couplings of W_L and W_R to fermions is written in the Lagrangian as:

$$\begin{array}{rl} \mathcal{L} = & \frac{g_L}{2\sqrt{2}} W_L(\bar{P}\Gamma_L U_L N + \bar{N}^{(0)}\Gamma_L U^\dagger E) + \\ & \frac{g_R}{2\sqrt{2}} W_R(\bar{P}\Gamma_R U_R N + \bar{N}^{(0)}\Gamma_R V^\dagger E) + \text{HC}, \end{array} \tag{1.50}$$

where, HC is the Hermitian conjugate, and $\Gamma_L = \gamma_\lambda(1-\gamma_5)$ and $\Gamma_R = \gamma_\lambda(1+\gamma_5)$ are the left- and right-handed projection operators. P is the triplet of up type quarks, N is the triplet of down type quarks, E is the triplet of electron type leptons, and $N^{(0)}$ is the triplet of neutrino

mass eigenstates. The fields W_L and W_R are related to the mass eigenstates W_1 and W_2 through a mixing angle, ζ, and CP violating phase, ω, by:

$$\begin{aligned} W_L &= W_1 \cos\zeta + W_2 \sin\zeta, \text{ and} \\ W_R &= e^{i\omega}(-W_1 \sin\zeta + W_2 \cos\zeta). \end{aligned} \tag{1.51}$$

If neutrinos are Dirac particles, then U_L, U_R, U, and V are unitary $n \times n$ matrices, where $n = 3$ is the number of generations. Together, these four matrices contain 12 mixing angles and 14 CP violating phases. If neutrinos are their own antiparticles (Majorana) then $\mathcal{L}$ also contains the 6 Majorana neutrinos where U and V become $n \times 2n$ matrices with 15 mixing angles and 18 CP violating phases. In general, the left- and right-handed neutrinos are written as a sum, j, over the neutrinos involved in the decay, as:

$$\begin{aligned} \nu_l^L &= \textstyle\sum_j U_{lj}\nu_j \quad (l = e, \mu), \text{ and} \\ \nu_l^R &= \textstyle\sum_j V_{lj}\nu_j \quad (l = e, \mu). \end{aligned} \tag{1.52}$$

Recent observations of neutrino oscillations imply mixing in the lepton sector [29]-[37]. For light Dirac or Majorana neutrinos, we can write the right-handed (left-handed) neutrinos as u_l (v_l), and the ratio of right- over left-handed neutrinos ($\tilde{v}_l$) as:

$$\begin{aligned} u_l &= \textstyle\sum_j' |U_{lj}|^2 \nu_j \quad (l = e, \mu), \\ v_l &= \textstyle\sum_j' |V_{lj}|^2 \nu_j \quad (l = e, \mu), \text{ and} \\ \tilde{v}_l &= u_l / v_l. \end{aligned} \tag{1.53}$$

The primes on the sum mean the sum is over those neutrinos and antineutrinos that are involved in normal muon decay. If all of the neutrinos can be created in the decay then $u_l = v_l = 1$. The approximate expressions for the muon polarization and muon decay asymmetry parameter become:

$$\begin{aligned} P_\mu &\approx 1 - 2t_\theta^2 \tilde{v}_\mu - 2\zeta_g^2 \tilde{v}_\mu - 4t_\theta \zeta_g \tilde{v}_\mu \cos(\alpha + \omega), \text{ and} \\ \xi &\approx 1 - 2t^2 \tilde{v}_e \tilde{v}_\mu + 2\zeta_g^2 \tilde{v}_\mu - 4\zeta_g^2 \tilde{v}_e. \end{aligned} \tag{1.54}$$

α is a CP violating phase in the right-handed CKM matrix, ω is a CP violating phase in W mixing:

$$\begin{aligned} t_\theta &= t\frac{\cos\theta_1^R}{\cos\theta_1^L} = \frac{g_R^2 m_1^2 \cos\theta_1^R}{g_L^2 m_2^2 \cos\theta_1^L}, \text{ and} \\ \zeta_g &= \frac{g_R}{g_L}\zeta. \end{aligned} \tag{1.55}$$

$\theta_1^L = \theta_c$ is the Cabbibo angle for semileptonic decays involving left-handed neutrinos. Note that in terms of CKM matrix elements: $V_{ud}^R = \cos\theta_{12}^R \cos\theta_{13}^R = \theta_c \cos\theta_{13}^R$, and since $\cos\theta_{13}^R \approx 1$ to 6 digits the Cabbibo angle is almost identical to V_{ud}^R. θ_1^R is the Cabbibo angle in the case of right-handed neutrinos. The product $P_\mu\xi$ becomes:

$$P_\mu \xi \approx 1 - 2t_\theta^2 \tilde{v}_\mu - 2t^2 \tilde{v}_e \tilde{v}_\mu - 4\zeta_g^2 \tilde{v}_e - 4t_\theta \zeta_g \tilde{v}_\mu \cos(\alpha + \omega). \tag{1.56}$$

In the case of manifest left-right symmetry (MLRS) the physical left and right-handed interactions are identical. For the MLRS case $t_\theta = t$, $\zeta_g = \zeta$, $\tilde{v}_\mu = \tilde{v}_e = 1$, $\alpha = \omega = 0$, and:

$$P_\mu \xi \approx 1 - 4t^2 - 4\zeta^2 - 4t\zeta. \tag{1.57}$$

We can rewrite this ζ as a function of $P_\mu\xi$ and the W masses:

$$\zeta \approx \frac{1}{2}\left(-\frac{m_1^2}{m_2^2} \pm \sqrt{1 - P_\mu\xi - 3\frac{m_1^4}{m_2^4}}\right). \tag{1.58}$$

The $\pm$ in front of the square root results in a different shaped limit for positive and negative mixing parameter as shown in Figure 1.6.

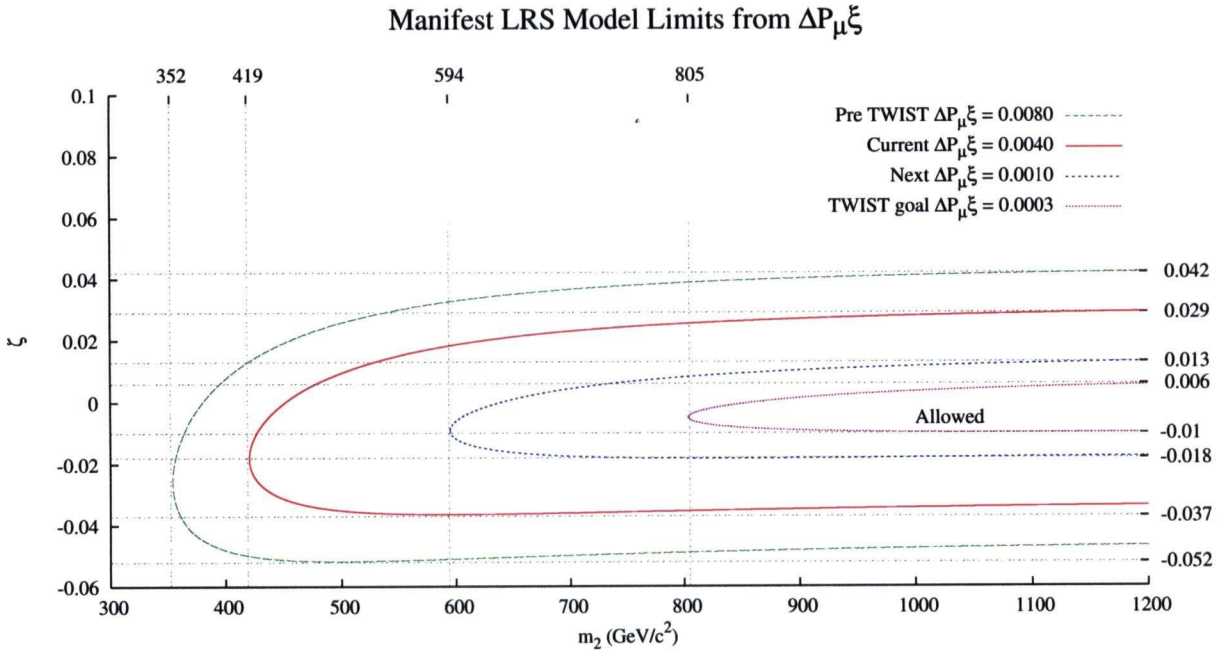

Figure 1.6: Manifest left-right symmetric model values from knowledge of 1-$P_\mu\xi$.

Pseudo manifest left-right symmetry is similar to MLRS, but allows for CP violation to still be present, giving the condition:

$$P_\mu\xi \approx 1 - 4t^2 - 4\zeta^2 - 4t\zeta\cos(\alpha + \omega). \tag{1.59}$$

Thus the combination $P_\mu\xi$ can be used to set limits on the W_R mass and the mixing angle. Figure 1.7 shows the limits on W_R mass and mixing angle from previous experiments, and from the first measurements of ρ and δ from the $\mathcal{TWIST}$ experiment.

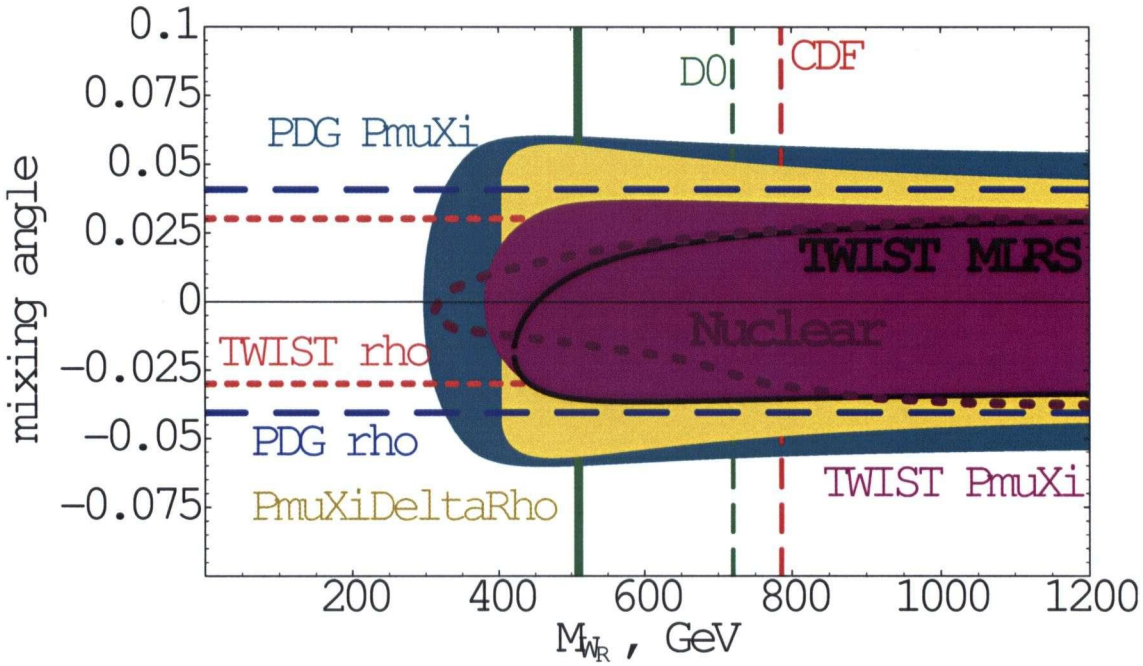

Figure 1.7: Limits on the $W' = W_R$ mass and mixing angle, ζ, showing pre-$\mathcal{TWIST}$ limits, and limits from $\mathcal{TWIST}$'s first measurement of ρ and δ. Limits from nuclear β decay experiments, and high energy experiments such as D0 and CDF, at Fermilab in Chicago, are also shown. The limits from $P_\mu\xi$ are drawn for both the non MLRS case in pink, and for the pseudo MLRS case as the solid black line.

Chapter 2

Apparatus

This chapter outlines the apparatus used for the measurements in this thesis. The sections in this chapter review the production of muons with the TRIUMF cyclotron, their transport down the M13 beamline, their injection into our detector solenoid field, the detector stack including details on the drift chambers, proportional chambers, gas system, muon stopping target, muon ranging beam package, muon beam measuring time expansion chamber, and the muon scintillator trigger.

2.1 TRIUMF Cyclotron and Muon Production

The TRIUMF cyclotron can produce a 140 μA current beam of 520 MeV protons. Cyclotrons consist of two parts: a dipole magnet to confine the ion orbits to circles, and a radio frequency (RF) electric field to accelerate the ions to higher radius orbits. The TRIUMF dipole magnet is 18 m diameter and produces a magnetic field of 0.56 tesla. Classically, the radius of the ion orbit depends only on its velocity as written in the force balance equation:

$$F = qvB = \frac{mv^2}{r} \Rightarrow r = \frac{mv}{qB}. \tag{2.1}$$

The TRIUMF cyclotron RF electric field oscillates at 23 MHz. Also classically, the RF field frequency doesn't have to change as the ion is accelerated since the angular frequency is:

$$\omega = \frac{v}{r} = \frac{qB}{m}. \tag{2.2}$$

One problem is that as the particle becomes relativistic there is a need for a higher magnetic field as the particle mass increases. Increasing the magnetic field as the radius increases would cause a defocusing of the H^- ions. To overcome this defocusing effect, the TRIUMF magnetic field is broken up into six crescent shaped sectors. Each sector has a high magnetic field, and between each sector there is a much lower magnetic field. The alternating sectors provide focusing of the beam with carefully designed azimuthal components of the field between sectors. Cyclotrons of this type of design are called azimuthally varying field (AVF) cyclotrons.

At the start H^- ions are injected into the center of the cyclotron. As the H^- accelerates, its radius in the cyclotron grows in proportion to its speed. When the ions arrive at the outer edge of the cyclotron, they are extracted when they pass through a thin carbon foil. The foil strips the electrons off the H^- ion leaving bare protons. Since the charge is then

positive, the polarity of the circle changes, and the proton is extracted. The protons are then collected from the edge of the cyclotron and fed into an evacuated beam pipe. A conceptual drawing of the TRIUMF cyclotron is shown in Figure 2.1.

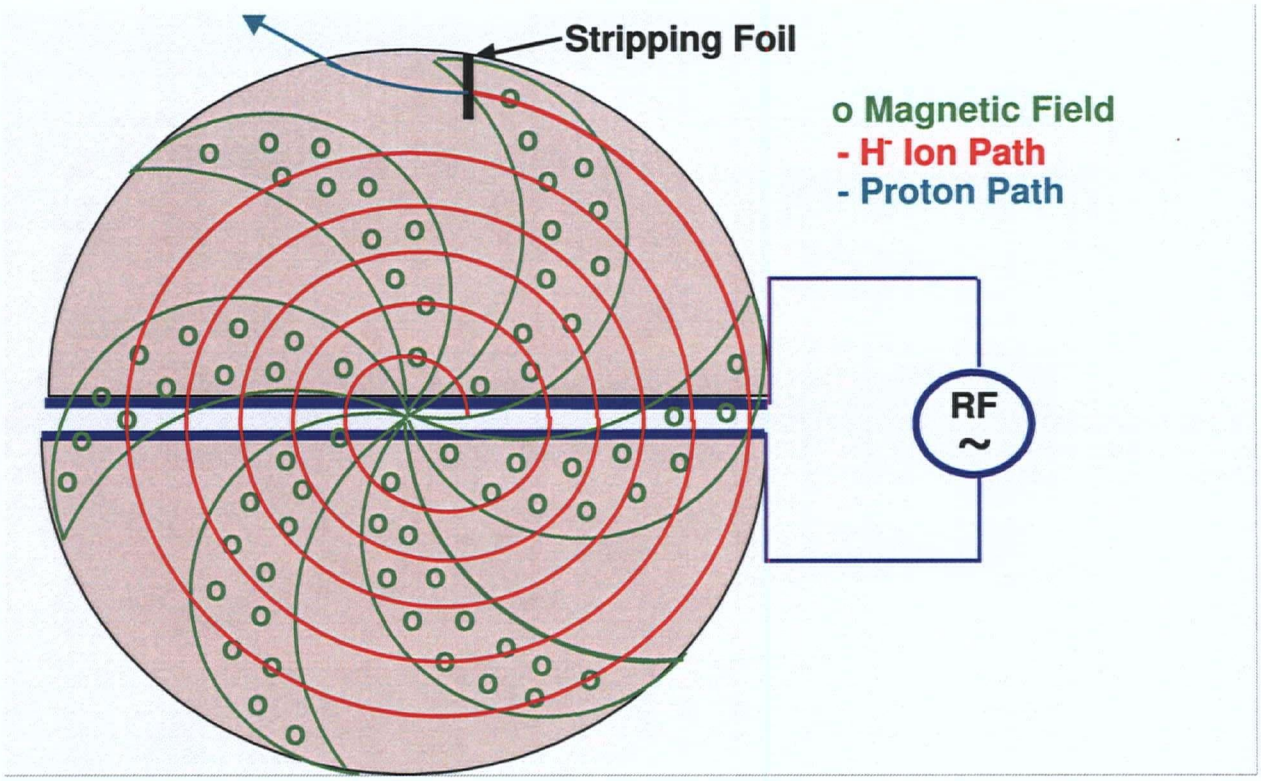

Figure 2.1: Conceptual drawing of the TRIUMF cyclotron.

By sending these protons through different kinds of targets (Be, C), intense beams of positrons, muons, pions, and neutrons are created. Recently, the ISAC (Isotope Separator and Accelerator) facility has been using the protons to produce beams of radioactive isotopes.

2.2 Muon Beam Selection with M13

To obtain highly polarized muons from pion decay, the M13 beamline at TRIUMF is used to momentum-select muons near the momentum of muons from pion decays at rest (29.87 MeV/c). The M13 beamline at TRIUMF has two momentum-selecting dipole magnets labelled B1 and B2, two doublets of quadrupole focusing magnets (Q1/Q2, and Q6/Q7), and a triplet of quadrupole focusing magnets (Q3,Q4 and Q5) as shown in Figure 2.2. Vertical jaws and horizontal slits are located before B1 (slit F0HSL and jaw F0VJ), between B1 and Q3 (slit F1HS), and between Q5 and B2 (slit F2HS and jaw F2VJ).

Protons from the primary beamline incident on a production target at T1 produce pions. The π^+ decays with a lifetime of 26.033 ns via the weak force into a μ^+, and ν_μ as in Figure 1.1d.

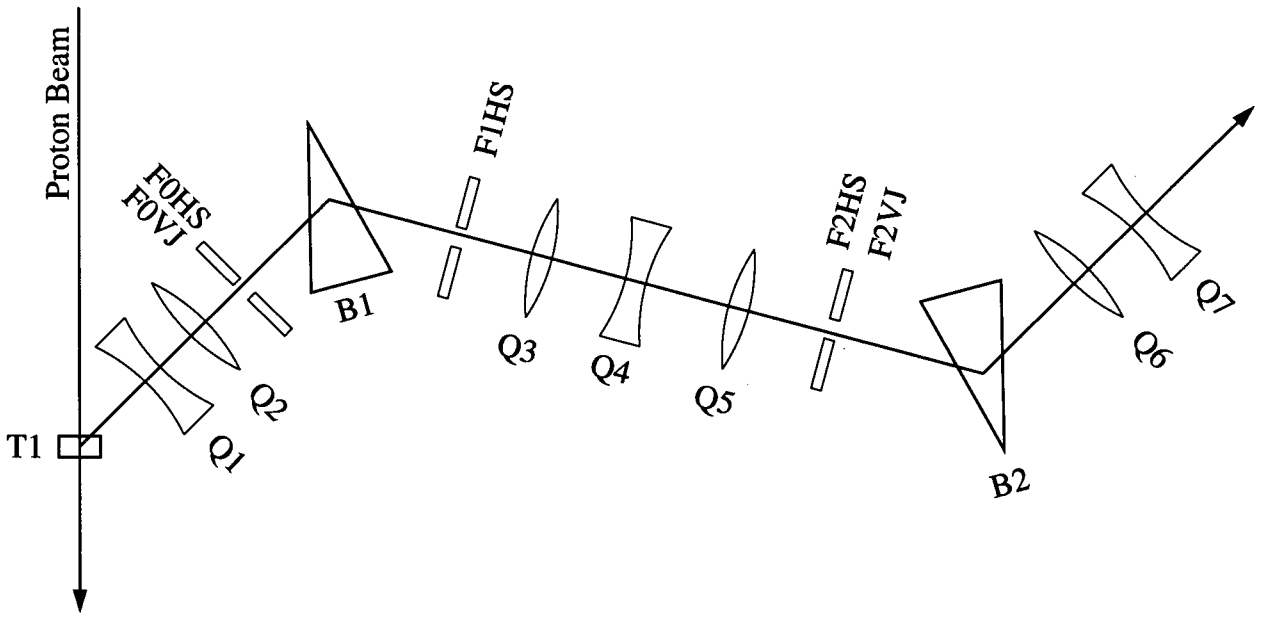

Figure 2.2: M13 beamline at TRIUMF has two dipole momentum-selecting bender magnets (B1 and B2), two doublets of quadrupole focusing magnets (Q1/Q2 and Q6/Q7), and a triplet of quadrupole focusing magnets (Q3, Q4 and Q5).

The momentum resolution of the channel dictates the average depth in the production target (T1) where the muons are created. Due to the finite resolution of the channel, and to avoid rate loss when sitting right at the energy above which muon production from pions at rest, the channel is tuned to a slightly lower momentum of 29.6 MeV/c. The momentum resolution of the channel is about 1% (0.3 MeV/c), and is measured by looking at the normalized rate in a scintillator at the end of the beamline as a function of the momentum at which the M13 beamline is tuned. A measurement of the M13 momentum resolution is shown in Figure 2.3.

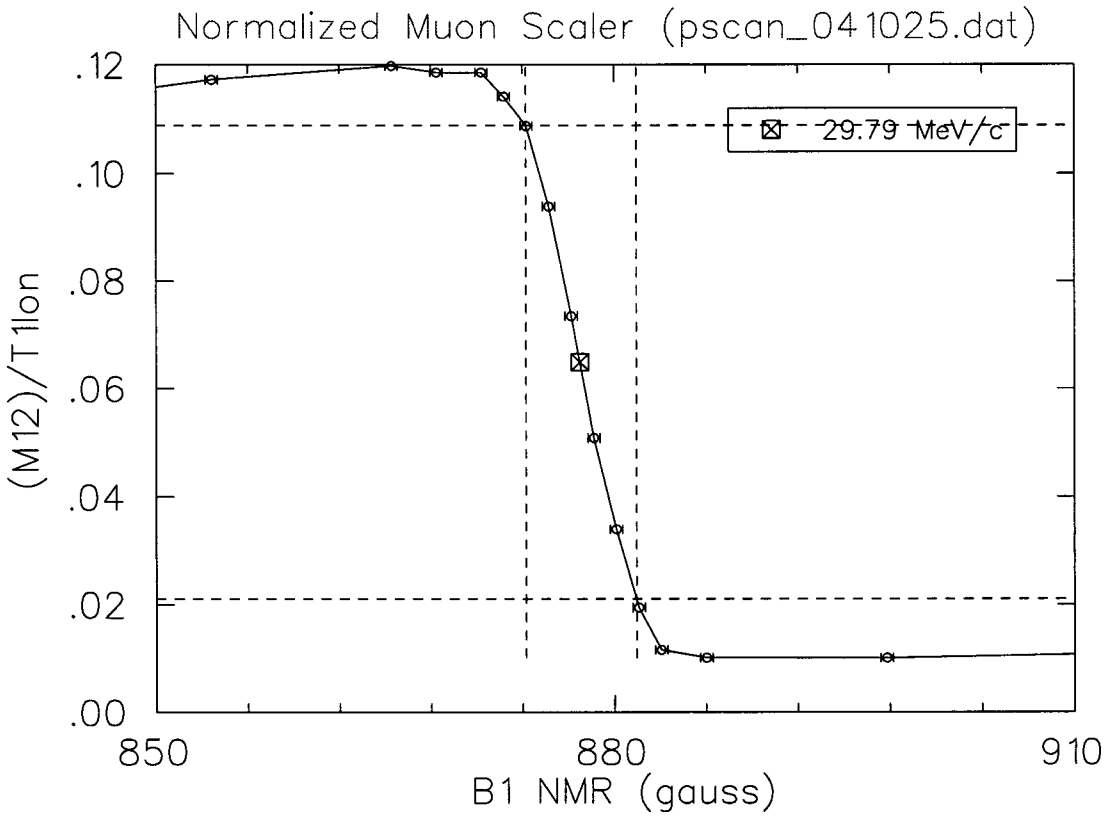

Figure 2.3: The width of the drop in muon count rate as the momentum of the channel is tuned above the surface muon edge is representative of the channel resolution. The plot above is from a scan done in fall 2004 with the graphite target at T1. The square shows where the mid-point of the edge is located; this should represent 29.79 MeV/c. In this scan the momentum resolution of the channel had a sigma of 0.19%.

2.2.1 Muon Production Target

The production target used for 2002 and 2003 data was a Be target surrounded by a water-cooled steel can. The Be was 12 mm long in the direction of the proton beam, 5.08 mm wide, and 14.73 mm tall. The M13 channel viewed the target at 135 degrees from the direction of the incident proton beam, so it views both the 12 mm wide face and the 5.08 mm side. The steel cylinder that surrounds the Be target adds a few mm to the dimensions of the target in each direction. The Be target could be used with proton beam currents up to 170 μA.

For 2004 data-taking a graphite target was used. The face of the graphite target that the proton beam hits is a quarter circle of 18 mm radius, which is 10 mm thick in the direction of the proton beam. The graphite is cooled by water flowing in a steel holder that covers the bottom circular edge of the target. The M13 channel sees both the 10 mm long face of the graphite, and the quarter circular face. The target is positioned so that the proton beam hits the face of the graphite target about 2 mm from the corner of the target (2 mm

from the center of the circle that makes the quarter circular face). The 10 mm graphite target could be used with proton beam currents up to 100 μA. Conceptual drawings of the production targets are shown in Figure 2.4. The 10 mm graphite muon production target was used during the data collection for this measurement of $P_\mu \xi$.

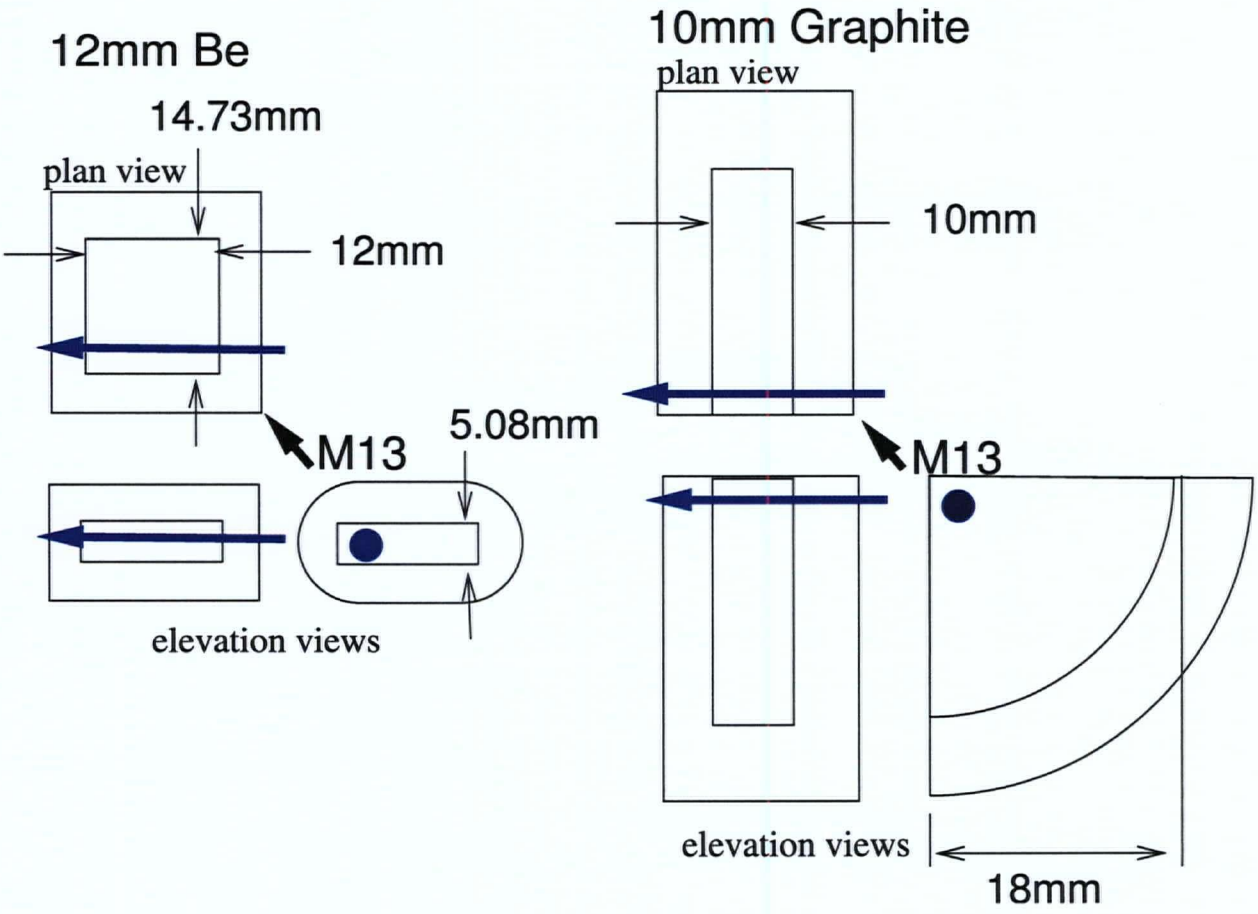

Figure 2.4: The 12 mm Be target is shown on the left, and the 10 mm graphite target is shown on the right. The steel jacket and water cooling are the unhatched regions, and the target material is hatched. The top two projections are looking down on the production target. Where the proton beam hits the targets is shown as the blue arrow. The short black arrow shows the direction in the top view from which M13 views the target.

2.3 TWIST Spectrometer

This section describes the hardware which is used for the *TWIST* measurements[38]. The following sections review the performance of the magnetic field, chamber spacing, drift chambers (DC), proportional chambers (PC), gas system, stopping target, beamline, beam package, muon ranging gas degrader, beam characterizing time expansion chamber (TEC), and the trigger scintillator. A conceptual drawing of *TWIST* is shown in Figure 2.5. A removable Time Expansion Chamber (TEC) outside the upstream end of the magnet yoke is not shown in the figure.

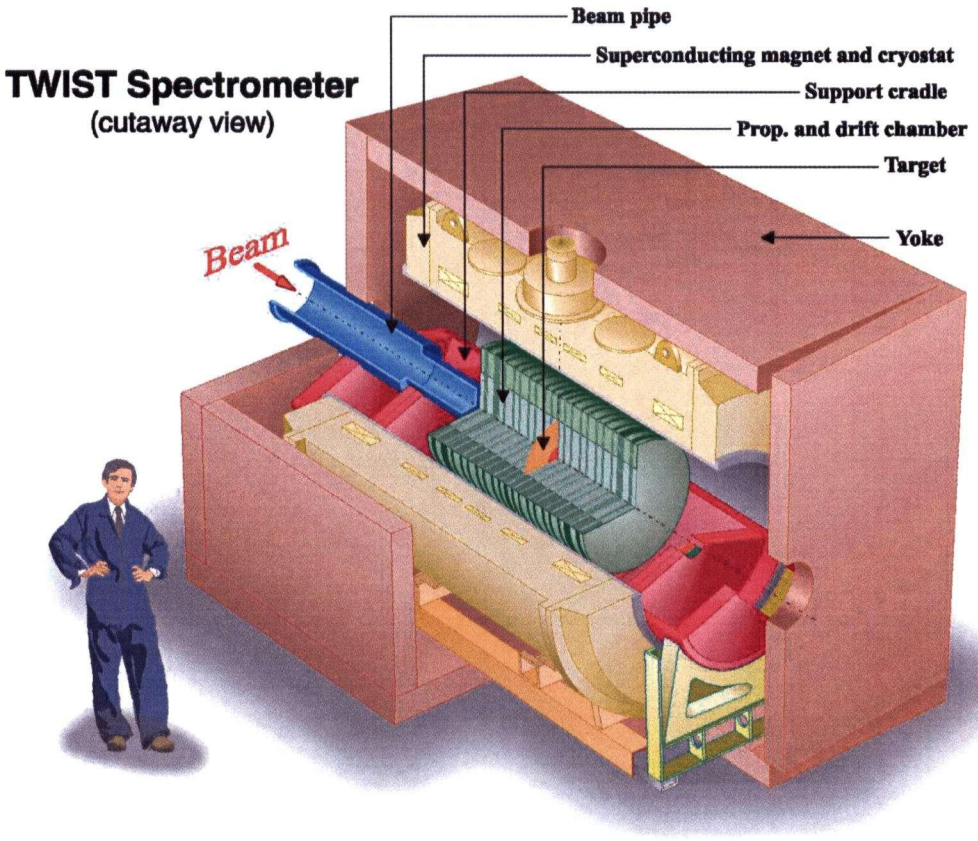

Figure 2.5: The *TWIST* spectrometer. (Courtesy of *TWIST*.)

The detector consists of a stack of 44 DCs and 12 PCs. The DC chambers come in two configurations called "UV modules", and "dense stacks". Each UV module consists of two orthogonal wire planes that share a cathode foil. The UV refers to the rotation of the wire planes by ± 45 degrees with respect to vertical. The dense stack consists of eight drift chambers that share cathodes. The PC modules consist of four wire planes. One PC module is at either end of the detector, and an altered PC module with a stopping target cathode foil at its midpoint is at the center of the detector. The DC and PC modules are arranged mirror-symmetrically around the stopping foil, with the exception of the target PC, which

going from furthest upstream to downstream planes has the V, U, V, U configuration.

2.4 Solenoid Magnet and Iron Yoke

The 2 tesla solenoidal magnetic field used in *TWIST* is produced by an Oxford liquid ^{4}He cooled superconducting magnet formerly used for magnetic resonance imaging. The solenoid has an inner radius of 50 cm and a length of 223 cm. The solenoid is surrounded by an iron box with holes for cryogenics, electronics cables, and for injecting the muon beam into detector. The yoke is designed to contain the magnetic field to a small region around the experiment, and to reduce the depolarization of the muons entering the detector.

Ideally the magnetic field is meant to be uniform and aligned with the axis of the muon beam momentum (and anti-aligned with the muon spin), which is labeled as the $+z$ coordinate in *TWIST*. The field shaping elements of the magnet are input into a simulation package called Opera[39]. The magnetic field is modeled in order to create a field map that includes the radial components of the field as well as the longitudinal components at each of the positions at which the longitudinal component was measured. The measured longitudinal field is shown in Figure 2.6.

The magnetic field of the solenoid was mapped using a specially constructed mapping tool which used Hall Probes, and NMRs to measure the magnetic field. The component of the magnetic field along z was mapped in the uniform field region in April 2002. Measurements were repeated in Spring 2003 including the fringe field region at the muon entrance region. An Opera 3D field map that matches the measurements was generated for use in simulation and reconstruction of data. The Opera map matches measurements to 2 G in 20000 G in the uniform region, but deviates up to 4% in the entrance region at $z < -200$ cm[40]. Differences between the measurements and the opera map are shown in Figure 2.7.

The effects of the steel from the last two quadrupoles of the M13 beamline were studied using Opera. The map produced from this study was used to estimate a systematic error on $P_\mu \xi$ due to the uncertainty in the magnetic field in the fringe field region.

In 2002 data were taken with the magnetic field set at 1.96 T, and 2.04 T. It has been noted that these $\approx 2\%$ differences in the magnetic field in the tracking region produced much larger differences of $\approx 10\%$ in the fringe field region. This big change in the fringe field is attributed to the saturation of the magnetic field in the end doors of the iron yoke.

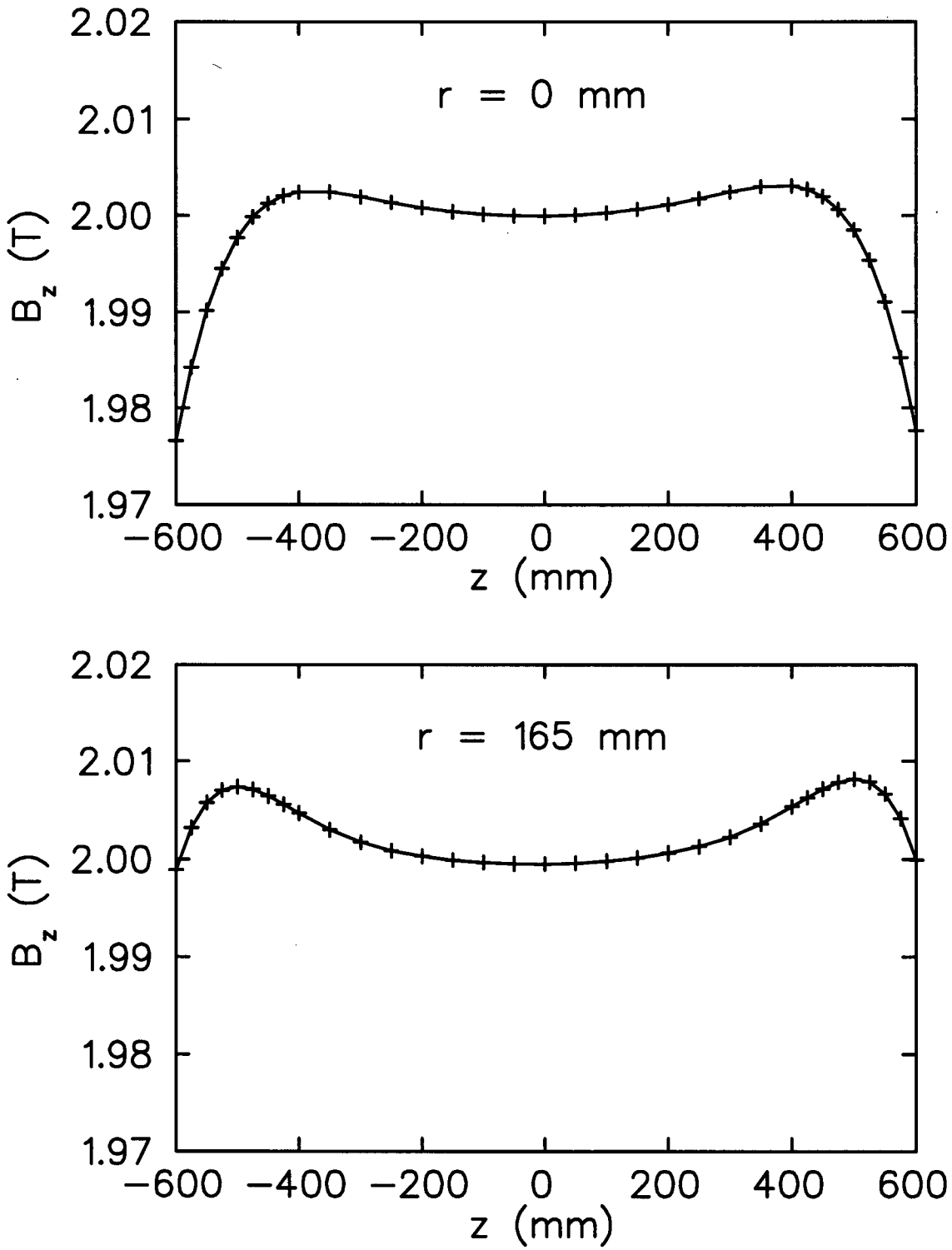

Figure 2.6: Measured magnetic field along the z axis for a radius of 0 cm, and for a radius of 16.5 cm.

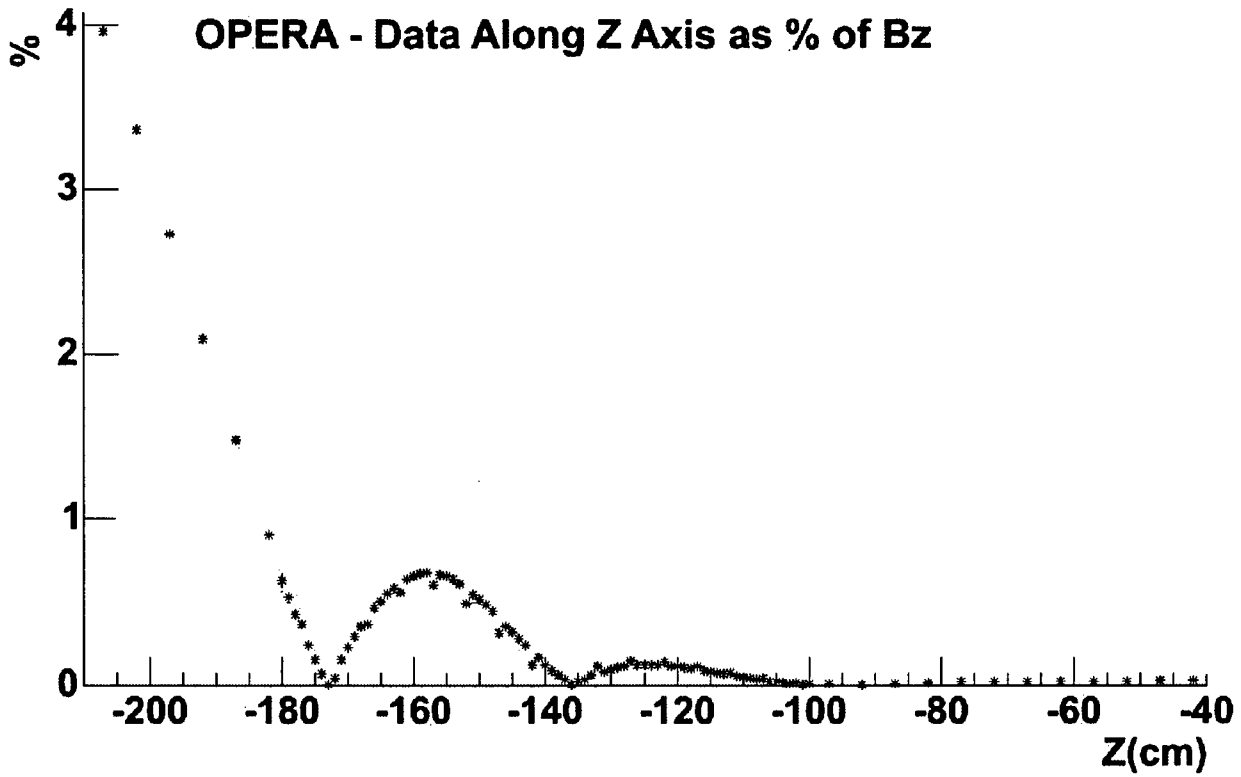

Figure 2.7: Magnitude of the difference between the Opera field map and the measured field along the z axis.

2.5 Cradle and Chamber Spacing

The gas particle detectors used by *TWIST* are mounted in a leak tight aluminum cradle that is filled with 3% N_2 and 97% He gas. Helium, rather than air, is used to reduce the scattering between measurement points and to allow the low energy muons to reach the stopping target at the center of *TWIST*. The precision spacing of the proportional and drift chambers is maintained by precision ground spacers made of a Russian engineered material Sital CO-113M which has a very small thermal coefficient of expansion. The spacers are pushed together by four pneumatic cylinders with a force of 1470 N each to ensure they are touching and do not move. A side view of the cradle, with the chambers spaced with Sital is shown in Figure 2.8.

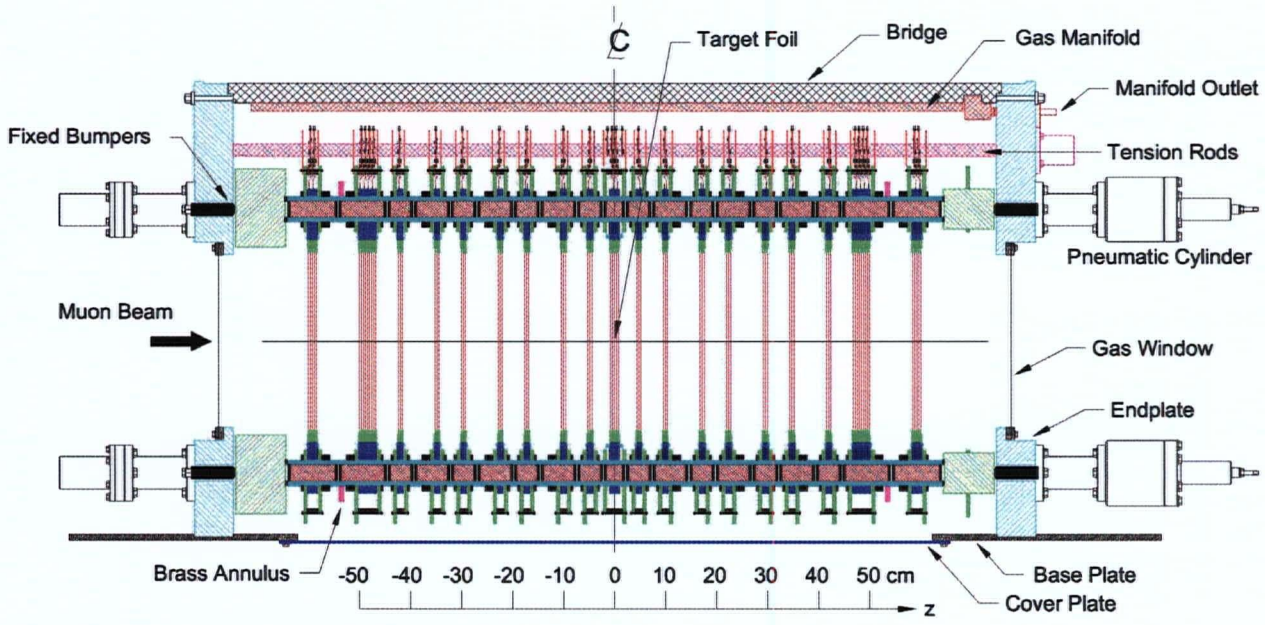

Figure 2.8: Side view of the *TWIST* cradle holding the proportional and drift chambers. (Courtesy of *TWIST*.)

Measurements of the Sitals show that the glass spacers are flat, and that the precision in the z coordinates is good to 2.4 μm over the length of one meter. The precision of the chamber construction has been shown to make the systematic uncertainty due coordinate scale negligible ($< 10^{-5}$).

The spacing of the He/N_2 gaps between drift chamber UV modules is $\sim$ 44 mm or $\sim$ 64 mm. Different spacings are used to help reduce the longitudinal granularity of the detector. Adjusting the position of the cradle is done with both vertical and horizontal screws at the upstream and downstream end of the detector stack. The center of the detector is aligned to the center of the hole in the yoke at both ends independently. The accuracy of this alignment

is better than 0.2 mm at both ends, or 0.1 mrad given the door-to-door distance between the yoke holes of 2.8 m[41].

2.6 Drift Chambers and $\mathcal{TWIST}$ Coordinates

The drift chambers are used to obtain a precise measurement of the position of the positron as it traverses the chambers. To accomplish this a slow drift gas, dimethyl ether (DME), with a small Lorentz angle was used. The Lorentz angle is the angle between drift field and electron drift direction that occurs in a non-zero magnetic field. Each drift chamber consists of 80 gold-plated tungsten anode sense wires of 15 μm diameter, spaced by 4 mm[42]. The cathode foil walls are 6.35 μm of aluminized Mylar, nominally placed 2 mm from the wires. The end view of a DC plane is shown in Figure 2.9.

The coordinate system in $\mathcal{TWIST}$ is defined as follows. The z direction is the line that goes through the center of the upstream and downstream solenoid magnet yoke doors, pointing downstream. The x direction is horizontal and to the left looking downstream. The y direction is vertically upward, making a right-handed coordinate system. The origin of the coordinate system is the center of the target cathode foil. u and v coordinates were defined such that u wires are tilted +45 degrees from the vertical looking downstream, and v wires at -45 degrees.

The drift chambers come in two module types. The first type, a single UV module, consists of a plane of wires along u, and a second plane of wires along v. The planes in a UV module share a cathode as its middle foil. There is a set of seven UV modules on each side of the detector, referred to collectively as the "sparse stack". The second type is an eight detector "dense stack" with the planes V, U, V, U, U, V, U, and V. On each side of the muon stopping target there are seven UV modules and one dense stack module. The DC layers start at $|z| = 44$ mm and end at $|z| = 500$ mm.

The precision with which the wire positions are known in the z direction is better than 50 μm. The average width of the active area is 320 mm, and this width varies by only 6 μm as surveyed for all of the planes. The positions of the foils relative to the wire planes was less well controlled. Measurements on the bench show that the foils can be as much as 250 μm shifted from the nominal 2 mm from the wire plane. This has been confirmed by software, where on average the chamber half-cells are shown to be 1.85 mm and 2.15 mm wide. This will be discussed in more detail in the section on bulge related systematics.

The operating voltage of the DC modules was chosen by measuring their efficiency for registering a hit when a positron track passed through the chamber. Efficiencies were measured using beam positron tracks in zero magnetic field, making straight tracks through the detector. The voltage chosen was 1950 V; as can be seen in Figure 2.10, this is well onto the proportional mode efficiency plateau.

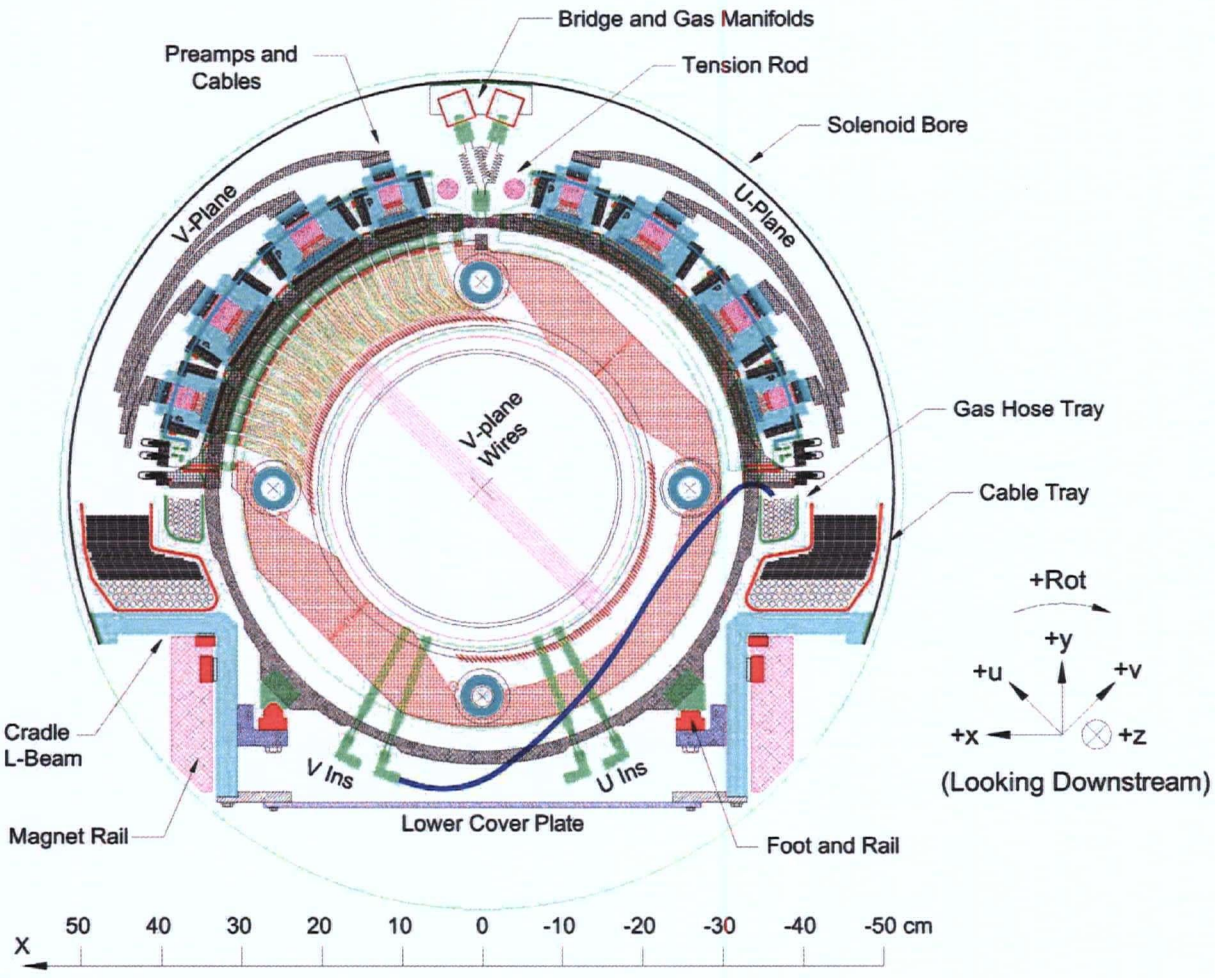

Figure 2.9: End view of a DC wire plane showing the electronics connections to the wires, and gas connections to the module. The coordinate axes used in *TWIST* are shown on the bottom right. (Courtesy of *TWIST*.)

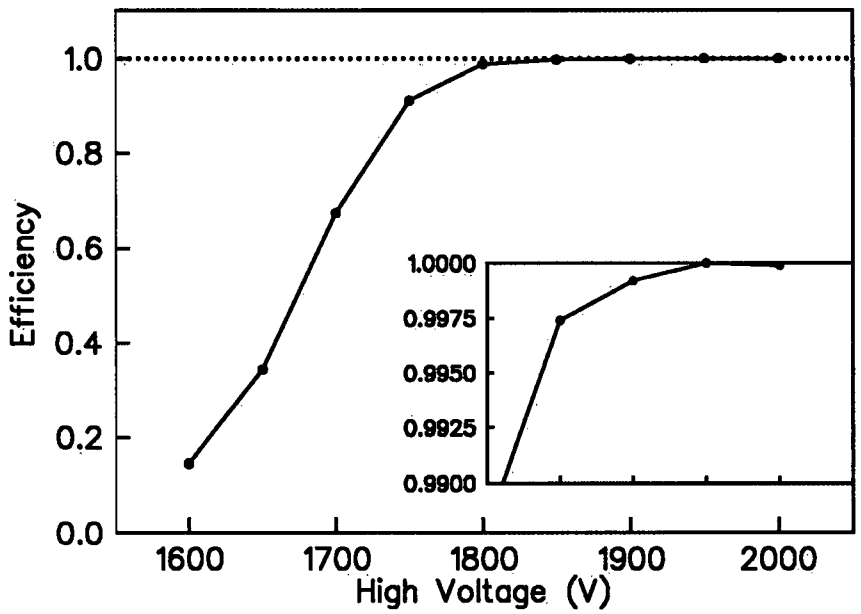

Figure 2.10: Drift chamber efficiency versus high voltage. (Courtesy of *TWIST*.)

2.7 Proportional Chambers

The purpose of the proportional chambers is to have reasonably fast timing information to help with pattern recognition. The width of the TDC signal from the proportional chambers is used in discriminating muons from positrons.

The proportional chambers are similar to the drift chambers, with the exception of the following differences: the proportional chambers use CF_4/isobutane gas, the wire spacing of the proportional chambers is 2mm, and the number of wires in each plane is 160. The PC modules consist of four wire planes oriented in the order U, V, U, V. The proportional chambers are numbered sequentially from furthest upstream (PC1) to furthest downstream (PC12). The two proportional chambers before the the muon stopping target are PC5 and PC6, which measure v and u respectively.

Only the 32 wires closest to the detector axis are readout individually from the outer PC planes (PCs 1-4, 9-12). The other wires of the outer PC planes are readout in groups of four wires summed together. The central 48 wires of the PCs in the target module are readout individually, and the remaining wires are not readout.

2.8 DC and PC Calibrations

Four main calibrations of the PCs and DCs were required: time-zero calibrations, translational alignments, rotational alignments, and alignment to the magnetic field axis.

The time zero calibrations, to remove the electronic and readout delays, were obtained using special data consisting of straight tracks of 120 MeV/c pions. The leading edge of the TDC time spectra for each wire was fit to an error function to determine the timing for that wire. Time of flight was corrected so that the timing of every wire is referenced to the time a muon would reach the target as time zero. The accuracy of the t_0 depends on the wire but is in the (0.5 ns to 2 ns) range, with the average timing good to a few hundred picoseconds.

Alignment corrections were determined using straight line fits to 120 MeV/c pion data. Transverse offsets of the centers of the chambers from the z-axis and the rotations of the chambers from their nominal u and v directions were determined. The translational offsets were measured with a precision of 10 μm, and the rotational orientations were measured with a precision of 0.01°.

Alignment of the detector to the magnetic field axis was done separately for the upstream and downstream halves of the detector. Fits to the decay positron helices with two additional pitch angle parameters were performed to determine the corrections needed. The correction was implemented by shifting the planes in the translational alignment calibration files. The accuracy of the alignment of the magnetic field axis to the chamber axis is 0.02 mrad, but the mismatch between upstream and downstream is 0.1 mrad for the 2004 data.

2.9 Gas System

The gas system used by *TWIST* is designed to maintain the foil positions and gas concentrations by monitoring and controlling the flow rate of the gases. The gas system needs to supply He/N_2 to the cradle, DME to the drift chambers, CF_4/isobutane to the proportional chambers, and He/CO_2 to the gas degrader. The He/CO_2 degrader is described in Section 2.11. Recycling of the PC gas is done as a cost saving measure.

Each mTorr of differential pressure between the cradle He and the chamber DME (or CF_4/isobutane for the PCs) corresponds to a bulge of the foil by 11.6 μm. In order to keep bulges constant to the 50 μm level, the differential pressures need to be controlled to about 4 mTorr.

In order to measure the bulging of the foils in software, a set of data runs with "nominal" 29.6 MeV/c muons was taken with foil bulge set to different values. To obtain these calibrations, the differential pressure between the DCs and cradle gas was adjusted to -30 mTorr, -10 mTorr, 0 mTorr, +10 mTorr, and +30 mTorr from the nominal unbulged settings. More details on how this data is used can be found in the systematics chapter, under the section about chamber bulge systematic effects.

2.10 Muon Stopping Target

The target is the central cathode foil of the PC module at the center of the detector. The target material is high purity aluminum (> 99.999%) measured to be 71 ± 1 μm thick. Since the aluminum was not flexible enough to be tensioned to maintain a flat foil, a special design for the foil was needed. The 150 mm diameter aluminum foil is glued on the edges to fill a 120 mm central cutout in a stretched aluminized Mylar foil. To maintain conductivity of the cathode foil a conductive silver epoxy was used to glue the foils. To avoid problems with sharp edges making high electric fields, pairs of 25 μm masks, with a central cutout of 110 mm diameter, were placed over each side of the aluminum region. The masks reduce the gas gain at these radii, but only the central 96 mm is read out in any case. A sketch of the muon stopping target is shown in Figure 2.11. The center of the detector coordinate system in z is the position half way between the PC6 and PC7 wires. In this coordinate system, the aluminized Mylar cathode foil between PC6 and PC7 is at $z = 60 \pm 50$ μm, and the center of the aluminum disk is at $z = -12 \pm 50$ μm.

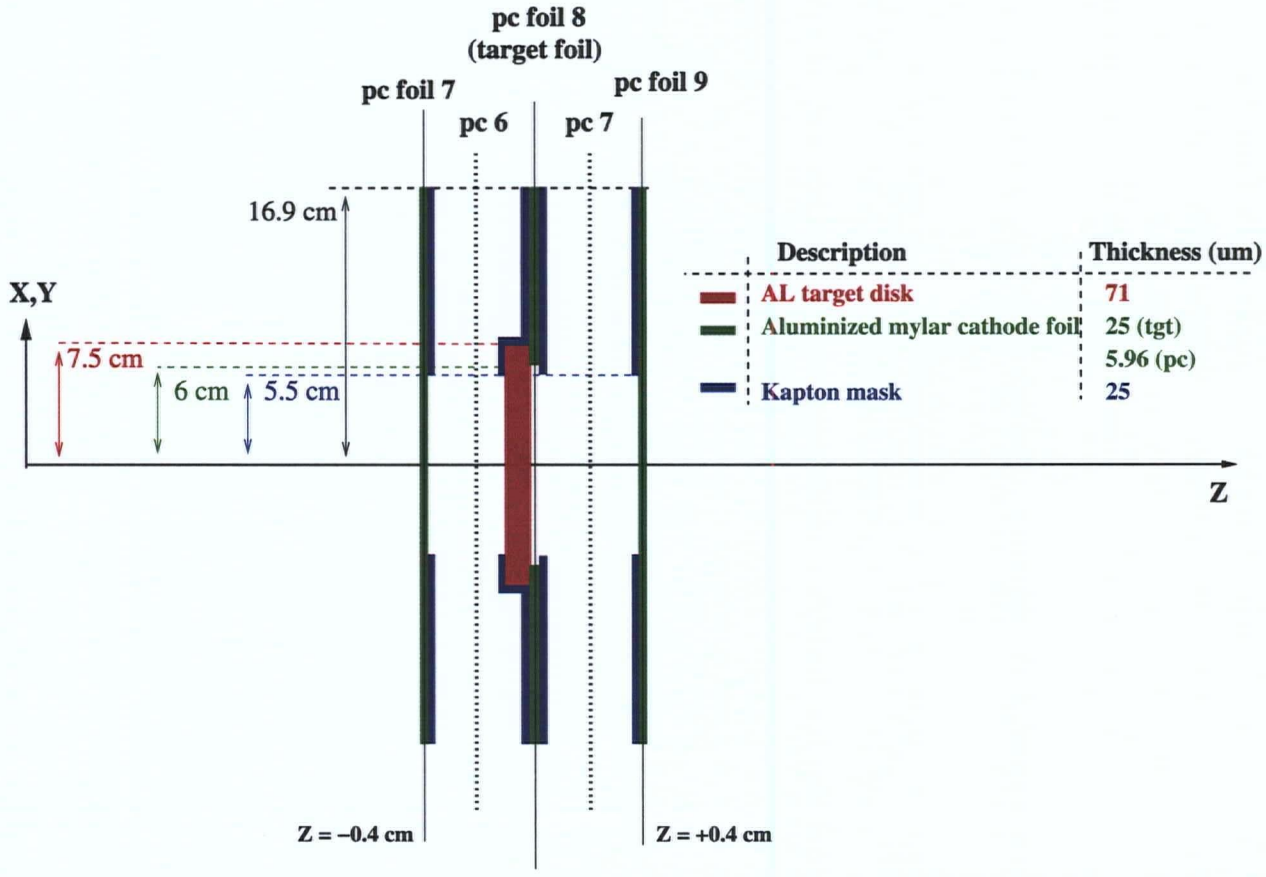

Figure 2.11: Sketch showing details of the aluminum muon stopping target used for data collected in 2003 and 2004. (Courtesy of *TWIST*.)

2.11 Beam Package and Muon Ranging

The surface muons produced at the production target are transported in vacuum through the M13 beamline until they reach the gas degrader, which is well inside the magnet yoke. This allows for keeping the muon spin along the magnetic field lines before any scattering occurs. The exception is a small amount of scattering in an 0.0003 cm thick polyester window valve (WV) in the beamline to stop beam gas (protons, alphas, $^{3}He^{++}$, $^{6}Li^{3+}$, $^{9}Be^{4+}$ [44]). The position and construction of the beam package components is shown in Figure 2.12.

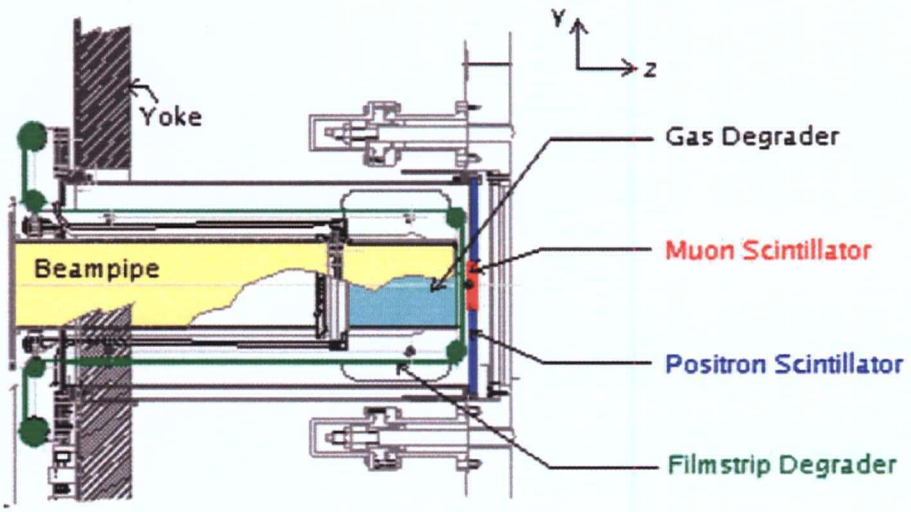

Figure 2.12: Side view of the beam package, showing the placement of the muon ranging He/CO_2 volume, filmstrip degrader, muon scintillator, and positron scintillator all inside the magnet yoke.

The gas degrader is a 21.67 cm long (along z) chamber containing a mixture of He and CO_2 that can be tuned to stop the muons in the stopping target. A typical 2004 data setting to stop muons in the stopping target has the degrader set to 63% He and 37% CO_2 at atmospheric pressure.

A plastic scintillator provides the trigger. The trigger scintillator is a 195 μm thick plastic disk (Bicron BC408) of radius 3 cm located 80 cm upstream of the central stopping target. The light guide is a strip of Plexiglas, the ends of which are attached to a pair of photomultiplier tubes, designated as M1 and M2. The output of M1 and M2 are used individually and as a linear sum, denoted M12. The nominal trigger is a coincidence of M1, M2 and M12.

The positron scintillators are plastic disks (Bicron BC408) with a cylindrical hole through the center to accommodate the muon scintillator. Each positron scintillator has an inner radius of 3 cm, an outer radius of 18.5 cm, and a thickness of 6.35 mm. These scintillators are located just downstream of the muon scintillator. A Bicron fiber (BCF99-AA) wrapped

around the circumference of each scintillator serves as a light guide. The end of each fiber is attached to a photomultiplier tube, yielding four positron scintillator signals.

The filmstrip degrader is a strip of Mylar containing several sites with various thicknesses of degrader material, including a site with no degrader (a hole), one of which is inserted into the path of the incoming muon beam. The nominal setting used the hole in the beam resulting in no additional degrader material. Other settings that were used are discussed in the context of specific data sets. The filmstrip degrader is located 2.5 mm upstream of the trigger scintillator.

The materials that the muon sees, starting from production target to the center of the stopping target are summarized in Table 2.1.

Material	Thickness (mg/cm^2)
Degrader and vacuum foils (incl. WV)	11.91
He/CO_2 Degrader	1.95 to 42.80
Air Gap (2.82 cm)	3.65
Muon scintillator	20.12
Scintillator wrap	3.03
Cradle window	0.88
PC module	9.46
Dense stack	13.41
Seven UV modules	27.80
He/N_2 (63.8 cm)	12.25
Half target module before target	4.31
Half of 71 μm Al target	9.59
Total to center of Al target	118.36 to 159.21

Table 2.1: Estimates of the material thicknesses in mg/cm^2 that the muon sees from the production target to the center of the muon stopping target. If the muon range is 140 mg/cm^2, then this calculation estimates that 53% of the degrader would have to be CO_2.

From the material budget, there is a discrepancy of 6.54 mg/cm^2 from this naive tabulation of materials. In the simulation an additional 12.8 mg/cm^2 of material is needed to match the muon stopping distribution with data. The source of this discrepancy is unknown, but could be due to errors in the thickness estimates of some of the materials or with the energy loss of muons in thin layers of material.

2.12 Time Expansion Chamber and Beam Characterization

The Time Expansion Chamber (TEC), consists of two parts: a drift region and a detection (signal multiplication) region. The basic operation is that a charged particle ionizes the gas along its trajectory. The electrons then drift relatively slowly toward the multiplication region. The further away from the multiplication region the track passed, the longer it takes for the charge to make it to the multiplication region. In the multiplication region, the electrons are quickly accelerated towards a wire, where they begin to ionize more gas molecules. The electrons from these ions accelerate and ionize more gas and so on in an avalanche situation.

The following subsections will describe the TEC layout, the TEC calibration and performance in 2004, and muon beam as measured by the TEC.

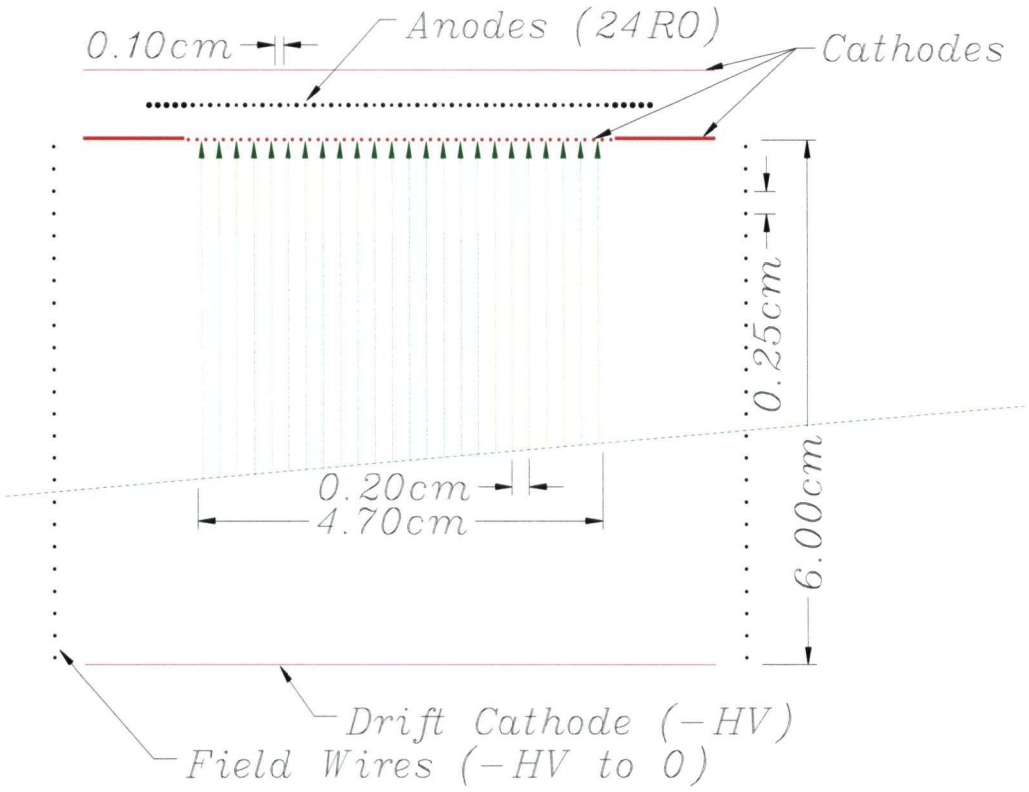

Figure 2.13: Schematic showing a TEC module with dimensions. The initial ionization of a track is shown as a green line, and the drift electrons as green arrows. The z direction is to the right, and x or y is pointing to the top of the page. (Courtesy of *TWIST*.)

2.12.1 TEC Basic Layout

The TEC used for muon beam measurements had two modules: one module measures the x position and divergence in x, dx. The other module measures the y position and divergence in y, dy. Each module has 24 signal wires spaced by 2 mm, with thick guard wires between them in the detection region. The drift region is 6 cm long, and detection region 2 mm wide. A schematic of one of the TEC modules is shown in Figure 2.13.

One important feature of the TEC was its use of a low 60 Torr pressure of DME gas. The low pressure is important to reduce multiple scattering of the low energy (4 MeV) muons. The only thing the muon sees before being measured in the TEC is a 6 μm Mylar foil, the field cage wire plane of the TEC, and the gas in the TEC. A photograph of the TEC modules attached to the low pressure box lid is shown in Figure 2.14.

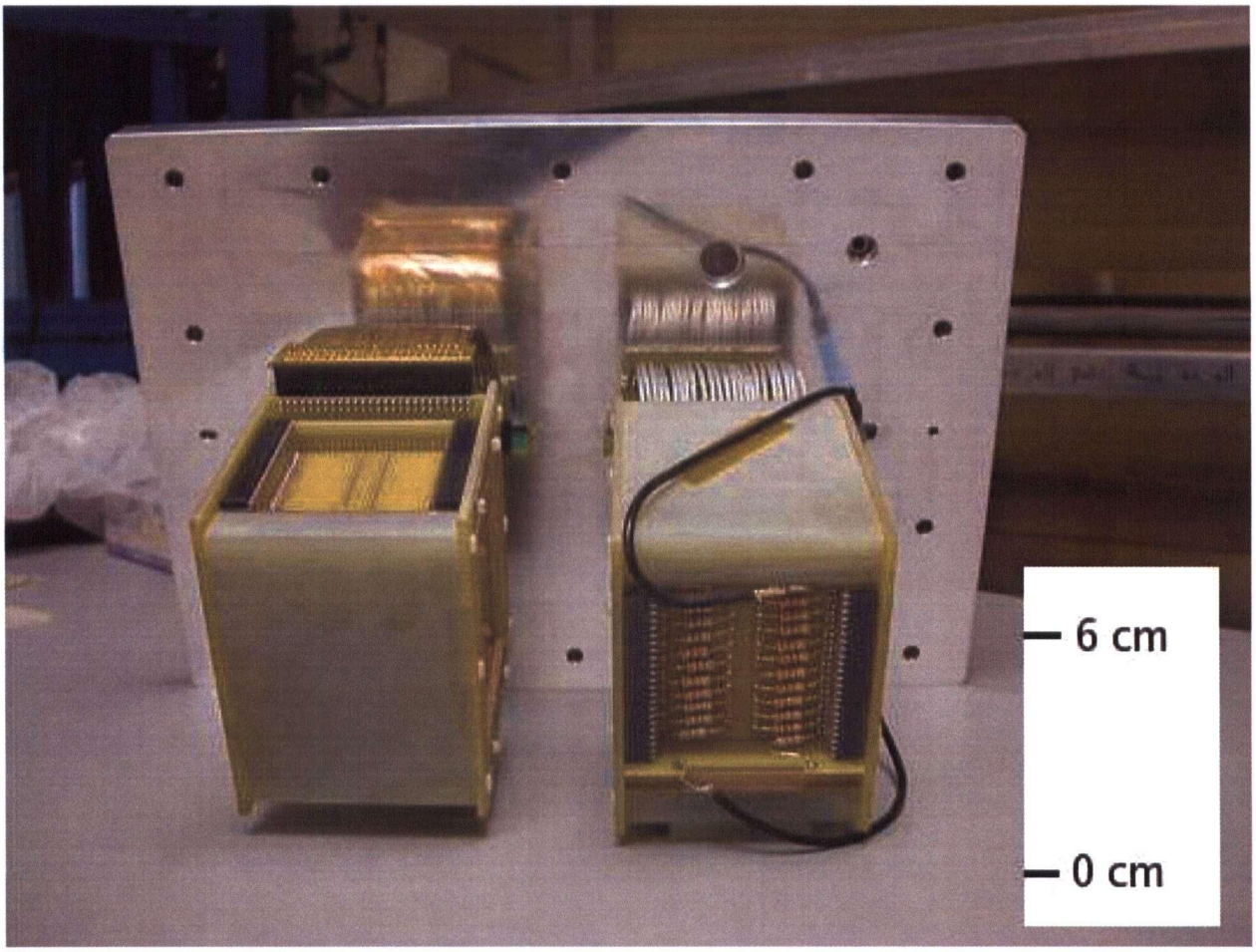

Figure 2.14: Photograph showing the TEC modules and mounting lid removed from the TEC box.

2.12.2 TEC Calibration and Performance

The accuracy of TEC measurements rely on how well the TEC is calibrated, and on how well it is aligned to the solenoid yoke. The TEC calibration procedure was developed as the TEC performance was gradually understood. Table 2.2 gives a list of all the TEC calibrations used for TEC data taken in 2004.

Name	Description
tc_t_0	wire time calibration
tc_twk	time walk correction (width)
tc_str	Garfield space time relation(STR)
tc_cor	Measured corrections to STR
tc_eff	Efficiency versus drift distance
$trig\_t_0$	Global t_0 offset

Table 2.2: TEC related calibration files.

The following subsections present how the trimming of individual wires is done, and the resulting TEC resolution and accuracy. The STR file, which was obtained from a Garfield simulation is not described here[45].

TEC Calibrations

The calibrations (except tc_str) listed in Table 2.2 are applied to correct wire inefficiency, field distortion and edge effects. Data taken with a one hole collimator with 10.0 mm diameter apertures at either end of the TEC box were used for determining the TEC t_0. Near the end of 2004, a four hole collimator was used to obtain STR corrections, and to improve the TEC t_0 measurements. The four hole collimator is shown schematically in Figure 2.15.

STR Correction. The STR from Garfield assumes the geometry and high voltage are perfect, and that there is no distortion of the electric field in one module from the field in the other module. To correct for these effects the collimated data with both modules turned on were used.

The procedure is to histogram the drift time for all wires. The mean drift times, t_i, and drift distances d_i for the three holes in each direction are plotted along with the Garfield drift time at $d_4 = 4.5$ mm ,t_4, which is the location of grid plane. Using this point assumes that intermodule field interference doesn't affect the amplification region. A fit is done to (d_i, t_i) using a 2^{nd} order polynomial function:

$$t_i = t_4 + a_1 \cdot (d_i - d_4) + a_2 \cdot (d_i - d_4)^2 \quad (i = 1, \cdots, 4) \tag{2.3}$$

Figure 2.16 is an example of the fit for wire 1 of the x module.

STR corrections are calculated for each of the forty-eight sense wires, and these are entered into the STR correction file. Since we did not have the four hole collimator data

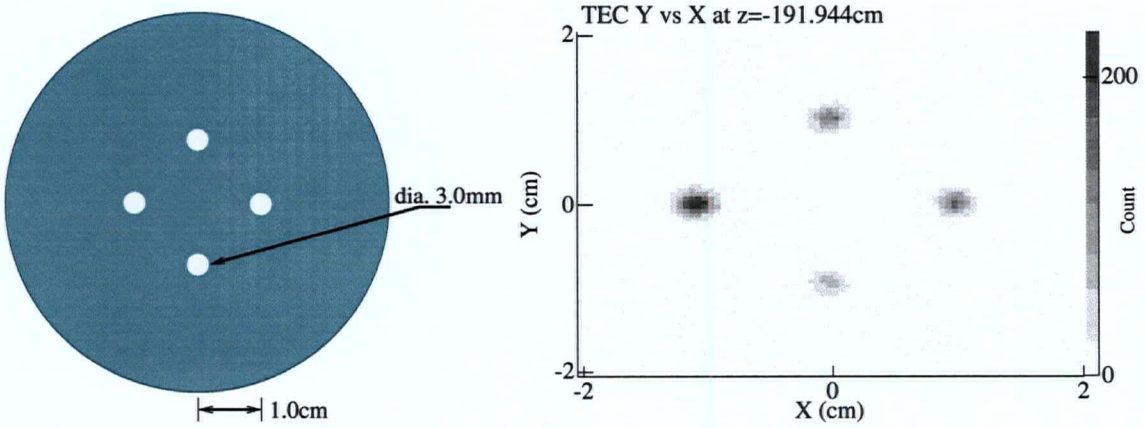

Figure 2.15: A schematic drawing of the collimator is given on the left, and the four holes reconstructed from data run 20718 are shown on the right.

with the solenoid on, we have assumed that these corrections are unchanged by the solenoid field.

TEC Efficiency Correction. The TEC had a lower efficiency for long drift time hits. A possible explanation is that due to diffusion of the ionization, a cluster could fail to register if it had to drift too far. The four hole collimator data are used to measure the efficiency as a function of the drift distance.

The calibration procedure is to histogram the number of hits on a beam track seen by TEC. For each hole, we obtain the mean number of hits, N_{mean} and plot this versus the mean drift time or distance. Figure 2.17 shows the relative efficiency as a function of drift time.

2.12.3 Uncertainties in TEC Measurements

The final uncertainty in the TEC measurements depends on the precision of the TEC calibrations and alignments. An estimate of the precision of the TEC measurement must include the alignment of the TEC chamber to the yoke and the alignment of the collimator to the beam line. This section describes the estimates of the systematic uncertainties or offsets in the TEC position and angle measurements.

t_0 calibrations. For the 3.0 mm hole collimator data the uncertainty in timing is $\sim$ 2.0 ns. For the 10.0 mm hole collimator data, the uncertainty is $\sim$ 15 ns, which corresponds to 150.0 μm.

There are some structures in the t_0 distribution that are not understood. These structures could introduce +2.0 mrad and +4.0 mrad offsets in the dx and dy divergence measurements if the structure is due to a misalignment of the apertures of the collimator.

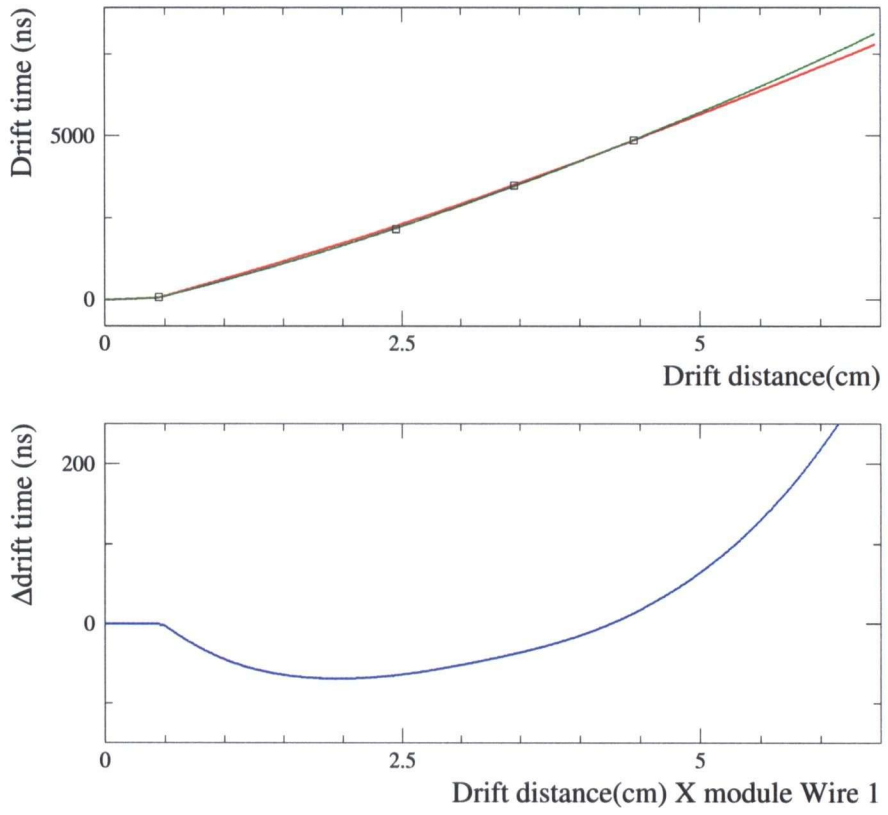

Figure 2.16: The top plot shows the data derived STR in green and the Garfield calculated STR in red. The open boxes are the measured drift times. The bottom plot shows the difference (data derived STR - Garfield calculated STR).

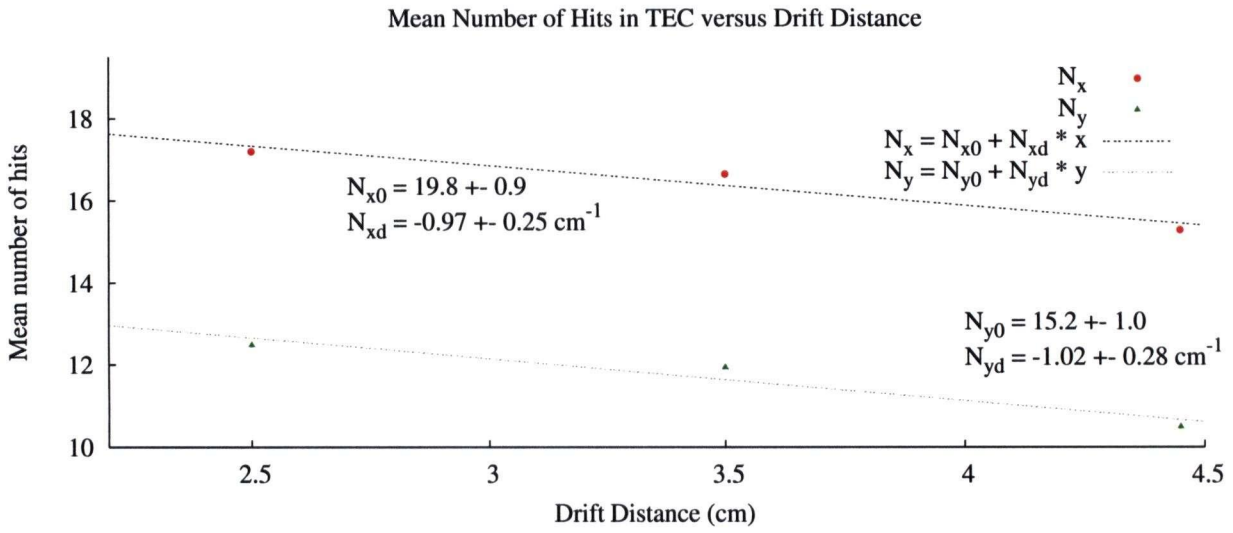

Figure 2.17: TEC efficiency calibration. N_x and N_y stand for mean values of the number of hits used in the track, fitting in the x and y modules, respectively.

STR. When deriving an STR from data, we borrowed a fourth point, (d_4, t_4), from the Garfield simulation since we do not have enough points for the STR extraction from the data. This gives us an uncertainty of about 300.0 μm in the position measurement, and about 1.0 mrad uncertainty in the angle measurement.

A big uncertainty comes from the STR variation when the gas temperature changes. The drift times for different temperatures for a drift distance of 3.45 cm are shown in Figure 2.18. The figure shows that a change of 3 to 5^0C in temperature could cause a shift of 0.5 to 1.0 mm.

Fortunately, all the TEC runs were taken within a short time so that the temperature variations were small. The uncertainty in beam position due to temperature variations is estimated to be < 200.0 μm.

Analysis algorithm. The TEC track fitting code could also produce a bias in the measurements because of the tracking algorithm employed. A Monte Carlo study with the wire inefficiency simulated and the multiple scattering turned off shows the uncertainty due to this effect is about 50 μm in position and < 1.5 mrad in angle.

TEC resolution. For some runs, the RMS of the residual distributions increases with wire number. This run-dependent resolution is found to be due to a loss of TEC efficiency with time. Figure 2.19 shows the resolution versus wire number for different numbers of hits.

Even with this feature, the resolution is better than 500 μm even on the worst wires. An average resolution for tracks with more than 9 hits is about 250 μm.

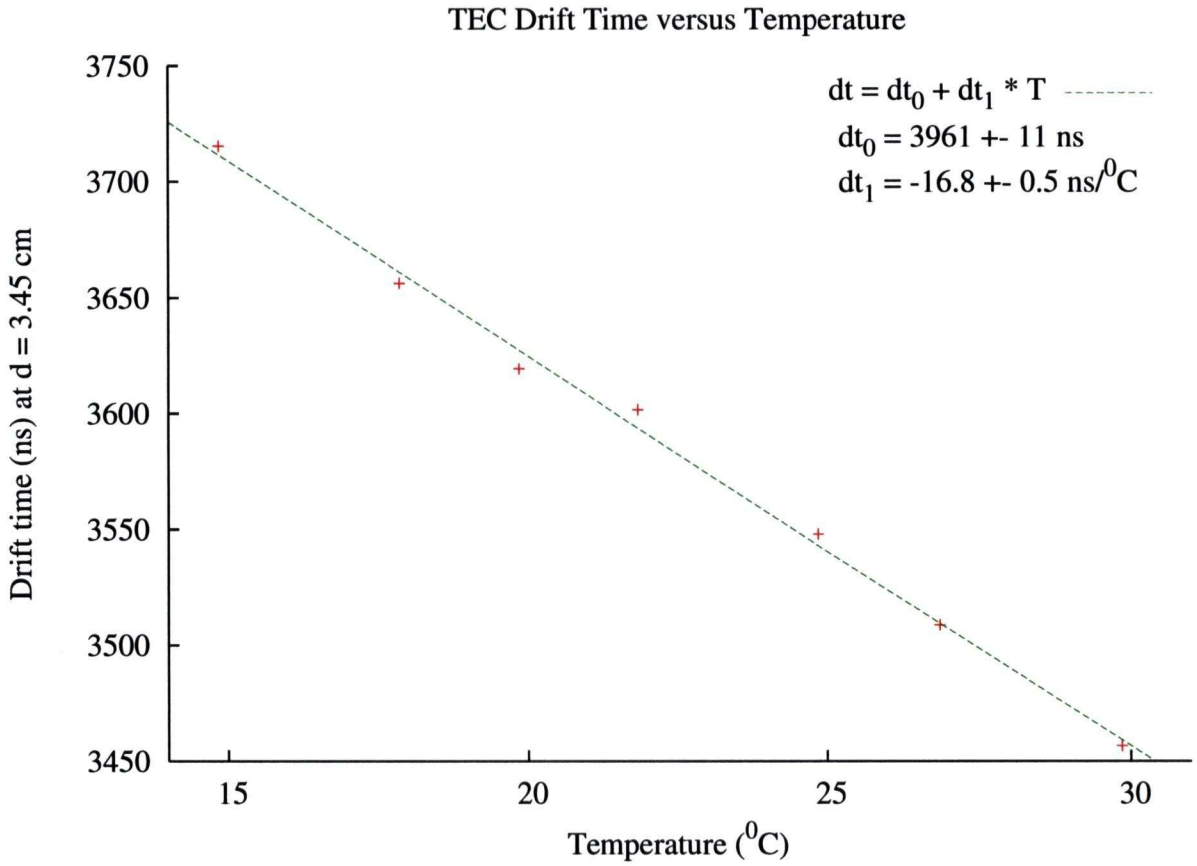

Figure 2.18: TEC drift time *vs.* gas temperature.

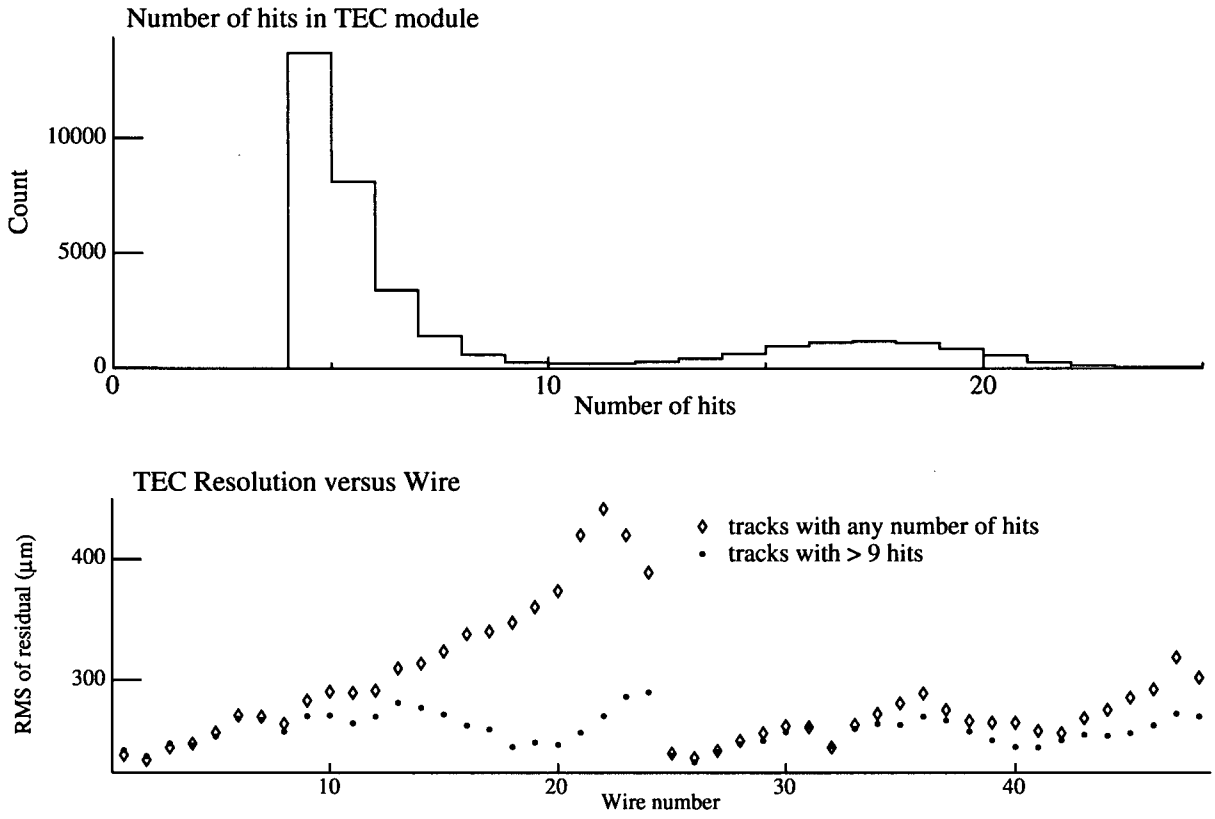

Figure 2.19: Resolution of TEC track fitting. The number of hits on a track is shown in the right. The resolution for all tracks (open diamonds) and for tracks with $N_X > 9$ (solid points) is in the bottom plot.

Multiple scattering in the TEC. An observed problem is that the resolution of the angle measurement is degraded by almost a factor of 2 due to multiple scattering. The muon is scattered by the TEC window and 2.45 cm DME gas before it reaches the TEC x module. This smears the divergence distributions, dx and dy. The problem is reduced somewhat by applying a deconvolution to the angle distributions measured by the TEC. The deconvolution is applied in the simulation, where the dx and dy distributions are generated as Gaussian, with a different mean and sigma, for each bin in x and y. The "Gaussian deconvolution" is used to approximate the real beam by multiplying the sigma used, for dx and dy, by separate "deconvolution" factors. The values used for the analysis in this thesis are 0.615 for dx, and 0.444 for dy.

Alignment of the collimator. Two apertures, one mounted on the entrance window of the TEC box and the other on the exit window, form the collimator used to align the TEC sense planes. Any noticeable shift or rotation between the apertures will deteriorate the tc_t_0 calibration and STR correction, and further introduce a bias in the TEC analysis. The uncertainty in the alignment of the apertures is around 500.0 μm[46].

Alignment of TEC to the drift chambers. The absolute alignment of the TEC relative to the solenoid yoke was done using cross hairs installed on either end of the TEC box, and on either end of the yoke end holes. The uncertainty on these measurements is about ± 0.2 mm, which corresponds to aligning the angles to ± 1 mrad. Measurements with a total station to confirm this alignment gave similar uncertainty on the measurement of the position of the TEC.

There are a number of issues that introduce additional systematic uncertainty on the TEC alignment. One issue is that the initial alignment of the TEC was done before turning on the solenoid field. When turning on the solenoid field, the TEC alignment was disturbed by the flexing of the solenoid yoke door (to which the beam package including TEC were bolted). A second issue is that pumping down the beamline moved the TEC. The position of the upstream and downstream end of the TEC looking upstream before and after the production data taking, and under vacuum load are shown in Table 2.3.

Based on the comparison between before and after running, one could say that the position alignment is changed by 1.8 mm, and the angle by at most 4.3 mrad. This seems like a reasonable number to quote as the uncertainty in the position of the TEC relative to the yoke.

TEC measurements during solenoid field ramping At the end of the 2004 runs, some TEC data were taken during the ramping down of the solenoid field. Those data show that the solenoid field, in addition to having some complex effects on the TEC data, also had an effect on the M13 beam optics. The effect of the solenoid field on the beam is shown in Figure 2.20.

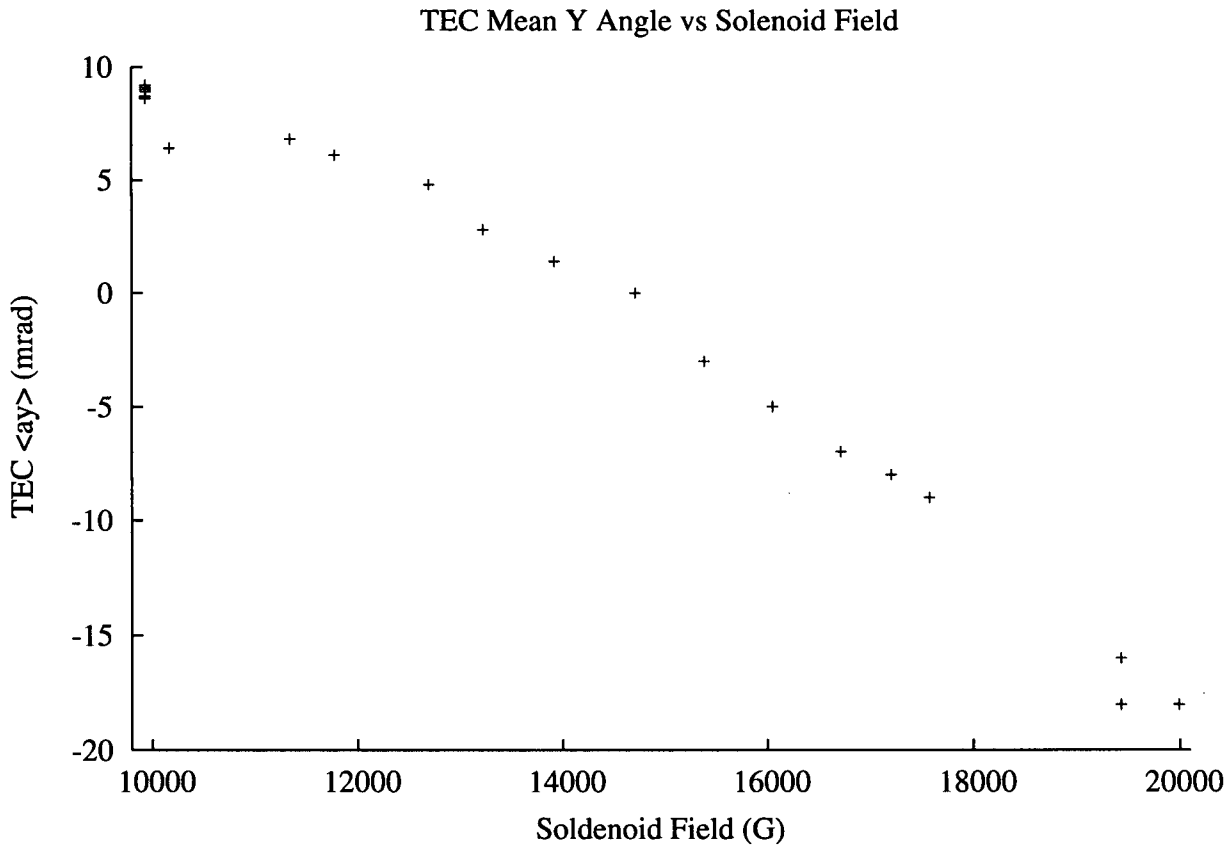

Figure 2.20: Effect of the solenoid field on the muon beam divergence in y, dy, as measured with the TEC.

	Before		After	Before-After
Position	Vented	Vacuum	Vacuum	Vacuum
Upstream x (mm)	+0.2	-1.2	-0.3	-0.9
Downstream x (mm)	0.0	-1.8	0.0	-1.8
dx (mrad)	-0.7	-2.1	1.1	-3.2
Upstream y (mm)	0.0	0.0	1.0	-1.0
Downstream y (mm)	+0.3	+0.5	-0.3	0.8
dy (mrad)	1.1	1.8	-2.5	4.3

Table 2.3: Measurements of the position of the center of the TEC upstream and downstream ends relative to the center of the holes in the yoke door. A positive number means, looking upstream, the center of the TEC is to the right or above the center of the yoke hole. The divergences dx and dy are the angular misalignments in x and y from the z axis respectively.

Overall Estimate of TEC Uncertainty Based on the estimates given in this section, the total uncertainty in the TEC measurements is estimated to be better than 2 mm in x and y, and better than 5 mrad in dx and dy. These numbers can be used along with sensitivity estimates to obtain a systematic error due to the fringe field depolarization of the beam.

2.12.4 Muon Beam as Seen by the TEC

The muon beam was measured for each of the data-taking conditions used for the 2004 data collection. The measurements were done with the solenoid field on and the results were output at the center of the TEC. These same beam profiles were used, starting at the center of the TEC, in a GEANT simulation of the data. The beam profile corresponding to the nominal 2004 datasets is shown in Figure 2.21

Details on the sensitivity of $P_\mu \xi$ to the uncertainty from this beam profile are discussed in Section 6.1.3.

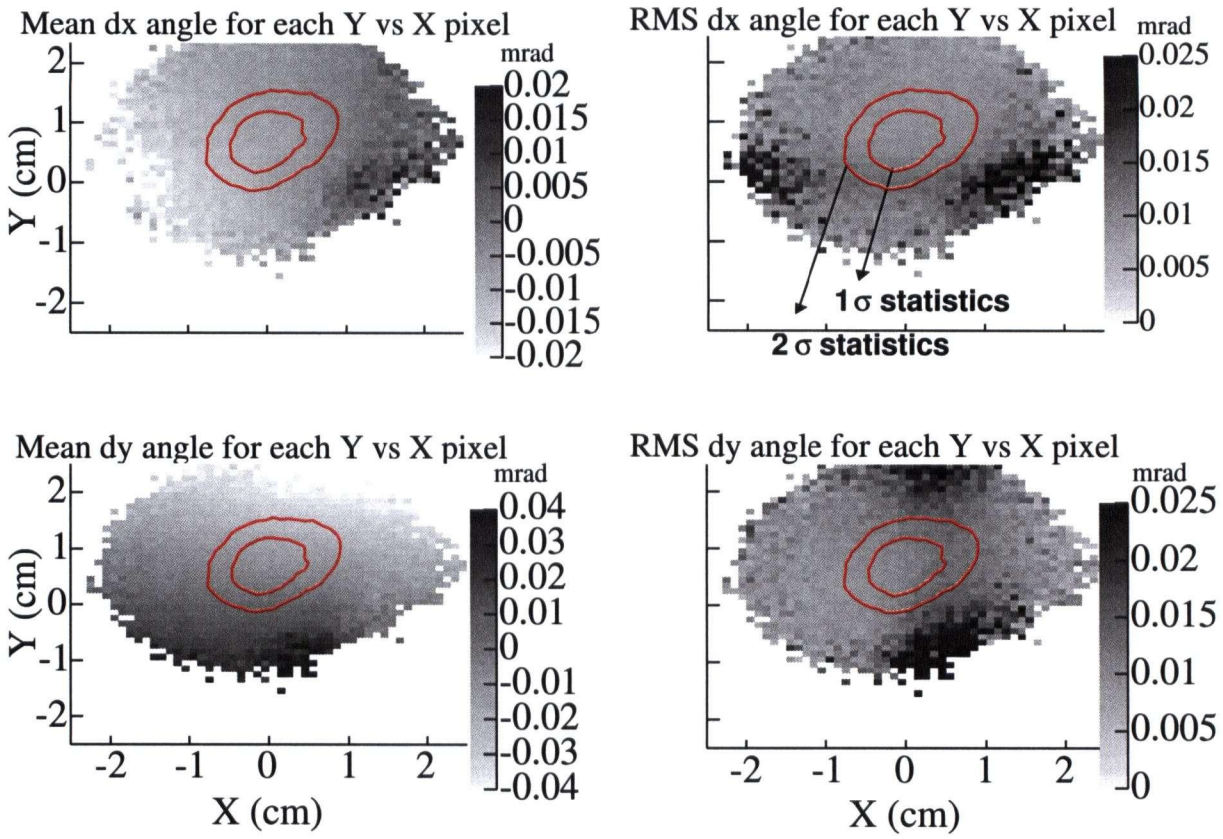

Figure 2.21: Plots showing the muon beam as seen by the TEC. The top plots show the divergence (mean and RMS angles) of the beam in x for each xy pixel. The bottom plots show the divergence of the beam in y for each xy pixel. The black contour lines indicate the size of the beam; the inner black contour contains 66% of the beam, and the outer contour contains 90% of the beam.

2.13 Electronics and Trigger Logic

Events in *TWIST* are recorded by LeCroy Model 1877 Time to Digital Converters (TDC) distributed in two Fastbus crates. The TDCs record the digitized time since a start gate in 500 ps bins, and can record up to 16 hits over a 32 μs period. The TDC read-out and trigger are setup to obtain hits from 6 μs before to 10 μs after a muon hits the trigger scintillator. For each wire hit, the TDC records a pulse start and stop, and thus can be used to calculate a pulse width. In this configuration up to eight wire hits can be recorded for each wire in any triggered event [47].

The event is triggered by the muon scintillator whose threshold is set high enough to reduce the beam positron trigger rate, but low enough to trigger most beam muons. Two photomultipliers, labelled M1 and M2, are read out from the single muon scintillator. M12 is the linear sum of the signals from M1 and M2. The muon trigger is a coincidence of M1*M2*M12, where the M12 signal defines the timing. The muon trigger then comes from the coincidence labeled M. The discriminated signals M1D, M2D, and M12D are all sent to TDCs to record the time relative to a start gate. The trigger signal (TRIG) is disabled if the Fastbus TDCs are busy (FBBUSY), or if there is another muon less than 15 μs after the trigger (TRGT). A schematic of the trigger logic is shown in Figure 2.22. The time of the M1 and M2 signals discriminated with a lower threshold (M1LD, M2LD) are also sent to TDCs.

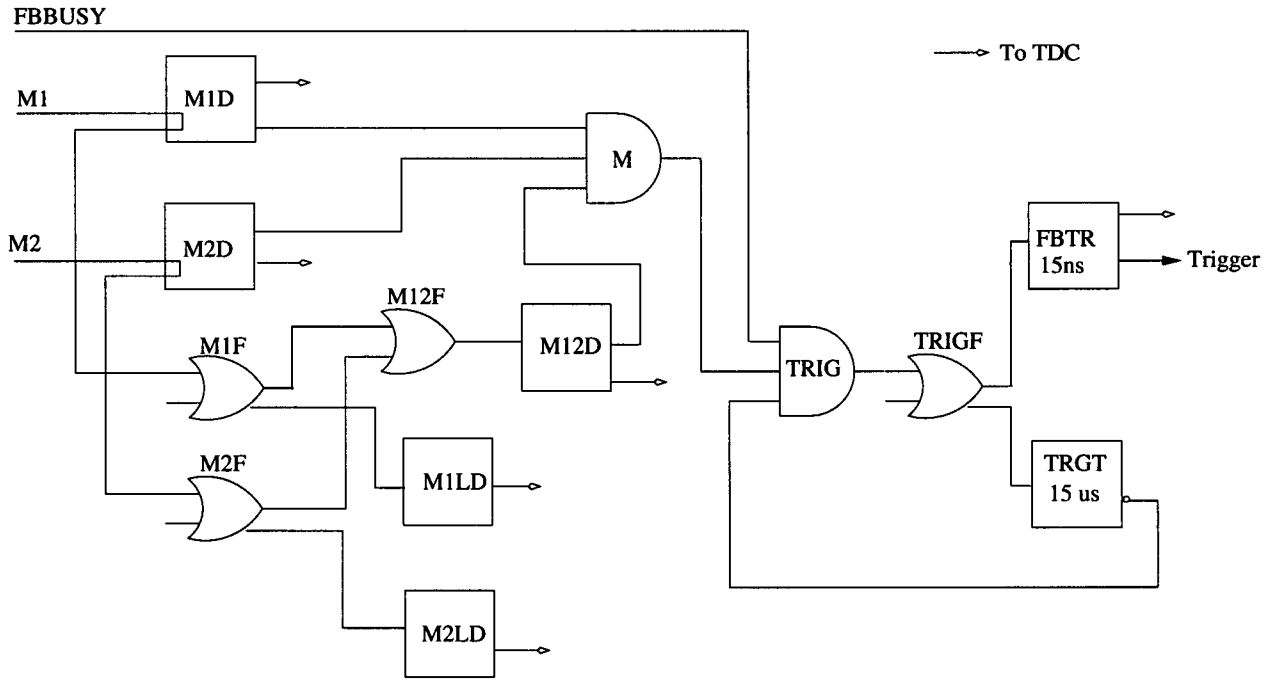

Figure 2.22: Schematic diagram of the trigger logic.

Part II

Analysis, Data, Simulation, and Systematic Effects

Chapter 3

Michel Spectrum Analysis Strategy

A key philosophy of the analysis strategy is to remain blind to the final answer until all of the steps in the analysis are validated and the most serious bugs have been fixed or understood. By doing a blind analysis the final answer cannot be biased by any preconceptions of the experimenter. In this chapter the method used to do a blind analysis, and how the data are processed is described.

3.1 Analysis Flow

A broad overview of the analysis, from raw data to muon decay parameters, is discussed in this section. In trying to extract muon decay parameters the detector response including acceptance, and physics effects need to be included. The method chosen to account for these effects was to fit a data distribution, in decay positron $\cos\theta$ versus total momentum, to a similar distribution from analyzed simulation data. By using the same analysis code on the data and the simulation, any biases in the analysis code will cancel to first order. Fitting to simulation will give the correct answer to the degree with which the simulation can be shown to agree with reality.

The fitting of data to simulation exploits a feature of the muon decay differential rate in Equation 1.14. The important feature is that the decay rate is linear in the parameters $\lambda = \{\rho,\ \eta,\ P_\mu\xi|_{P_\mu\xi\delta},\ P_\mu\xi\delta\}$, where the bar on ξ means that it is considered with $P_\mu\xi\delta$ held constant. Using this fact we can write the measured decay rate in terms of a simulation decay rate with hidden values of the muon decay parameters (λ_{sim}) as:

$$\Gamma_{\text{Data}}(\lambda) = \Gamma_{\text{sim}}(\lambda_{\text{sim}}) + \sum \frac{d\Gamma}{d\lambda}\Delta\lambda, \tag{3.1}$$

where $\Delta\lambda = \lambda - \lambda_{\text{sim}}$ is the difference in the true muon decay parameter from the hidden simulation muon decay parameter, and $d\Gamma/d\lambda$ are the derivatives of the muon decay spectrum with respect to each parameter. More details on the spectrum fitting can be found in the thesis of A. Gaponenko[48].

In order to fit differential decay rates in the way described above, simulation of both an ordinary muon decay distribution with hidden muon decay parameters, and each of the derivatives needs to be generated. The fit is done using six two-dimensional histograms of $\cos\theta$ versus total momentum. The six histograms consist of: one data histogram, one simulation histogram, and four derivative histograms. Since our detector is not very sensitive to the parameter η, the fits are often done with η fixed to the Particle Data Group (PDG) value, and thus the fitting only needs five of the six histograms.

The steps taken to go from a raw data file or raw simulation file to the distributions of positron momentum and angle needed for the spectrum fits are:

- unpacking hits,
- sorting hits in time to make time windows,
- classifying the types of tracks in the windows,
- classifying the overall event type,
- sorting hits in space to make clusters,
- making an initial guess for the positron helix parameters,
- doing a wire center fit for the helix parameters,
- doing a full drift fit for the helix parameters,
- creating a root tree of the classification and fit results,
- analyzing the root trees to apply the final cuts and select the tracks,
- determining the energy calibration using the endpoint of the decay positron spectrum, and
- applying the energy calibration in a reanalysis of the root trees.

The steps itemized above are detailed in the remaining sections of this Chapter.

3.2 Unpacking

Raw data unpacking routines read the data from the DAQ output files which are written in YBOS format. Signal timing and widths are read for hits from the scintillators, PCs and DCs. Signal times are adjusted to account for electronic timing offsets using t_0 calibration files. Wire positions and angles are adjusted according to translational and rotational correction files.

For real data the identification and removal of electronic crosstalk hits is done. A hit is identified as crosstalk if, on a nearby wire, it produces a narrow signal a short time after a good hit. A good DC hit is defined to be at least 50 ns wide and a good PC hit to be at least 60 ns wide. A DC crosstalk hit occurs 5 ns to 60 ns after a good hit, and a PC crosstalk hit occurs 5 ns to 65 ns after a good hit. The width of the pulse is considered narrow if it is less than 50 ns wide, and more than 60 ns narrower than the good hit. The PC hit is narrow if it is less than 40 ns wide, and more than 60 ns narrower than the good hit. The nearby wire must be within 10 wires for the DC, and within 32 wires for the PC crosstalk.

3.3 Pattern Recognition and Event Classification

This section summarizes the method used to perform pattern recognition on data and simulated data implemented in the *TWIST* analysis package called MOFIA. The algorithm used for sorting the TDC hits into the MOFIA "time window" structure is also presented.

The algorithm can be broken up into the following steps, in the order in which they are done:

- calculate TDC hit statistics in different time bins,
- set window times,
- look for outlier noise hits at large radii,
- calculate TDC hit statistics in window times,
- calculate start and stop planes and try to tag possible cosmic ray,
- match scintillator hits to windows,
- assign hits to the window structure,
  - evaluate window types one at a time,
  - review window types looking at whole event,
  - assign hits to window,
- cluster hits in space, and
- decide on overall event type.

Most of the items above will be discussed in their own subsection in the remaining portion of this section.

3.3.1 Calculating TDC Hit Statistics in Bins of Time

The first step is to calculate several different statistics on TDC hits, binned in time. The size of each time bin was chosen to be 50 ns, so there are a total of 321 time bins from -6000 ns to 10000 ns. The statistics calculated are stored in separate structures for the PCs and DCs. The structure for each time bin contains statistics on average and RMS u and v positions, timing information, and the first and last planes hit.

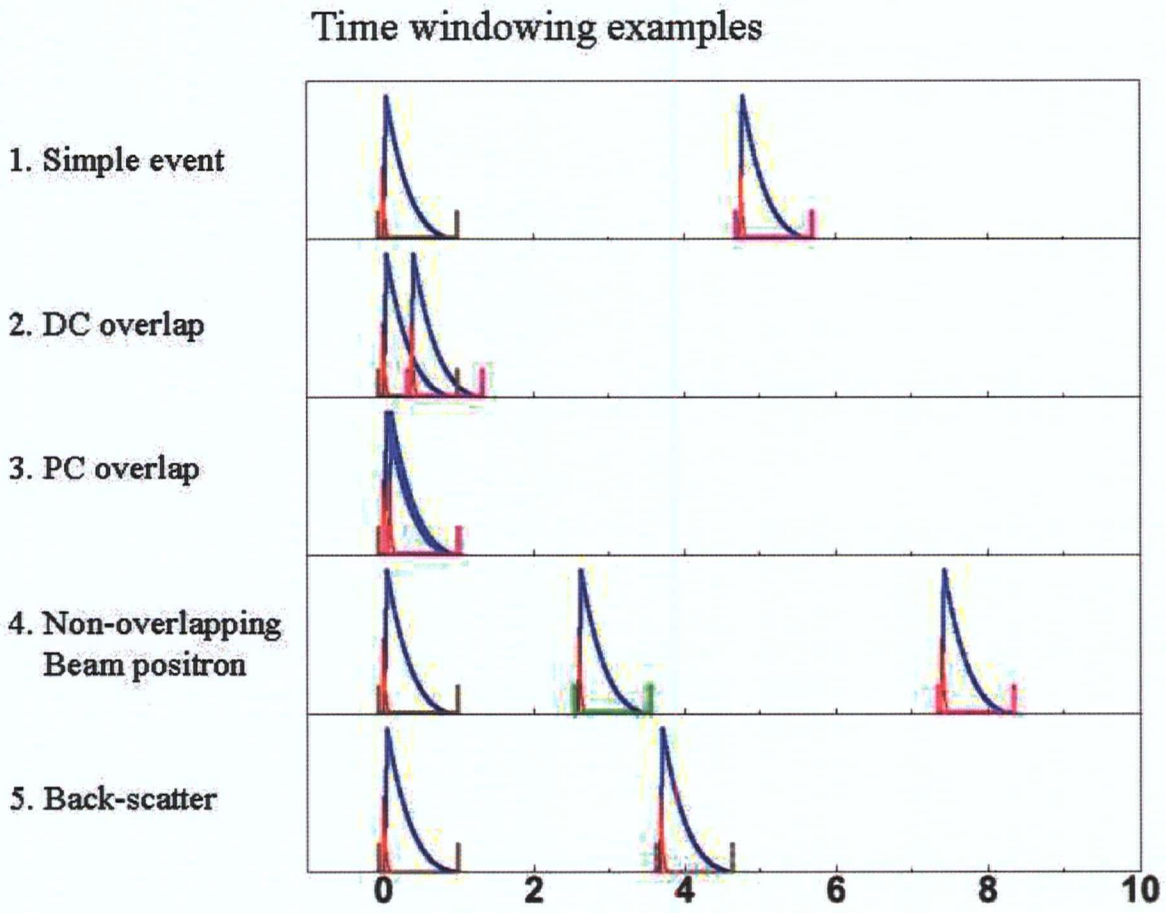

Figure 3.1: Examples of how events are split into different time bins (windows). The red lines represent the times of PC hits, and the blue distributions represent the times of DC hits. The grey lines represent muon windows, the pink lines represent decay positron windows, and the green lines represent beam positron windows.

3.3.2 Set Window Times

A time window is used to separate track hits in time. This is done by looking for peaks in both the PC and DC time bin hit count statistics. Most of the time only PC time bin statistics are used, but occasionally DC statistics are used. For illustration purposes, the timing of hits in the PC and DC chambers in some typical events is shown in Figure 3.1.

The algorithm usually ignores single PC hits, unless there are lots of DC hits at the same time, and there has not been any other particle for 1050 ns.

The algorithm loops over the time bins, and decides if a given time bin should make a new window, or be added to an existing window. The decision is made in two steps. In step one if there is more than one PC hit in the time bin then we look to see if this is a continuation of an already started track. It is a continuation when: the first and last PC hit

in this time bin are in the same plane and have TDC widths less than 40 ns, or if there are fewer than four hits in this time bin with width less than 40 ns and within 8 time bins of the last PC time bin. Otherwise if the time bin has more than 3 DC hits, more than 3 PC hits, or more than 3 DC hits in each of the next three time bins then we go on to step two. If there is one PC hit in the time bin, then we look to see if the second step has told us the next time bin with hits will be a new track and that there are more than 10 DC hits in this time bin with width > 40 ns to send the time bin on to step two. A check is made to not make a new window if this time bin's minimum PC time is within 200 ns of the first time for this track. Another check is made to see if this time bin's minimum PC time is later than 1050 ns of the first time for this track.

For step 2 there are two cases. The first case is if we already think this is a new track, then we start a new window. The second case is more complex, and it is here that we try to decide if this is a continuation of the previous track or a new one. Essentially the algorithm looks to see if a peak in the hit count has been reached. Once a peak is reached, then we do not start a new window unless there is another peak more than 150 ns away.

When a new time window is started the number of PC windows found is incremented, and information about the tracks found are stored in a structure containing information about the timing. For each of these PC windows, two entries in the window structure will be made. The even window and odd window before it will have the same start and end times, and are meant to try to separate the hits in space. The even window will contain the decay positron hits, and the odd window before it the hits that did not belong to any time window with a track.

3.3.3 Look for Outlier Noise Hits at Large Radius

The idea is to try to ignore a few outlier hits that are more than 5 cm in u, v from the bulk of the other hits. The decision to make this cut is done separately for the upstream and downstream halves of the detector. The hit cut was implemented based on observation of a few rare events in data that were misclassified without removing a noise hit.

3.3.4 Calculate TDC Hit Statistics in Window Times

A loop through the TDC hits for each time window is made to calculate some average quantities to help later in deciding what is contained in each window.

3.3.5 Assign Hits to the Window Structure

In order to assign hits to the window structure, we need to have an idea of what the track or tracks are in the window. To do this we first evaluate window types, one at a time, then make corrections looking at the whole event. Then we can try to separate the hits so that mostly decay positron hits are in an even window, and any hits that overlap in time are put in the previous odd window. The following subsections describe the window types, and hit assignment to windows.

Evaluate Window Types One at a Time

A summary of the window types, and a short description of what the window type represents is presented in the following subsections. This decision process is complex, and the descriptions given here are only approximate. The *window types* are:

1. Muon
   Only a muon with possible deltas or hard scattering appears in this window.

2. Upstream Decay
   Only an upstream decay with all hits on the upstream side of a muon decay appear in this window.

3. Downstream Decay
   Only a downstream decay with all hits on the downstream side of a muon decay appear in this window.

4. Beam Positron
   Only a beam positron in this window.

5. Empty
   An odd window, which may contain hits which do not appear to be from a muon or decay positron track.

6. Overlap involved
   PC time between two tracks of more than 200 ns, more than 1.5 hits per plane, no muons yet or in track.

7. Upstream Decay (DS delta removed)
   Upstream decay with additional downstream hits that are concentrated around one u, v positron (within 0.5 cm RMS).

8. Downstream Decay (US delta removed)
   Downstream decay with upstream hits that are concentrated around one u, v positron (within 0.5 cm RMS).

9. Upstream Decay (Scatter back downstream)
   Upstream Decay that has hits on both sides of muon stop (upstream and downstream of the muon stop). There needs to be more than 5 hits per plane upstream, more than 15 hits in a particular plane, or more than 80 hits in any group of 8 planes.

10. Downstream Decay (Scatter back upstream)
    Downstream Decay that has hits on both sides of muon stop. There needs to be more than 5 hits per plane downstream, more than 15 hits in a particular plane, or more than 80 hits in any group of 8 planes.

11. Muon and Fast Decay Downstream
    Appears to be a muon with a fast decay downstream within 200 ns.

12. Muon and Fast Decay Upstream
    Appears to be a muon with a fast decay upstream within 200 ns.

13. Muon and beam positron
    Appears to be a muon and a beam positron within 200 ns.

14. Upstream Decay (DS part of beam e+ removed)
    Appears to be an upstream decay and a beam positron within 200 ns.

15. Downstream Decay (US part of beam e+ removed)
    Appears to be a downstream decay and a beam positron within 200 ns.

16. Soft uncorrelated track
    All u,v hits at one position with RMS less than 0.5 cm, that does not have one end near a muon stop (more than 2 planes, or more than 5 cm in u,v).

17. Cosmic, noise, or beam gas
    Appears to be just a cosmic ray, noise, or beam gas. Not enough planes hit or too far from any muon stops to be a muon or decay positron.

18. Too early
    Track has only DC hits with earliest time less than -5800 ns, or PC hits earlier than -5800 ns.

19. Too late
    Earliest window hit time is later than 9800 ns.

20. Don't know
    Decay positrons with no muon that can be seen in the event. They could also be some leakage from other window types that for whatever reason had average hit distributions that just did not seem right.

21. Pion
    No events should possess this window type since the default parameters are set such. These would be windows that appear to have a pion (large m12width, specific TCAP time, and stop before a particular DC plane).

The algorithm to determine the window types uses different decision processes if:

- the window is determined to be the trigger window (within 100 ns of zero time),
- the window is within 900 ns of any other window, or
- there has or has not been a muon found yet.

Review Window Types Looking at Whole Event

After looping through each window separately to decide on window types, a second pass is made to look for pathological cases, and correct the window types for these cases.

Assign Hits to Window

Using the already determined PC windows that have been tagged as being of a particular type, fill the time window structure with two windows for each PC window. For each PC window we put the hits that we think belong to the decay positron into the even window, and hits that do not belong to the muon or beam positron into the previous odd window.

3.3.6 Decide on Overall Event Type

The decision about the overall event type is simple because information about what each window contains has already been determined. The *event types* are enumerated below, and the probabilities for each event type in 2004 data and simulation are shown in Figure 3.2. Event type 14, the beam positron triggers, occur more frequently in data since the simulation should not have any beam positron triggers. Event types 26 and 27 are "dirty" event types that appear more frequently in data than in the simulation.

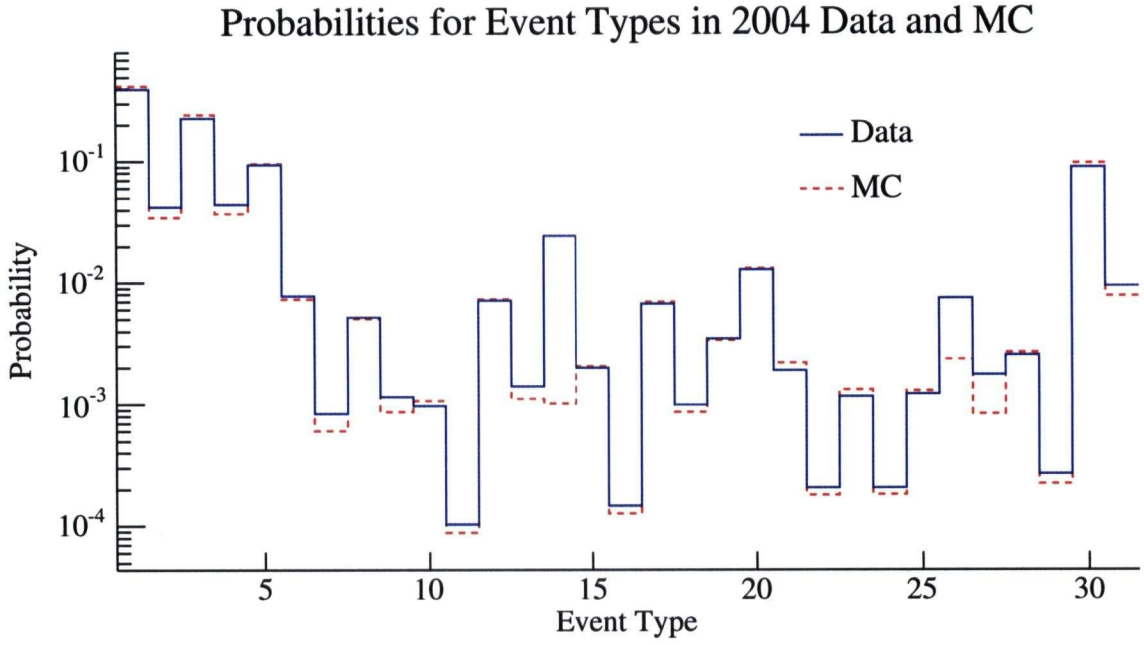

Figure 3.2: Distribution of event types in 2004 data and simulation. Event type 14 is the beam positron trigger events that should only occur in the data. The beam positron trigger classifications of the simulation occur for beam positrons that come close in time to a muon.

1. Simple clean
   Muon and decay positron, separated in time by more than 1050 ns. No other windows in the event.

2. Time clean
   Muon, decay, and beam positron(s) each separated in time by more than 1050 ns.

3. Simple DC overlap
   Muon and decay positron separated in time by 200 ns, but less than 1050 ns apart. No other windows are in the event.

4. Time DC overlap
   Muon, decay positron and beam positron(s) each separated in time by 200 ns or more, but at least one time between windows is less than 1050 ns.

5. PC overlap
   There is at least one window which has two tracks within 200ns of each other.

6. Simple delta cleaned
   Muon and decay positron, separated in time by more than 1050 ns. The decay positron has a delta which extends to the other side of the muon stop. No other windows in the event.

7. Time delta cleaned
   Muon, decay positron and beam positron(s), each separated in time by more than 1050 ns. The decay positron has a delta which extends to the other side of the muon stop.

8. Simple DC overlap delta cleaned
   Muon and decay positron, separated in time by more than 200 ns but less than 1050 ns. The decay positron has a delta which extends to the other side of the muon stop. No other windows in the event.

9. Time DC overlap delta cleaned
   Muon, decay positron and beam positron(s), each separated in time by more than 200 ns but at least one is separated in time by less than 1050 ns. The decay positron has a delta which extends to the other side of the muon stop.

10. Simple scatter cleaned
    Muon and decay positron, separated in time by more than 1050 ns. The decay positron has lots of hits per plane and has hits on both sides of the muon stop. No other windows are in the event.

11. Time scatter cleaned
    Muon, decay positron and beam positron(s), each separated in time by more than 1050 ns. The decay positron has lots of hits per plane and has hits on both sides of the muon stop.

12. Simple DC overlap scatter cleaned
    Muon and decay positron, separated in time by more than 200 ns but less than 1050 ns. The decay positron has lots of hits per plane and hits on both sides of the muon stop. No other windows are in the event.

13. Time DC overlap scatter cleaned
    Muon, decay positron and beam positron(s), each separated in time by more than 200 ns but at least one is separated in time by less than 1050 ns. The decay positron has lots of hits per plane and hits on both sides of the muon stop. No other windows are in the event.

14. Beam positron trigger
    Event appears to have been triggered by a beam positron. There can be any combination of other window types in the event.

15. Multiple muon decays simple clean
    Two or more muons are in the event. All of the windows are separated in time by more than 1050 ns. Only muons and decay positrons are in the event, and the order of the windows is: muon, decay, muon, ...

16. Multiple muon decays time clean
    Two or more muons are in the event. All of the windows are separated by more than 1050 ns. Only muons, decay positrons, and beam positrons are in the event. The order of the muons and decay positron(s) is: muon, decay, muon ... The beam positron window(s) can come in any order.

17. Multiple muon decays DC overlap simple clean
    Two or more muons are in the event. All windows are separated by more than 200 ns, and at least one pair of windows is separated in time by less than 1050 ns. Only muons and decay positrons are in the event, and the order of the windows is: muon, decay, muon, ...

18. Multiple muon decays DC overlap time clean
    Two or more muons are in the event. All windows are separated by more than 200 ns, and at least one pair of windows is separated in time by less than 1050 ns. Only muons, decay positrons, and beam positrons are in the event. The order of the muons and decay positron(s) is: muon, decay, muon, ... The beam positron window(s) can be in any order.

19. Multiple muon decays dirty
    Two or more muon decays that are in the wrong order, or at least one pair of windows that are within 200 ns.

20. Muon(s) and beam positron(s)
    There is one or more muons in the event and zero or more beam positrons. There does not appear to be any decay positron.

21. Simple beam positron cleaned
    Muon and decay positron tracks separated in time by more than 1050 ns. The decay positron appears to be within 200 ns of a beam positron. No other windows are in the event.

22. Time beam positron cleaned
    A muon, decay positron, and beam positron(s) separated in time by more than 1050 ns. The decay positron appears to be within 200 ns of a beam positron.

23. Simple DC overlap beam positron cleaned
    A muon and decay positron separated in time by more than 200 ns but less than 1050 ns. The decay positron appears to be within 200 ns of a beam positron or backscatter. No other windows are in the event.

24. Time DC overlap beam positron cleaned
    A muon, decay positron, and beam positron(s) separated in time by more than 200 ns, where at least one pair of the windows is separated by less than 1050 ns. The decay positron appears to be within 200 ns of a beam positron.

25. Beam positrons, unknown trigger
    Events where the trigger window does not contain either a muon or a beam positron, and the event does not contain any muon(s) or decay positron(s).

26. Other unknown trigger
    Events where the trigger window does not contain either a muon or a beam positron. There can by any combination of other window types in the event.

27. Other
    Whatever is left.

28. Simple clean – too few planes hit for event types 1, 6, 10, and 15
    Simple clean muon and decay positron events with fewer than 6 planes hit so that no reasonable fit could be done.

29. Time clean – too few planes hit for event types 2, 7, 11, and 16
    Time clean events with fewer than 6 planes hit for the decay positron so that no reasonable fit could be done.

30. Simple clean – Too high angle for event types 1, 6, 10, and 15
    Simple clean events, where the decay positron has an average cluster area greater than 12.5, and average hits per plane more than 3.5.

31. Time clean – Too high angle for event types 2, 7, 11 , and 16
    Time clean events, where the decay positron has an average cluster area greater than 12.5, and average hits per plane more than 3.5.

3.4 Clustering

Hits on adjacent wires are grouped together and called a cluster. Adjacent orthogonal planes can also be combined to make two dimensional clusters.

The number of wires hit on average is a function of crossing position, angle and energy of the particle that passes through the chamber. The angle of a positron track relative to the z axis (θ), is correlated with the average number of wires hit per chamber. For this reason the average cluster size is used to classify very large angle decay positrons into their own event types. Hit clustering is illustrated in Fig. 3.3, including the ambiguity resulting from multiple particles overlapping in time.

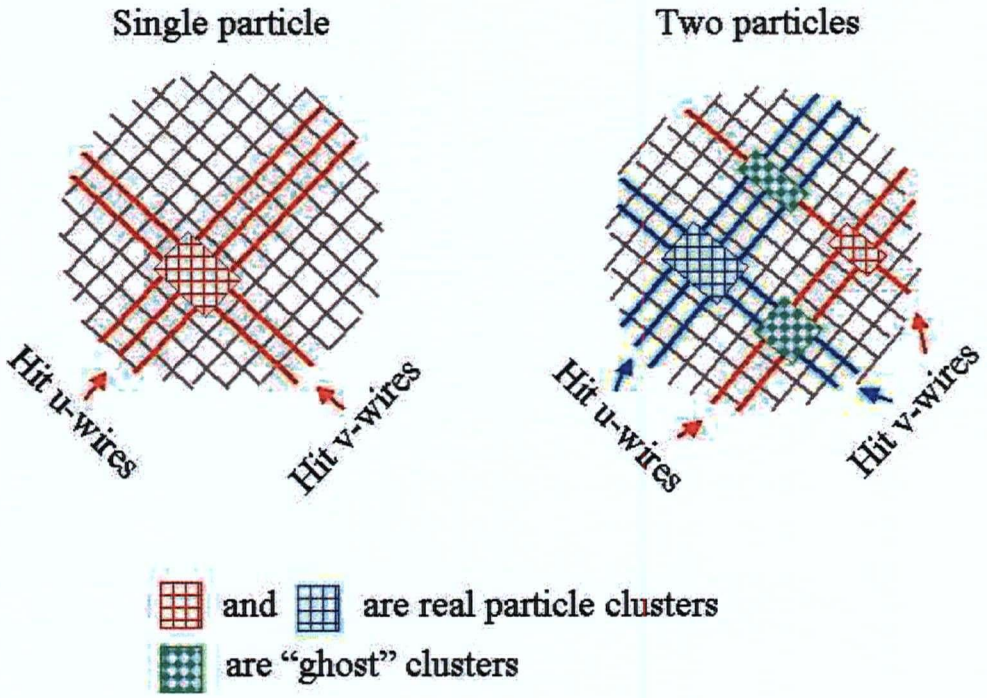

Figure 3.3: A simple single particle cluster of u and v wire hits is shown on the left. On the right we see that when there are two particles there is an ambiguity as to which clusters are real. Removing these fake clusters, called "ghost" clusters, is done by a first pass at a wire centers fit to a helix.

3.5 Track Fitting

This section describes the initial track estimate, the track fitting, and the final track fitting resolution and efficiency.

3.5.1 Initial Estimate

The initial helix estimate is done in two steps. The first step estimates the radius and center of the circle from the projection of the helix onto the transverse plane. The second step is to determine the phase and winding number of the helix.

The circle estimate is obtained for every combination of three hit clusters. The χ^2 is calculated for each of the three hit circle estimates. The circle estimate yielding the smallest χ^2 is selected as the initial circle.

The phase of a helix can be expressed in terms of an initial phase ϕ_0 at z_0 as:

$$\phi_i = \omega(z_i - z_0) + \phi_0. \tag{3.2}$$

ϕ at the z location of a foil between two adjacent orthogonal planes can be estimated by calculating the angle between the u axis and a ray from the center of the circle, (u_c, v_c), through u and v as measured at the two planes.

$$\phi_i^{\text{calc}} = \tan^{-1}\left(\frac{v_i - v_c}{u_i - u_c}\right). \tag{3.3}$$

The phase as a function of z mod 2π is equivalent to the calculated phase.

$$\phi_i = \phi_i^{\text{calc}} + 2\pi n_i \qquad n_i \in \mathbf{I}. \tag{3.4}$$

There are an infinite number of possible combinations of winding number, n_i. There are two key physical restrictions that can be made to limit the combinations to a reasonable number. First, the longitudinal frequency, ω, of the track is correlated with the number of cells hit within a plane. Second, reconstructable tracks do not wind through a phase change of 2π between successive pairs in the dense stack. Those that wind more than 2π in the dense stack are well outside the angular acceptance of the detector.

To obtain the best estimate of the phase and winding number, we use a combinatorial approach beginning with the most likely candidate. We fix $\phi_i = \phi_i^{\text{calc}}$ at one z_i, and fix a second $\phi_k = \phi_k^{\text{calc}} + 2\pi n_i$ at a z_k far from the first one. The phases of the remaining hits (j) are chosen by minimizing:

$$\left|\phi_i - \left[\frac{\phi_k - \phi_j}{z_k - z_j}\right](z_i - z_j) - \phi_j\right|. \tag{3.5}$$

Given $z_0 = (z_j + z_k)/2$, the resulting ϕ_j versus z is fit to a straight line to deduce ω and ϕ_0. The steps are repeated, replacing n_i with the values $-n_k$, $n_k + 1$, $n_k - 1$, $-n_k - 1$, $-n_k + 1$, ... , 50, -50, 1, -1, 0. All of the previous steps are repeated but two different starting z to fix

ϕ are selected. The process is continued until an acceptable estimate is found or all allowed values have been tried.

To estimate the fit acceptability a Chebyshev Norm is defined as $\sum \Delta\Phi_i$ where $\Delta\Phi_i$ is the difference between the angle as predicted by the track estimate, ϕ_i^{pred}, and the angle as calculated from the cluster of hit cells, ϕ_i^{calc}. The difference, $\Delta\Phi_i$, is set to zero if it is within a half of the cluster width of the fit. The selection criteria for an acceptable track is that its Chebyshev Norm is zero.

3.5.2 Helix Fitting

The final helix fit is seeded with the initial guess described in the previous subsection. The fit is done in two steps.

In the first step of helix fitting, a wire center fit using the narrow windows technique [49] is used. Some important features of the wire center fit is that it uses a magnetic field map, allows for kinks in the track, and can split the track into two tracks if there is a sufficiently large scatter. Kinks are included by applying a penalty to the fit χ^2 as described by Lutz[50]. The fit is done by minimizing the χ^2:

$$\chi^2 = \sum (d_{\text{track}} - d_{\text{hit}})^2/\sigma_d^2 + \sum \theta_{\text{kink}}^2/\sigma_{\text{kink}}^2, \tag{3.6}$$

where $d_{\text{track}} = f(\text{fit parameters}, z)$ integrates $\vec{F} = q\vec{v} \times \vec{B}$ using an arc step approximation with variable step size. Iteration of the track fitting is done to resolve most left-right ambiguities.

The final track fit is done using the DC drift time information. The drift time to distance relationship is estimated by Garfield[45]. The efficiency of the track fitting is better than 99% withing the nominal fiducial region used for spectrum fitting. The fit efficiency versus momentum and angle is shown in Figure 3.4. Future improvements are: to determine the drift time to distance relationships from the data, and to weight the hits using a distance and angle dependent resolution. The helix fits performed for this analysis assumed a constant 100 μm resolution.

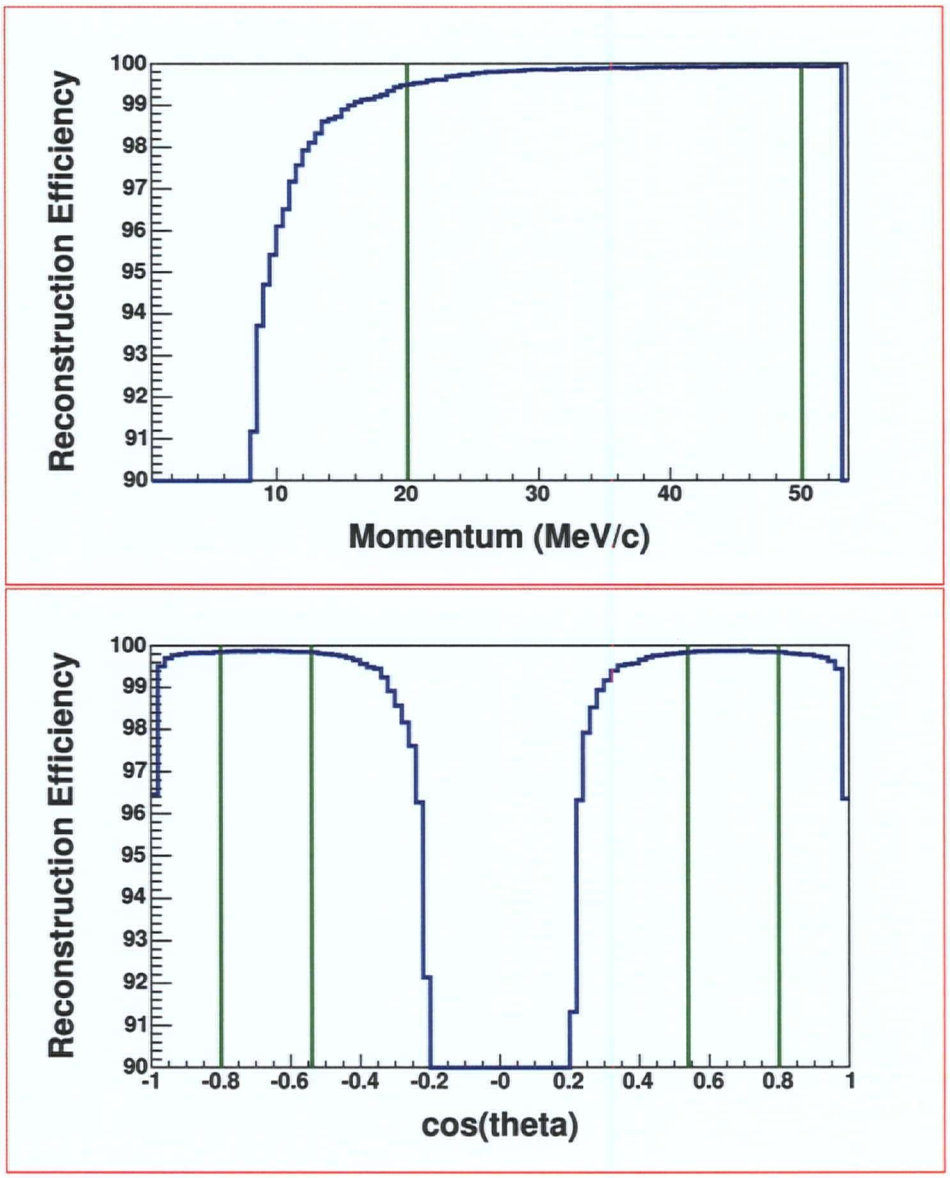

Figure 3.4: The helix fit efficiency versus momentum is shown at the top, and the fit efficiency versus $\cos\theta$ is shown on the bottom. The green lines mark the fiducial region.

3.6 Energy Calibration

3.6.1 Endpoint Energy Calibration Method

This section describes the energy calibration, including the calibration at momenta other than at the decay positron endpoint momentum (p_{edge}). The corrected momentum p_{ec} is given by:

$$p_{\text{ec}} = \frac{p_{\text{rec}}}{1 + \frac{\beta}{p_{\text{edge}}}} + \frac{\alpha}{|\cos\theta|}, \tag{3.7}$$

where p_{rec} is the reconstructed momentum, $\cos\theta$ is the reconstructed cosine of the decay positron angle, β is the shift in the spectrum from the theoretical endpoint momentum, and $\alpha = (\alpha_u, \alpha_d)$ is the zero angle energy loss for upstream (u) or downstream (d) decay positron tracks. This simple form is valid to first order because of the planar geometry of the wire chambers.

A procedure for determining the spectrum edge energy calibration parameters was developed by Andrei Gaponenko. The endpoint fit function is a slope with an edge convoluted with a Gaussian as illustrated in Figure 3.5. An angle dependent resolution is put into the fitting function. The end point of the muon decay spectrum, and sections of the 2-dimensional end point fit function for several angular slices are shown in Figure 3.6.

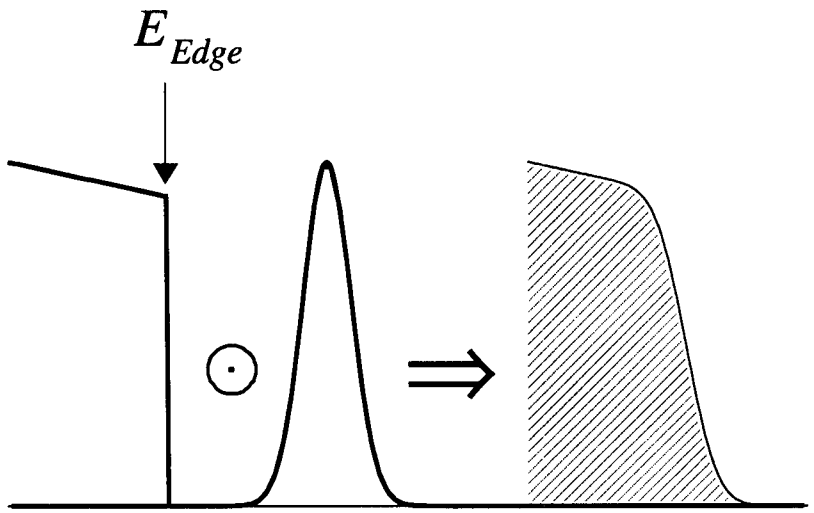

Figure 3.5: A convolution of the cut-off linear function with a Gaussian gives the shape on the right, which is used to fit the end point of the reconstructed spectrum.

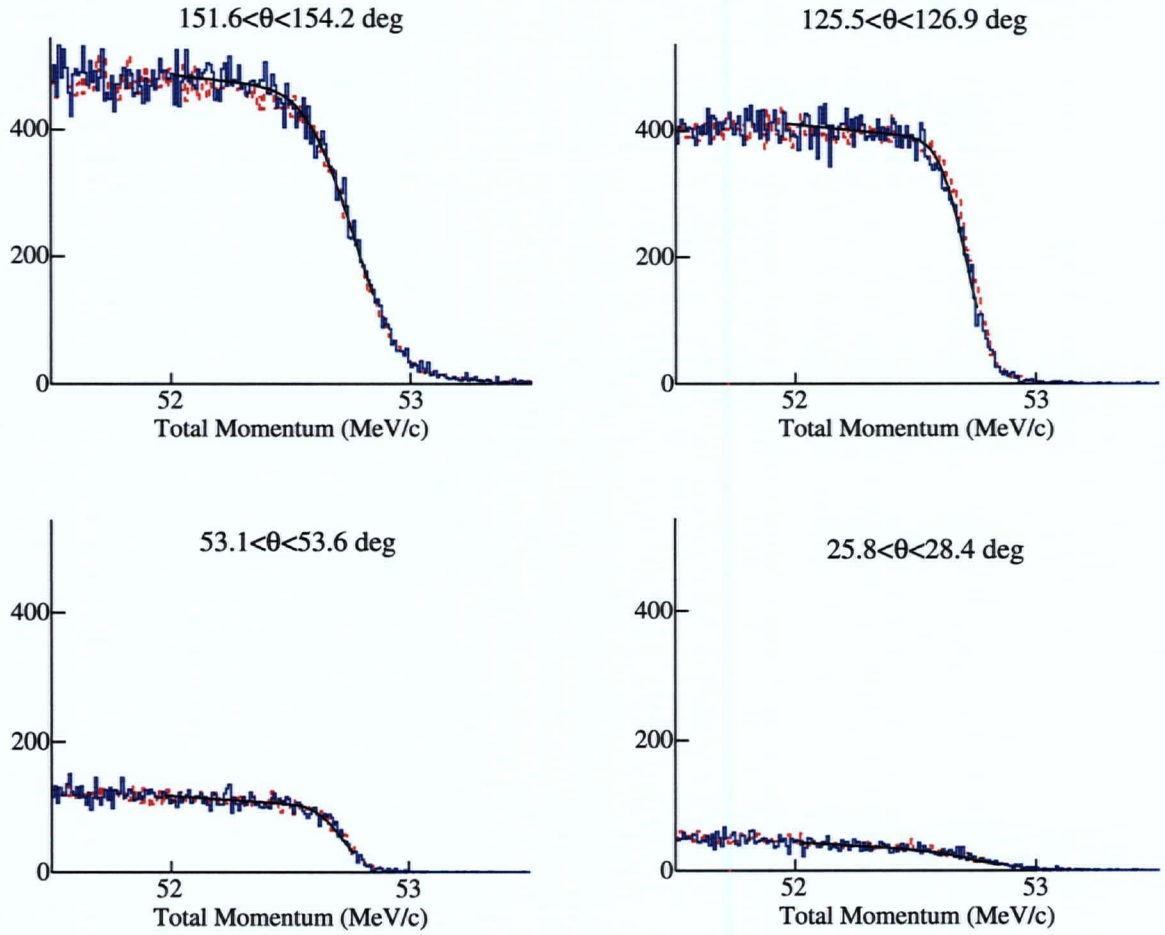

Figure 3.6: The end point of the muon decay spectrum, and sections of the 2-dimensional end point fit function for several angular slices. Data set 35 is shown in blue, and the matching simulation set is shown underneath in red. The smallest and the largest angles in the upstream (top), and the downstream (bottom) are shown.

3.6.2 Endpoint Energy Calibration Results

The energy calibration results for the data used for the measurement of $P_\mu \xi$ are presented in this section. For a description of the data sets refer to Chapter 4, and for a description of the simulation refer to Chapter 5.

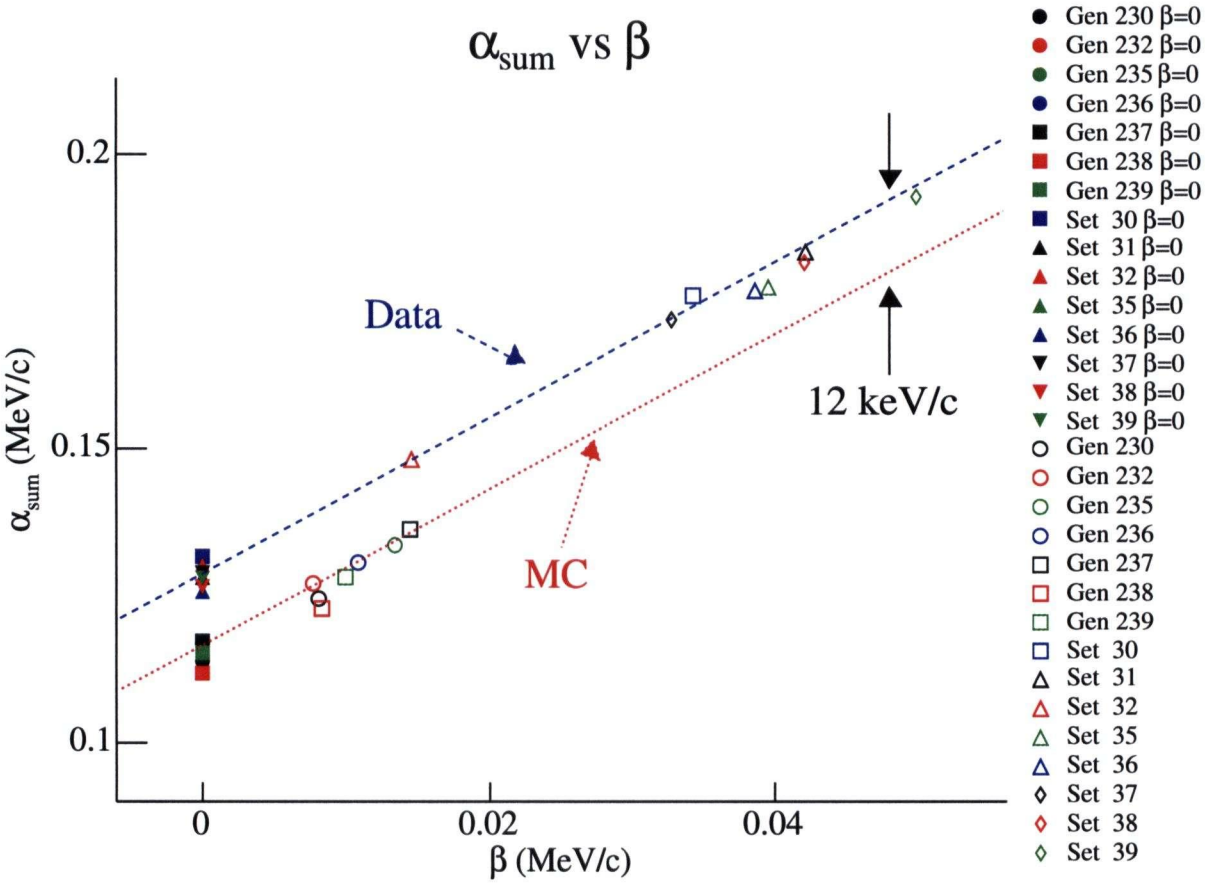

Figure 3.7: Energy calibration α_{sum} versus β in 2004 data and simulation.

The endpoint fit parameter β is highly correlated with $\alpha_{\text{sum}} = \alpha_u + \alpha_d$. This correlation is very clear in a plot of α_{sum} versus β as shown in Figure 3.6.2. We expect the momentum measured with our fits to be unbiased since: we know in simulation that we measure the momentum without bias at the few keV/c level, we measure our magnetic field with an NMR, and have a field map that is good to better than 2 G in the tracking region. For this reason we use an endpoint fit where we fix the value of β to zero. Table 3.6.2 presents the endpoint fit results for each of the data and simulation sets used for the measurement of $P_\mu \xi$.

The difference between the upstream and downstream energy loss is not correlated with the endpoint, but is sensitive to the muon stopping location. For example data sets with the muon distribution stopped 3/4 of the way into the muon stopping target have slightly more

Spectrum	β	α_u	α_d	σ_0	$\alpha_u(\beta=0)$	$\alpha_d(\beta=0)$
Gen 230	8.0±3.3	61.3±2.3	63.2±2.2	67.7±0.6	55.8±0.4	58.0±0.4
Gen 232	7.6±5.7	56.3±4.0	70.7±4.0	66.8±1.1	51.1±0.7	65.7±0.7
Gen 235	13.3±3.2	65.4±2.2	68.2±2.2	67.5±0.6	56.2±0.4	59.6±0.4
Gen 236	10.8±3.4	67.6±2.4	63.1±2.3	68.4±0.7	60.2±0.4	56.3±0.5
Gen 237	14.4±5.1	69.2±3.5	67.0±3.5	67.9±1.0	59.4±0.6	57.8±0.7
Gen 238	8.3±4.9	64.2±3.4	58.6±3.4	64.9±0.9	58.5±0.6	53.2±0.6
Gen 239	9.9±3.4	67.0±2.4	61.2±2.3	68.1±0.7	60.3±0.5	54.9±0.5
Set 30	34.3±11.9	89.4±8.2	86.7±8.2	71.3±2.4	65.9±1.6	65.7±1.7
Set 31	42.2±5.9	92.6±4.1	90.7±4.0	71.2±1.2	63.9±0.8	64.1±0.8
Set 32	14.5±10.6	68.1±7.4	79.9±7.3	70.5±2.1	58.2±1.4	72.0±1.4
Set 35	39.6±4.9	91.3±3.4	86.2±3.4	71.5±1.0	64.4±0.6	61.3±0.7
Set 36	38.6±4.7	93.7±3.3	83.2±3.2	68.9±0.9	67.2±0.6	58.5±0.7
Set 37	32.8±6.3	90.6±4.4	81.4±4.3	74.2±1.3	68.3±0.9	60.5±0.9
Set 38	42.1±5.4	95.6±3.7	86.0±3.7	71.1±1.1	67.0±0.7	59.5±0.8
Set 39	49.8±6.9	101.2±4.8	91.7±4.7	71.6±1.4	67.4±0.9	60.6±1.0

Table 3.1: Energy calibration results for 2004 data and simulation in keV/c. The last two columns give the results for fits with the endpoint shift β fixed to zero.

positive $\alpha_u - \alpha_d$. The data set where we stopped the muons upstream, set 32, has a much more negative $\alpha_u - \alpha_d$ than the other datasets.

A difference between simulation and data is evident in the resolution, σ_0, measured at the endpoint. This difference is attributed to imperfections in the real detector that are not included in the simulation. Possible differences are in wire-to-wire timing, or in the chamber STRs. The 12 keV/c difference between the data and simulation α_{sum} values is corrected for by applying the energy calibration. The systematic uncertainty in $P_\mu \xi$ due to energy calibration is estimated in Section 6.3.1.

3.6.3 Momentum Dependent Energy Calibration

Studies of positron tracks that traverse the detector can be used to look at momenta that differ from the endpoint momentum. The plots used are of the difference between the upstream and downstream reconstructed momenta times $\cos\theta$ versus the momentum ($\overline{\Delta p \cos\theta}$ versus p). These plots show a clear linear dependence, and if there is no shift in the endpoint ($\beta = 0$), then:

$$\overline{\Delta p \cos\theta} = \alpha_0 + \alpha_1 p = \alpha_{\text{tot}}(p). \tag{3.8}$$

If $\beta = 0$ then $\alpha_{\text{tot}}(p_{\text{rec}})$ is related by a constant scaling to our endpoint momentum calibration $\alpha_{\text{sum}} = \alpha_u + \alpha_d$ at the endpoint. We obtain momentum dependent $\alpha_u(p)$ and $\alpha_d(p)$:

$$\alpha_u(p) = \frac{\alpha_u(p_{\text{edge}})}{\alpha_{\text{tot}}(p_{\text{edge}})}(\alpha_0 + \alpha_1 p), \text{ and} \tag{3.9}$$

$$\alpha_d(p) = \frac{\alpha_d(p_{\text{edge}})}{\alpha_{\text{tot}}(p_{\text{edge}})}(\alpha_0 + \alpha_1 p). \tag{3.10}$$

If we use this formulation, then the energy correction on the reconstructed momentum will look like the following equation:

$$p_{\text{ec}} = \frac{p_{\text{rec}}}{1 + \frac{\beta}{p_{\text{edge}}}} + \frac{\frac{\alpha}{\alpha_{\text{tot}}(p_{\text{edge}})}(\alpha_0 + \alpha_1 p_{\text{rec}})}{|\cos\theta|}, \tag{3.11}$$

or equivalently,

$$p_{\text{ec}} = \frac{p_{\text{rec}}}{1 + \frac{\beta}{p_{\text{edge}}}} + \frac{\alpha}{|\cos\theta|}\frac{(\alpha_0 + \alpha_1 p_{\text{rec}})}{(\alpha_0 + \alpha_1 p_{\text{edge}})}. \tag{3.12}$$

To obtain the energy calibration constants, α and β, fits to the decay positron spectrum edge are performed. The α_0 and α_1 parameters are determined from an analysis of far upstream stops data. The α_1 correction was not applied, but a systematic uncertainty due to the discrepancies between the simulation and the data values of α_1 are estimated in Section 6.4.1.

3.7 Track Selection and Cuts

This section describes the tree processing code, and the final fiducial cut implemented in the spectrum fitting program. The tree processing code, described in the following subsection, does the final track selection and event type cuts. Fiducial cuts on the decay positron momentum and angle are done at the spectrum fitting stage.

3.7.1 Tree Processing Code Description

The tree processing code cuts, and track selection algorithm are described in this section. The cuts that the tree processing code performs are:

1. TCAP
   A time of flight from the proton beam capacitive probe to the trigger scintillator is used to cut beam positrons, cloud muons, and pions. The elimination of the differently polarized cloud muons is clearly seen by looking at an asymmetry analysis of the polarization versus TCAP shown if Fig. 3.8.

2. Event type
   An event type cut is made to select clean muon and decay events, including events that have hard scatters or delta electrons. This cut removes multiple muons, very high angle decay positrons, and non muon events.

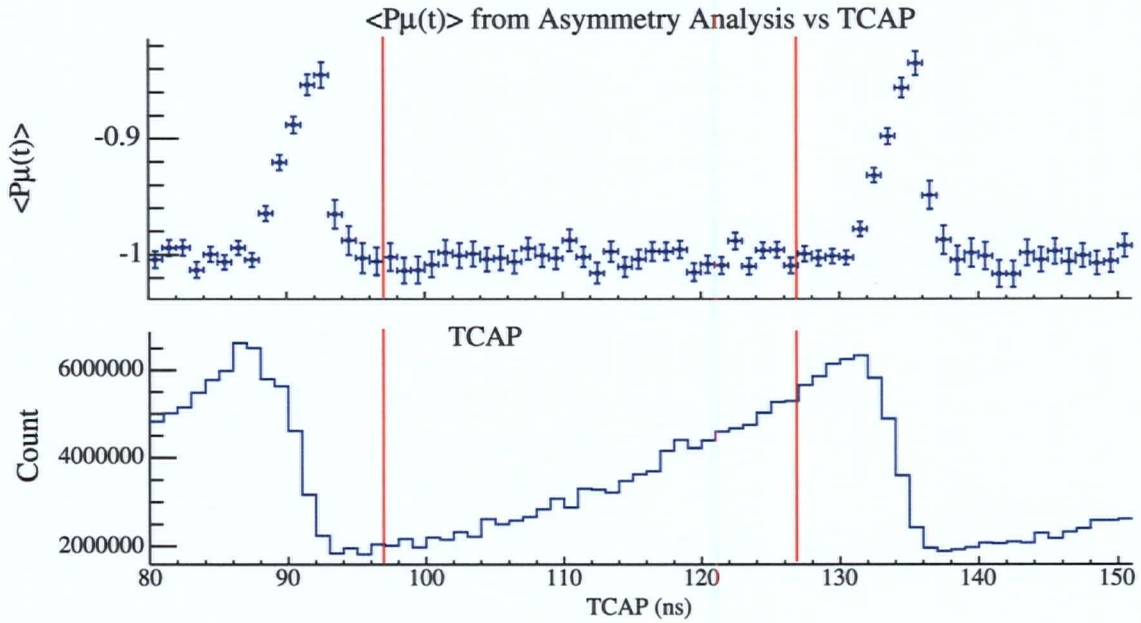

Figure 3.8: The time averaged $P_\mu(t)$ from an asymmetry analysis versus TCAP is shown on top, and the number of events versus TCAP is shown on the bottom. The red lines indicate where the cut was placed in this analysis. Some statistics could have been gained by moving the higher end of the cut from 127 ns to 129 ns.

3. Muon stop
   The muon stop cut removes muons that have their last hit somewhere other than immediately before the muon stopping target. This cut also removes any remaining multiple muon events.

4. Muon stop radius
   Removes muons that stop too far from the center of the detector, in u, v, at the last two planes hit by the muon. The cut is on $\sqrt{u^2 + v^2}$.

5. Decay time cut
   The decay time cut removes events that are too late, and may have lost too many late DC hits. This cut removes decays that are before 1050 ns, that might have late muon hits confusing the decay positron track. The decay time used is the window time, which is derived from the earliest PC hit.

6. Number of decay positron tracks
   Require at least one fit to a decay positron.

7. Fit error cut
   Removes tracks that have bad helix fits.

8. Track start stop
   Removes track fits that start, stop or have a $\cos\theta$ that do not match its decay direction.

9. Track charge
   Tracks should have positive charge, tracks with negative charge or undetermined charge are cut.

10. Cut pair matches
    Tracks that have a match in the closest distance of approach (CDA) and in time with another track are rejected. These are most likely beam positron contamination, or backscattered tracks. If all of the tracks are thrown out, the event is rejected.

The final track selected is the one that has an end point closest to the muon stopping target, and closet to the muon (u, v) coordinate. The distributions of the different cut probabilities in simulation and data are shown in Figure 3.9. Distributions of the cut variables both before and after each cut in the data are illustrated in Figure 3.10. The largest discrepancy between simulation and data is in the muon radius cut, and is due to the larger muon beam size at the target in simulation. A systematic uncertainty due to this discrepancy is estimated in Section 6.1.3. Studies of variations in the tree sum cut values show that the biggest change in $P_\mu \xi$ is related to the track pair matching cut, and is smaller than 0.0002.

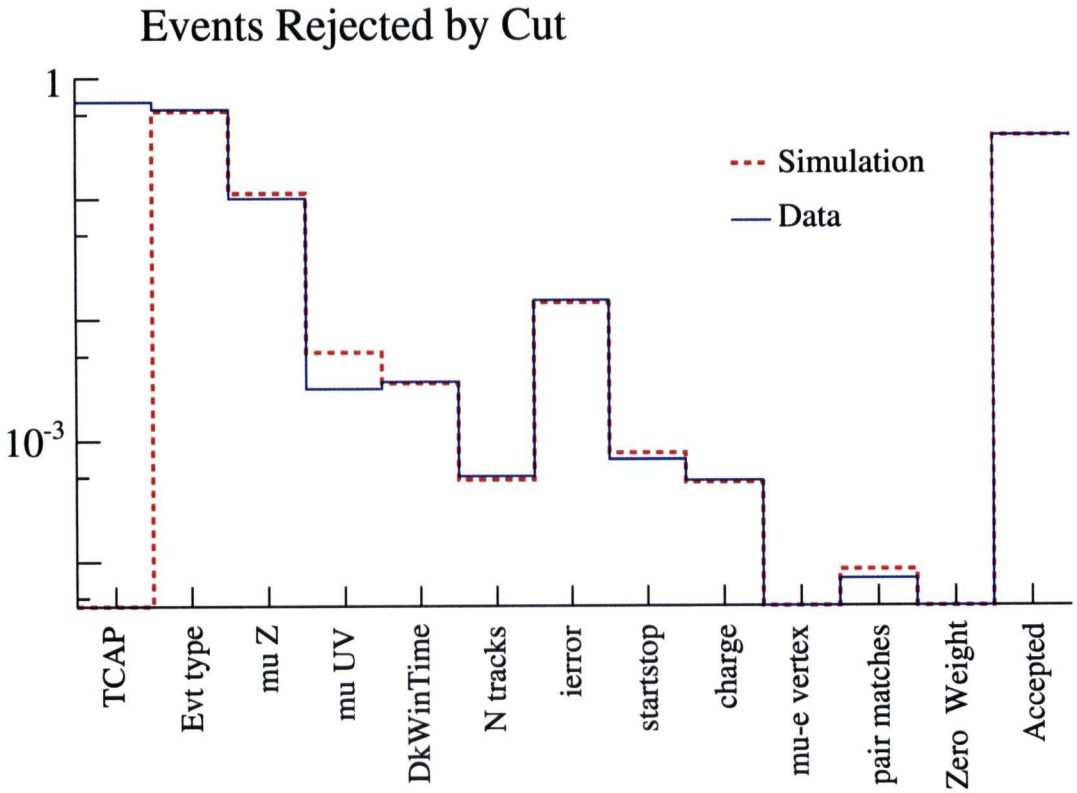

Figure 3.9: Event and track selection cut probabilities in simulation and data. The largest discrepancy between simulation and data is in the muon radius cut, and is due to the larger muon beam size at the target in simulation. The TCAP cut is only applied to data since the simulation does not include pions, beam positron triggers or cloud muons.

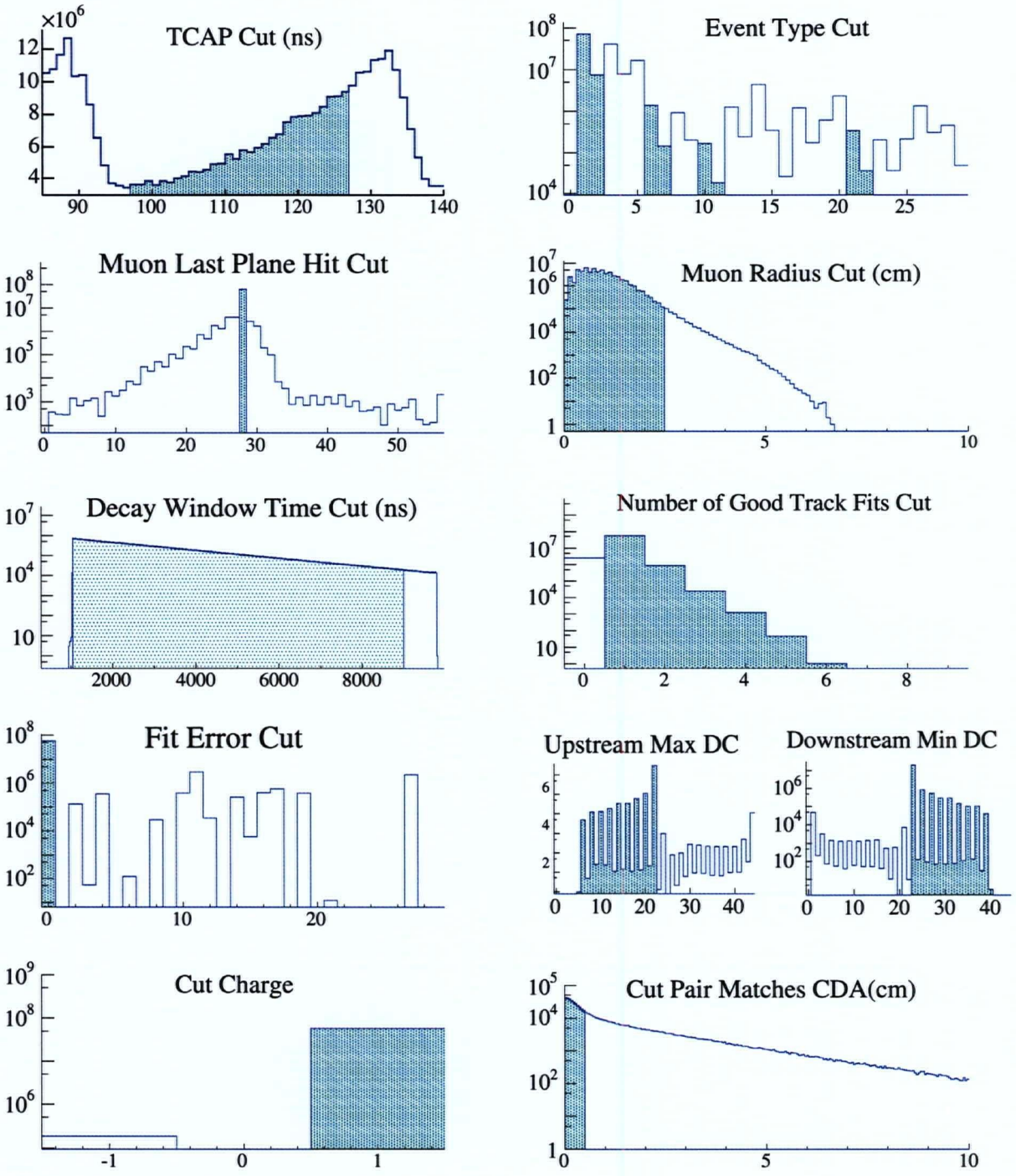

Figure 3.10: Event and track selection cut distributions for the data. The number of events before the cut is shown as the dark blue lines, and the events or tracks selected are shown as the shaded cyan regions. A description of the cuts is in text.

3.7.2 Fiducial Cuts

The fiducial cuts are implemented in the spectrum fitting code. The list below itemizes the cuts.

1. $p_l > 13.7$ MeV/c
   The positron longitudinal momentum cut is used to eliminate problems with detector granularity that arise due to the periodic spacing (4 cm and 6 cm) of the wire chambers.

2. $p_\perp < 38.6$ MeV/c
   The positron transverse momentum cut is used to eliminate decay positrons that could have gone outside of the wire plane measurement radius.

3. $p_{total} < 50.0$ MeV/c
   The positron total momentum cut is used to eliminate decay positrons near the end-point, where we have used the data to estimate the energy calibration.

4. $|\cos\theta| > 0.5$
   The angle between the detector z-axis and decay positron direction needs to be small enough that it can be measured without too much scattering. At too high an angle determining the winding number becomes impossible.

5. $|\cos\theta| < 0.84$
   The small angle decay positron cut is used to eliminate positrons with a small radius where the helix fitting fails.

The fiducial cuts described above are illustrated in Figure 3.11.

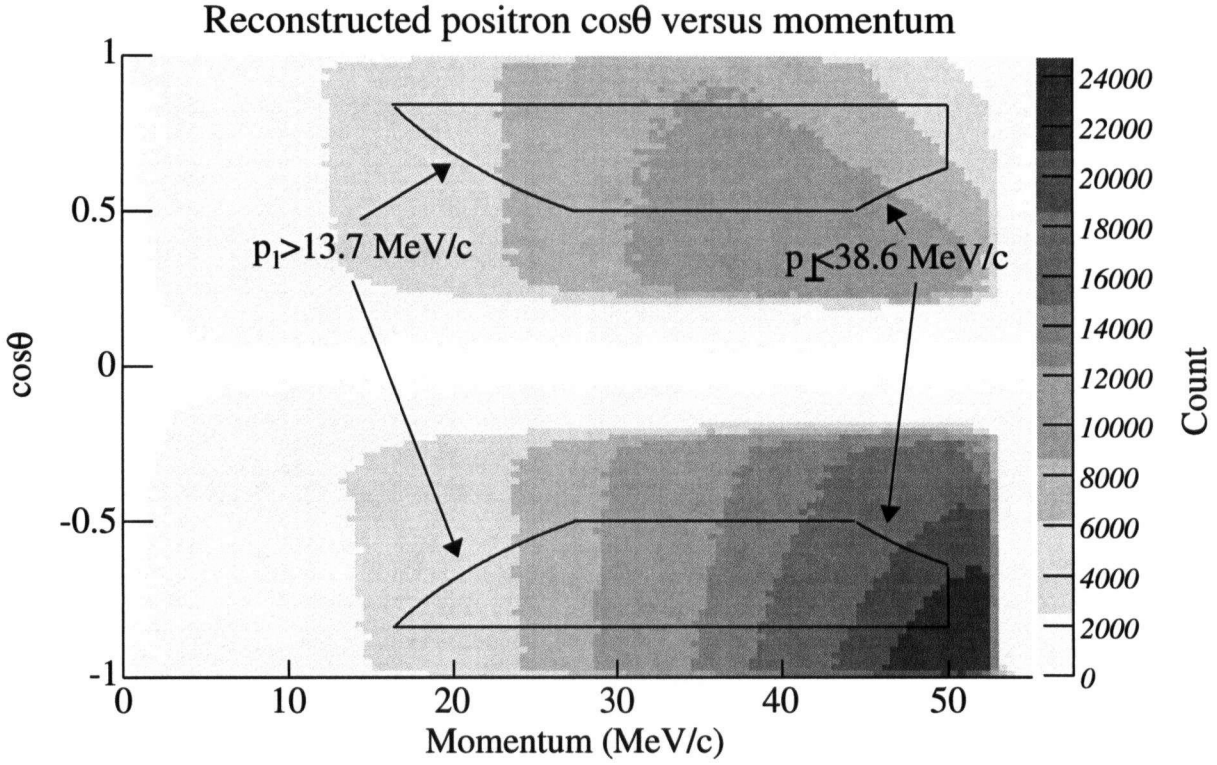

Figure 3.11: The distribution of positron angles and momenta. The fiducial region used for fitting the spectrum to simulation is inside the black lines. The longer curved black lines are the $p_l > 13.7$ MeV/c cuts, and the shorter curved black lines are the $p_\perp < 38.6$ MeV/c cuts.

Chapter 4

Data

This chapter describes the data used in this measurement of the muon decay parameters. The nominal and systematic data sets used, and the quality checks on the data are reviewed.

The data used in this thesis was collected over the period from October 15, 2004 to December 8, 2004. The period from October 15 to October 29 was spent with the solenoid at 0 T to study the muon beam, obtain time calibration, and plane alignment data. From October 29 to November 17 all of the nominal data with the solenoid at 2.0 T was obtained. On November 17 there was a disasterous accident that rendered 2/3 of the drift chambers inoperable. The remainder of the run period was used to study the muon beam and TEC operation both with the field on and off.

4.1 Data Sets

The data used for the measurement of $P_\mu\xi$ were taken in the fall of 2004 at TRIUMF using the M13 beamline. Seven datasets totaling nearly 2000 runs of 2GB size each are used in the final measurement. Two datasets were used to measure the detector response. The various data sets taken in 2004 are enumerated in Table 4.1.

Set	Runs (2 GB)	Abbreviation	Description
30	60	B2+5G A	B2 = 949 G, z centered, M1 trigger
31	265	B2+5G B	B2 = 949 G, z centered, M trigger
32	120	PC5 stop	B2 = 949 G, PC5 stops
33	91	far us	Far upstream Stops
34	11	far ds	Far downstream stops
35	368	stop 1/2	2004 nominal stop centered
36	390	stop 3/4 A	2004 stop at 3/4
37	281	hi rate	high rate
38	303	aperture	aperture In
39	211	stop 3/4 B	2004 stop at 3/4
Total	2100 (4 TB)	1998 nominal runs	

Table 4.1: Data set number, number of runs, and description of dataset. Sets 33 and 34 were taken to measure the detector response and were therefore excluded from the measurement of $P_\mu\xi$.

Sets 30, 31, and 32 were taken with the beam steered off center by changing the last

Magnet	Current (DCT)	NMR	Slit/Jaw	Width	Position
B1	39.8 A	871.37 G	F0 Jaws	18.0 mm	
B2	43.8 A	944.00 G	F0 Slits	60.0 mm	0.0 mm
Q1	149.8 A		F1 Slits	10.0 mm	0.0 mm
Q2	57.4 A		F2 Jaws	20.0 mm	
Q3	113.3 A		F2 Slits	12.0 mm	-5.0 mm
Q4	89.5 A				
Q5	113.4 A				
Q6	52.1 A				
Q7	59.6 A				

Table 4.2: Beamline element settings used for the nominal M13 surface muon beam tune used for 2004 data. Magnet currents are read from a direct current transformer (DCT).

bending magnet (B2) field by +5 G from the nominal 944 G to 949 G. Both sets 30 and 31 had the muon stop Bragg peak centered in the stopping target, while set 32 was stopped relatively far upstream to produce a larger fraction of stops in PC5. Set 30 used only one photomultiplier tube (PMT) readout for the trigger, while set 31 used a coincidence of the two PMTs from the trigger scintillator.

Sets 33 and 34 were taken with the muons stopping either very far upstream, or very far downstream. The purpose of these runs was to measure the detector response. This was done by obtaining positrons going from one end of the chamber stack to the other. Set 33 had the muon beam momentum lowered, and extra degrader inserted to stop the muons in the trigger scintillator and first four PCs. Set 34 was taken at a higher momentum with as much degrader removed as possible to stop the muons in the last four PCs, and in a plastic disk placed at the downstream end of the detector.

Set 35 was a nominal surface muon run with the beam centered, and the muon Bragg peak centered in the stopping target. The nominal beam settings are shown in Table 4.2. Refer to Section 2.2 for a description of the beamline. Sets 36 and 39 were surface muon sets with the muon beam stopping with the Bragg peak 3/4 of the way through the stopping target. The muon stopping distribution was changed to look for any effects of depolarization of the muons that stop in the CF_4/isobutane gas that surrounds the Al stopping target. The muon degrader CO_2/He fraction was about 37%/63% for stopping centered runs, 28%/72% for stopping at 3/4 runs.

Set 37 was taken with the beamline horizontal slits at F0 widened to 24.0 ± 0.1 mm, and vertical jaw at F0 widened to 80.0 ± 0.1 mm. This increased the beam rate from about 3 kHz to about 5 kHz. Set 38 was taken with the same beamline settings as set 37, but a 1 cm diameter Al aperture was inserted at 177 cm upstream of the center of the detector to reduce the radial size of the beam. Inserting the aperture reduced the beam rate to 1.2 kHz.

4.2 2002, 2003 and 2005 Data

Data were taken in 2002 and 2003. Some of the lessons learned from these data, and reasons why they were not used for *TWIST*'s first measurement of $P_\mu\xi$ are presented in this section. The 2003 data were not used because of uncertainties in the beam profiles, and a systematic set to look at the production target depolarization was later found to give an immeasurably small effect.

The 2002 data was used for a precision measurement of the muon decay parameters ρ and δ. The 2002 data were not suitable for a precision measurement of $P_\mu\xi$ because of the large depolarization observed in the graphite-coated Mylar target that was used to stop the muons. A few of the 2002 datasets, where a particular effect was exaggerated, are compared to a nominal 2002 dataset to estimate the systematic uncertainties. The systematic uncertainties obtained from 2002 data are: beam intensity (high rate and low rate data sets), and material outside the detector (downstream Al plate added data set).

A difference of $(15 \pm 2) \times 10^{-3}$ in polarization was observed between 2002 datasets where the solenoid field was changed from 1.96 T to 2.04 T. Subsequent simulations were done to study the effects of the change in the fringe field region and changes in the beam between these changed solenoid field data sets. The final polarization predicted by the simulation with these changed fringe fields and changed beams did not explain this large difference in polarizations as measured in the data. There is, however, a large uncertainty in the beam profiles used for the 2002 data such that we cannot completely rule out this scenario.

A more likely model for this large change in polarization between the 2002 data for the different solenoid field data sets is that different fractions of the muons were stopping in the Mylar versus in the graphite coating. Fitting all of the 2002 data to two different populations of muons, with different polarization rates, described the 2002 data much better than a single exponential depolarization rate. This model attributes the measured rates to muons stopping in Mylar ($\lambda_2 = -9.3 \times 10^{-6}$ /ns) and muons stopping in graphite ($\lambda_1 = -0.00044$ /ns). The target has less graphite than Mylar, so the faster depolarization rate is attributed to the graphite, since the polarization at a few μs was 90%, not 10%. Subsequent fits to the individual 1.96 T data set and the 2.04 T data set with the two depolarization rates fixed to the values measured in the fit to all 2002 data were done. The fits resulted in the polarizations extrapolated back to zero time agreeing, because of a difference in the fraction of muons depolarizing with the two different rates. Figure 4.1 shows an overlay of the asymmetry analysis $P_\mu(t)$ fit to double exponentials for the changed solenoid field data sets. The model used in the fit is:

$$P\mu(t) = P\mu_1(0)e^{-\lambda_1 t} + P\mu_2(0)e^{-\lambda_2 t} \tag{4.1}$$

where $P\mu_j(0)$ are really the product of the fraction of muons with the polarization of those muons at time zero. The fit results are summarized in Table 4.3.

If this model is correct, the 2004 data does not have this problem since it used an Al muon stopping target. If the explanation for the different solenoid field polarization values observed in 2002 is not due to this model then there is either large unexplained difference in polarization in the data or an undiscovered bug in the analysis. To verify that this systematic

Description	$P\mu_1(0)$	$P\mu_2(0)$	χ^2/NDOF
Sum	-0.069 ± 0.017	-0.877 ± 0.022	13.9/18
Set 1 (1.96 T)	-0.081 ± 0.007	-0.865 ± 0.003	27.7/20
Set 22 (2.04 T)	-0.059 ± 0.003	-0.888 ± 0.003	10.8/20

Table 4.3: Results of a double exponential fit to the sum of 2002 data, and the data sets with changed solenoid field.

uncertainty does not exist in the 2004 data, additional data were taken in 2005 at 1.96 T and 2.04 T; an analysis is presented in Section 4.3.

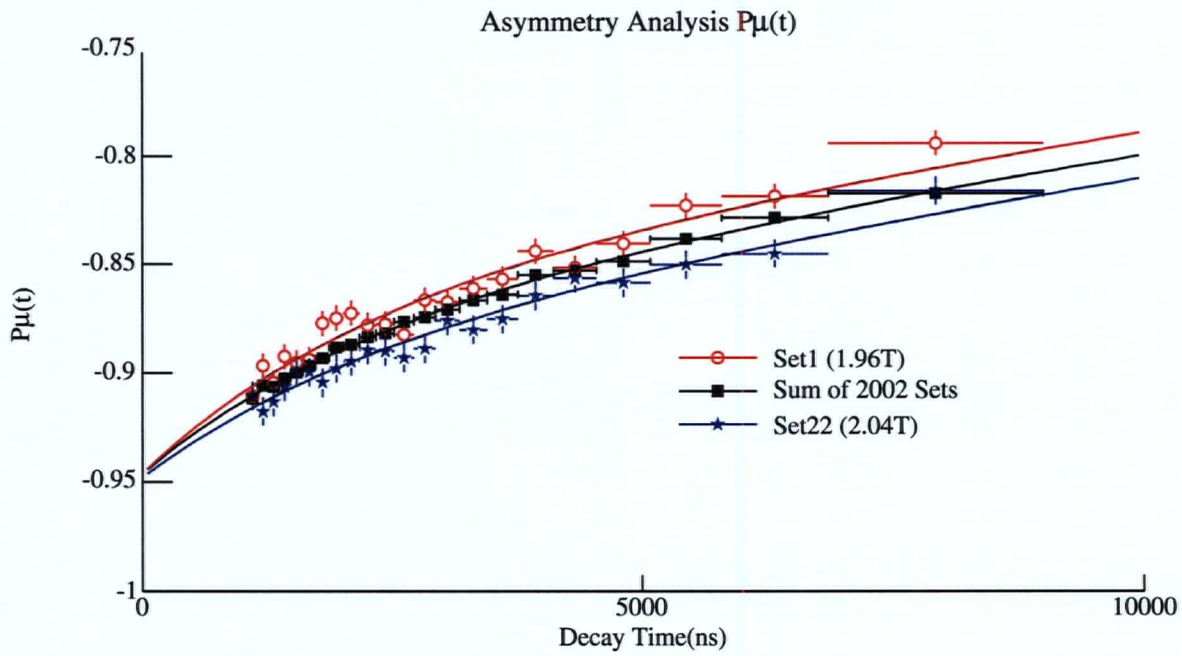

Figure 4.1: Overlay of the 2002 data muon polarization versus decay time from asymmetry analysis of the changed solenoid field data sets. The 1.96 T data and fit are shown as the upper red hollow circles, the 2.04 T data are shown as the lower blue stars, and the sum of all 2002 data used to determine the two decay rates are shown as the solid black squares.

4.3 Results of 2005 Data Solenoid Field Change

Three sets of data were taken in fall of 2005 were used to show that the solenoid field change was not a problem when using an Al muon stopping target. The three datasets were: 2.00 T, 1.96 T, and 2.04 T. The main result of the analysis is that there is no significant difference in the muon decay parameters, including $P_\mu\xi$, due to the change of solenoid field. The fit of the muon decay spectrum from the 2.04 T set to the decay spectrum from the 1.96 T set resulted in a difference in $P_\mu\xi$ of 0.0016 ± 0.0015. The spectrum fit results are tabulated in Table 4.4, and shown in Figure 4.2.

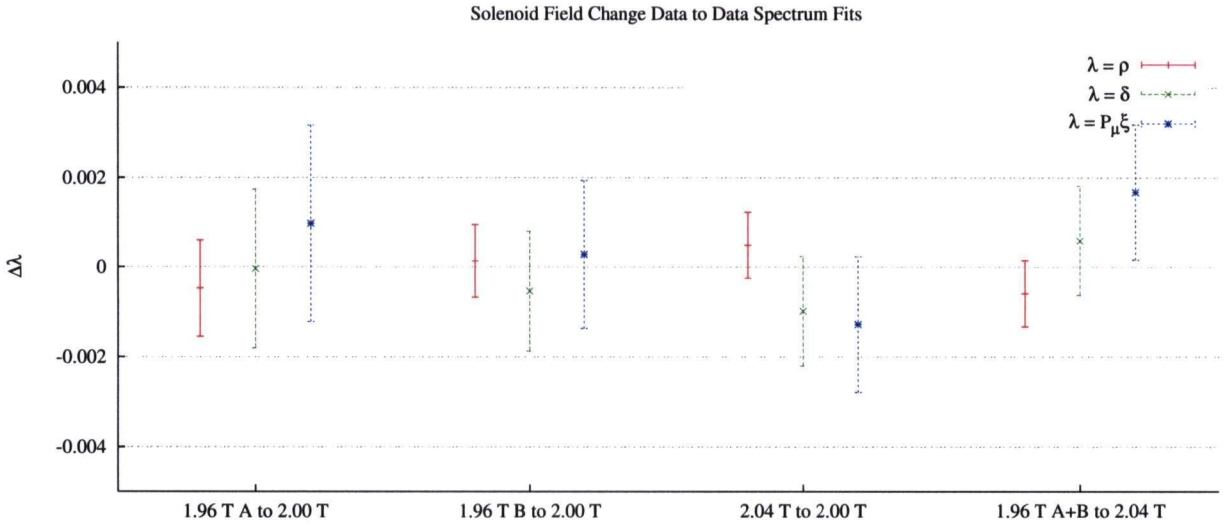

Figure 4.2: Differences in the muon decay parameters for data taken at different solenoid field settings. The differences in: ρ are shown as the red '+'s, δ are shown as the green 'x's, and $P_\mu\xi$ are shown as blue '*'s. The 1.96 T data were collected as two smaller sets, while the 2.00 T and 2.04 T were both single sets.

Data to data fit	$1000 \times \Delta\rho$	$1000 \times \Delta\delta$	$1000 \times \Delta P_\mu\xi$	$\chi^2/NDOF$
1.96 T A to 2.00 T	-0.5 ± 1.1	-0.0 ± 1.8	1.0 ± 2.2	1764/1887
1.96 T B to 2.00 T	0.1 ± 0.8	-0.5 ± 1.3	0.3 ± 1.7	1810/1887
2.04 T to 2.00 T	0.5 ± 0.7	-1.0 ± 1.2	-1.3 ± 1.5	1903/1887
1.96 T A+B to 2.04 T	-0.6 ± 0.7	0.6 ± 1.2	1.6 ± 1.5	1943/1887

Table 4.4: Results of 2005 data solenoid field change spectrum fits for the differences in the muon decay parameters.

Set	ATM (Torr)	B1NMR (gauss)	B2NMR (gauss)	M rate (Hz)	μ Stop z (cm)
30	749.2 (1.7)	871.298 (0.007)	949.001 (0.008)	2700 (50)	-0.810 (0.035)
31	758.7 (3.4)	871.300 (0.008)	949.000 (0.008)	2540 (60)	-0.890 (0.042)
32	753.5 (0.6)	871.299 (0.008)	944.000 (0.008)	2560 (70)	-2.184 (0.062)
35	756.8 (1.8)	871.370 (0.008)	944.000 (0.008)	2740 (200)	-0.745 (0.034)
36	752.1 (1.5)	871.370 (0.009)	944.000 (0.008)	2790 (90)	-0.300 (0.024)
37	757.1 (0.5)	871.300 (0.009)	944.000 (0.011)	5970 (210)	-0.287 (0.031)
38	753.4 (4.8)	871.300 (0.007)	944.000 (0.007)	1400 (50)	-0.301 (0.029)
39	755.2 (1.6)	871.300 (0.010)	944.000 (0.010)	3340 (60)	-0.293 (0.026)

Table 4.5: Mean and RMS changes in several experimental variables. The numbers in brackets are the RMS change over the dataset. The muon stop z is over the z range -12 cm to 12 cm, where centered is at -0.7 cm, and stopping at 3/4 is at -0.3 cm.

4.4 Data Quality

The history of many of the experimental variables was recorded both in a database, and with the TDC data. The broad categories of variables monitored include proton beam steering, muon beamline element currents and voltages, chamber temperatures, chamber gas flow rates, differential pressures, scaler rates, and variables from a quick offline analysis. Table 4.4 lists the mean and RMS change in several of the experimental variables for each data set used for the measurement of $P_\mu\xi$ (both controlled and uncontrolled).

Feedback was used to keep three of the experiment variables fixed. Regulation of the two beamline bending magnet currents using an NMR read back was employed. The regulation kept the bending magnet fields fixed to better than 0.01 G. The mean last plane hit by the muon was also controlled for sets 35 to 39 with feedback to the CO_2/He degrader gas flow rates. The distributions of the muon last plane hit from the data and MC sets used to obtain a measurement of $P_\mu\xi$ are shown in Figure 4.3.

The simulation does not include any pions, and this is the reason for the lower number of muon stops at higher plane numbers in the MC. A systematic uncertainty due to "background muons" from pion decays near the entrance of the detector is estimated in Section 6.1.5. Also noted is that for the data sets stopping at 3/4, the simulation muon stopping distribution was moved too far downstream. The systematic shift in $P_\mu\xi$ due to this discrepancy in muon stopping distributions is $< 0.04 \times 10^{-3}$.

The DC plane drift times depend on the location of the aluminized Mylar cathode foils. To monitor the position of the foils two regions, A and B, are defined on a DC foil with $r < 5.0$ cm and $9.5 < r < 12.5$ cm, respectively. The mean drift times are compared in these regions. To reduce the statistical error, all upstream DC "sparse stack" data were put together to obtain the difference in drift times ($\Delta t = t_B - t_A$). A positive Δt indicates a negative foil bulge, which is the case for most of the 2004 data. Data taken with the foils bulged known amounts were used to calibrate the bulge size. For the upstream DC "sparse stack" the calibration curve is:

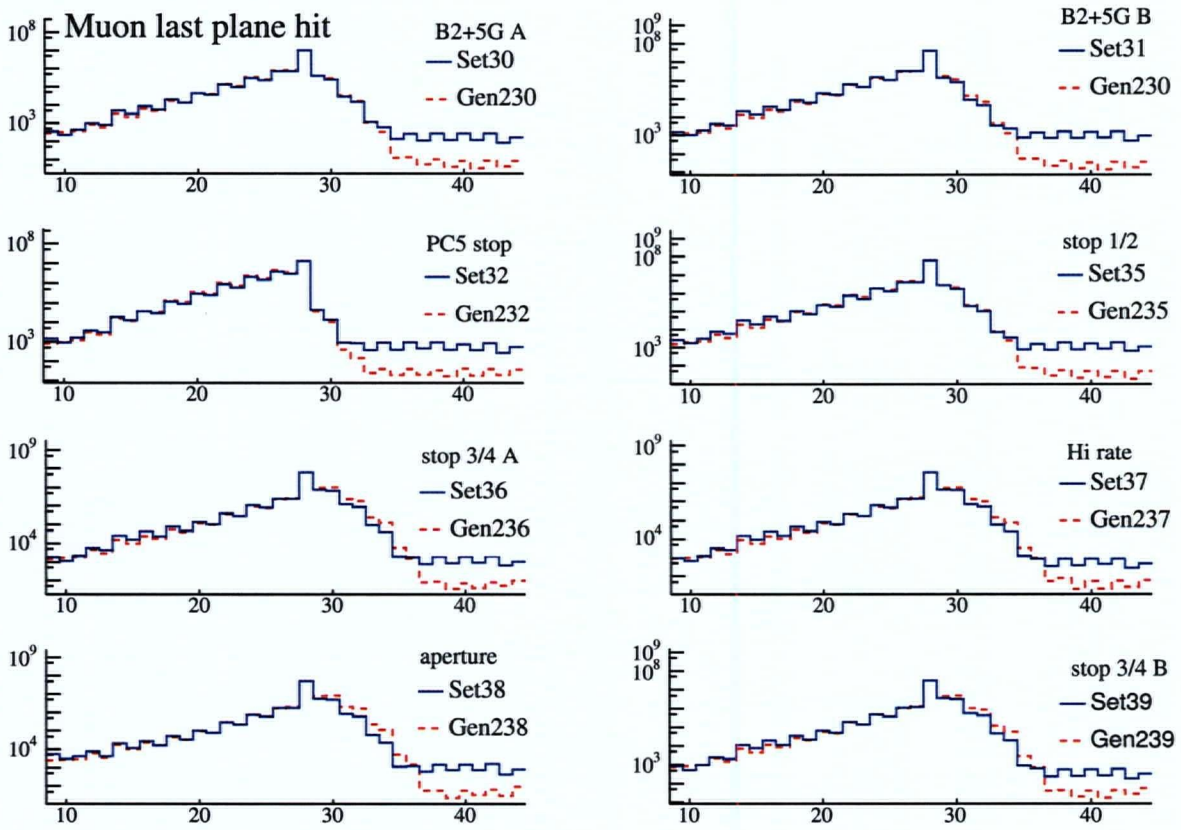

Figure 4.3: Overlay of the muon stopping distribution as a function of last plane number hit, where the MC is in red and the data is in blue.

$$\Delta t = -3.28525 + 0.30664P - 0.00254P^2 \tag{4.2}$$

where the drift time difference, Δt, is in ns, and the differential pressure between He and DME volumes, P, is in millitorr. A 1.0 ns change in Δt corresponds to a change in differential pressure of 4.15 mTorr. For the flattest cathode foils, the differential pressure between the He and DME is nominally $P = 107.8$ mTorr. Table 4.6 lists the foil position offset from nominal. A negative number means the foil was flexed towards the wires. The uncertainty in the estimate, due to statistics, calibration, region definition, foil shape, foil tilt and, temperature variation, is < 25.0 μm.

Set #	Abbreviation	Offset (μm)	Variation (μm)
30	B2+5G A	-10.0	30.0
31	B2+5G B	-50.0	55.0
32	PC5 stop	-75.0	45.0
35	stop 1/2	-30.0	45.0
36	stop 3/4 A	-25.0	55.0
37	hi rate	-25.0	50.0
38	aperture	-20.0	65.0
39	stop 3/4 B	-15.0	40.0

Table 4.6: Estimate of the average DC foil bulge for 2004 data sets.

Chapter 5

Simulation

The measurement of the muon decay parameters comes from fits to simulated data. By fitting to simulated data, it is possible to account for the detector resolution and acceptance. The simulation is based on GEANT3[51]. The production simulation used for comparison with the data has all the physics processes turned on, including positron energy loss in matter, multiple scattering, delta electron production, primary photon conversion, Bhabha scattering (electron-positron scattering), and hard scattering (backscatters). The output from the simulation is digitized data in the same format as the data acquisition (DAQ). Simulation specific information is included in the output for estimating efficiency, detector response, and other studies.

Additional inputs to the simulation that are not specific to GEANT are described in this chapter. The additions to the simulation include: the muon decay spectrum generation including radiative corrections, a detailed detector geometry that matches the real detector measurements, the chamber and TDC responses, muon and positron beam pile-up, beam position and angle distributions, muon spin tracking, and material dependent muon depolarization. The final section of this chapter will discuss the validations of the simulation.

5.1 Muon Decay Spectrum and Radiative Corrections

The decay positron spectrum from muon decay is coded into the simulation in terms of the muon decay parameters. The muon decay parameters are set from blackbox values that are within a few percent of the standard model values where the maximum changes allowed are: $d\rho = 0.01$, $d\eta = 0.03$, $d\xi = 0.01$, and $d\delta = 0.01$.

Since photons are not detected in this experiment, the measured decay positron spectrum needs to include the effect of photon emission by inner bremsstrahlung(IB). This type of bremsstrahlung, from the muon or positron, occurs because of the abrupt change in the electric field where the muon decays. Also important is the effect of photons on the vertex (vertex renormalisation) and on the muon and decay positron (mass dressing). The Feynman diagrams for the first order corrections are shown in Figure 5.1. Only diagrams (c) through (e) in this figure are part of the radiative corrections, while (a) and (b) are mass normalisations. Note that because the W boson mass is large compared to the muon, electron and neutrino masses, it is not included in the calculations of the radiative corrections. The interaction is assumed to be a four fermion point interaction.

Since the effect of first order radiative corrections on the decay positron spectrum is large, additional corrections are needed for precision measurements. The analysis in this thesis includes full $\mathcal{O}(\alpha)$ radiative corrections with the exact electron mass, leading and next

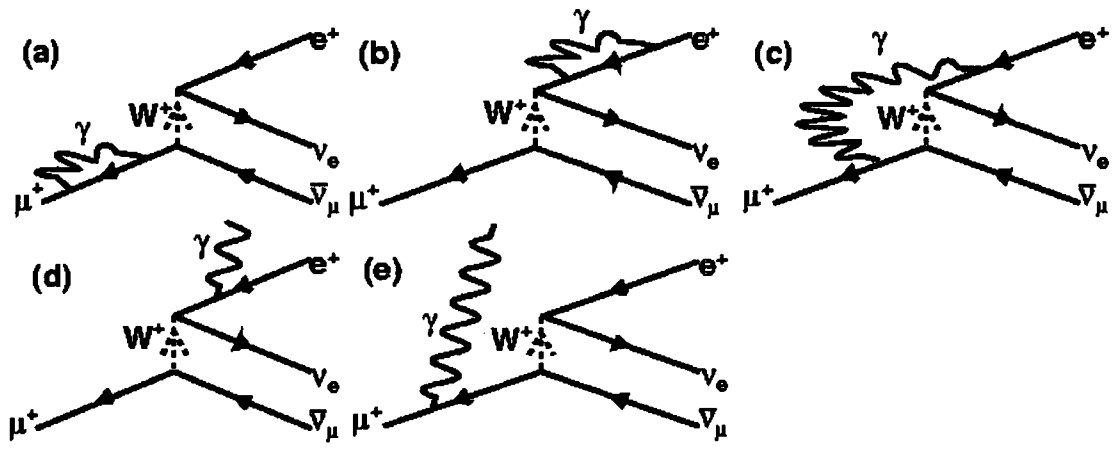

Figure 5.1: Feynman diagrams of radiative corrections to: (a) muon propagation, (b) positron propagation, (c) decay vertex, (d) positron Inner Bremsstrahlung, and (e) muon Inner Bremsstrahlung.

to leading logarithmic terms of $\mathcal{O}(\alpha^2)$, leading logarithmic terms of $\mathcal{O}(\alpha^3)$, corrections for soft pairs, virtual pairs, and an adhoc exponentiation. The exact forms used can be found in the references [52, 53, 54, 55, 56, 57, 58].

5.2 Geometry

The simulation includes detailed geometry of the detector containing the components of the hardware with which a muon or decay positron could interact. The wire chamber foils, individual wires, gas, G10 support, and Sital spacers are included. The positioning of the planes was adjusted by the measured translational and rotational alignments. The simulation included the beam package and solenoid yoke. To reduce the CPU time that would be needed for showers in the magnet yoke, the tracking of positrons was terminated once the yoke was hit.

5.3 Chamber Response

The chamber response is simulated by randomly creating ionization clusters along the path of a charged particle it follows when crossing a drift cell. The drift time for each cluster comes from a space to time relationship (STR) that is calculated by a GARFIELD simulation [45, 59]. The overlap of different clusters is used to produce a signal when it is above a statistical threshold of 1.6 clusters. The signal timing is smeared by a Gaussian with $\sigma = 3$ ns to simulate the electronics' time resolution. Parameters for the threshold and time smearing are tuned to match the data TDC time distributions[60].

5.4 Beam Input

The beam input includes muons and beam positrons, but not pions. The muon is always the trigger particle in the simulation, while in the data up to 10% of the triggers are from beam positrons. The muon and beam positron rates are determined from measurements of the rates in data, and statistical pileup of the beam particles is also simulated in the simulation. The beam positron rates used in the simulation come from an estimate of the rate from the ratio of simple muon decay events to muon decay events that also contain one or more beam positrons separated in time from the muon or decay positron by > 1 μs. The total rate estimated for muons plus beam positrons for the 2004 data is shown in Figure 5.2. The beam positron rate in 2004 was much lower than in 2002 because of the insertion of vertical apertures in the beamline, and because the muon production target was changed from a beryllium target to a graphite target.

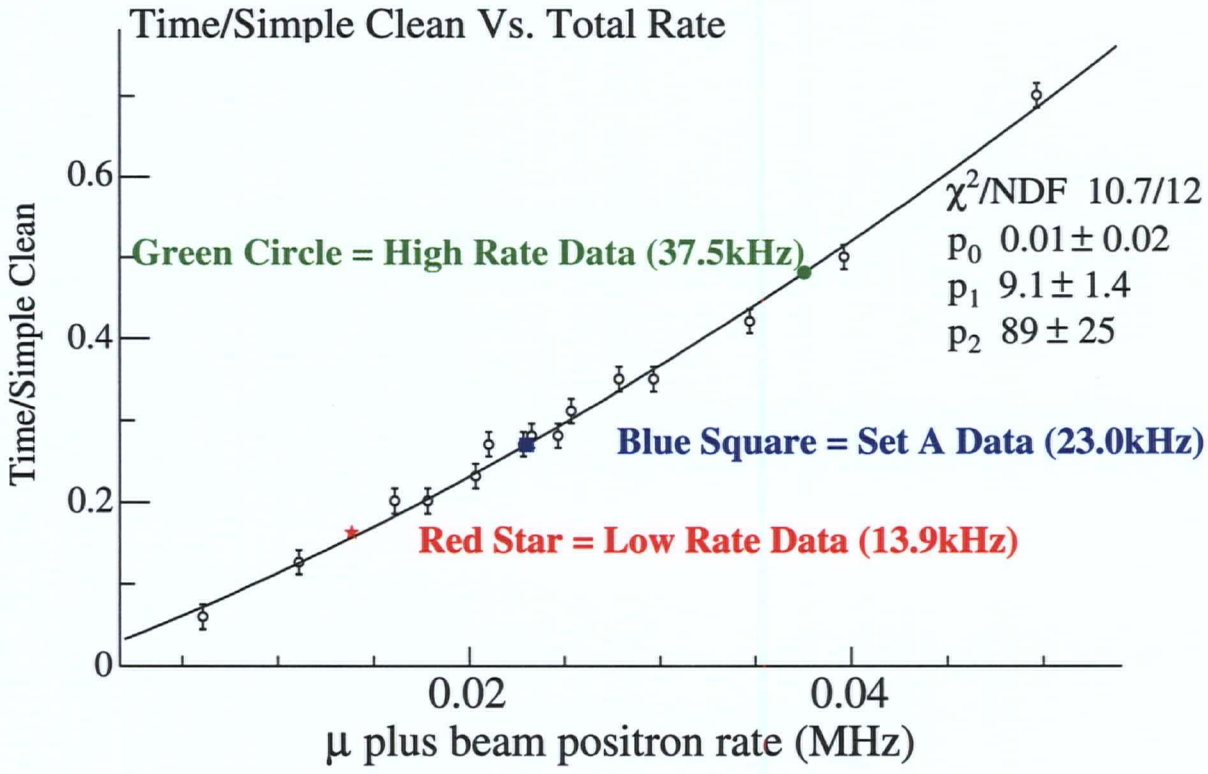

Figure 5.2: Total rate estimated for muons plus beam positrons for the 2004 data. The beam positron rate is taken from this total rate estimate minus the muon scintillator rate. One of the 2002 data sets is included for reference.

The muon beam distribution in position and angle, input to the simulation, comes from the TEC measurements. Some details of the TEC measured beam are in Section 2.12.4. The inputs to the simulation are: the probability of a muon at each y versus x, the mean

angle of the muon in x, $<dx>$, and y, $<dy>$, for each y versus x, and the RMS of the angle distributions at each y versus x. The simulation throws a random number for x, y, and the probability. If the point is accepted, then random Gaussian numbers are thrown with mean given by the $<dx>$ and $<dy>$ at the x and y point thrown. The σ of the Gaussian is from the "deconvolved" RMS angles at the x and y position thrown. For more discussion of the TEC measurements of the beam refer to Section 2.12.

5.5 Spin Tracking

GEANT transports charged particles in a magnetic field using a classical fourth order Runge-Kutta, using the Nystroem algorithm. The tracking of the muon spin is done using the same Runge-Kutta method, and uses the BMT equation, presented in Section 1.5.5, to propagate the spin through the magnetic field. The accuracy of this numerical integration is very good, but it depends on the knowledge of the input beam parameters and the magnetic field map and its interpolation.

Tests of the spin tracking, in a constant field in vacuum, were done to check that the spin remains parallel to the momentum with the implementation of the formula in the simulation. It was also checked the spin remains parallel and antiparallel at a level $\ll 10^{-4}$ when tracking through the field map with all physics turned off [61].

5.6 Muon Depolarization in Material

Two different models for muon depolarization were included in our simulation. The depolarization rates in the muon stopping target and all other materials can be chosen differently. The two depolarization rates coded are for an exponential or a Gaussian shape. Section 6.1.4 contains a discussion of the material dependent muon depolarization mechanisms.

5.6.1 Gaussian Depolarization

To obtain a muon depolarization rate of the form:

$$P_\mu(t) = P_\mu(0)e^{-\frac{t^2}{2\sigma^2}}, \tag{5.1}$$

from a collection of muons, we start with the muon spins all anti-aligned with the muon momentum. We define the fraction that have not flipped, $\text{spin}_z = -1$, as $g = 1$, and the fraction that have flipped, $\text{spin}_z = +1$, as $f = 1 - g = 0$. The polarization of this collection of muons is then $P_\mu(0) = 1 - 2g$. Then at some later time t we have:

$$\begin{aligned} 1 - 2g = &\ -e^{\frac{-t^2}{2\sigma^2}}, \\ g = &\ 0.5 * (1 + e^{\frac{-t^2}{2\sigma^2}}), \text{ and} \\ f = 1 - g = &\ 0.5 * (1 - e^{\frac{-t^2}{2\sigma^2}}). \end{aligned} \tag{5.2}$$

Then for each muon decay at time t we can throw a uniform random number, U, between $[0 : 1]$. We flip the spin if:

$$\begin{aligned} U < &\ f, \\ ie.\ U < &\ 0.5 * (1 - e^{\frac{-t^2}{2\sigma^2}}). \end{aligned} \tag{5.3}$$

5.6.2 Exponential Depolarization

This subsection shows that the exponential depolarization rate measured in the data is related to the theoretical spin flip time. We define the population of muons at time t, with $\text{spin}_z = -1$, as N_a, and the population with $\text{spin}_z = +1$ as N_b. The rate of spin flip, λ_s, is independent of whether the spin is -1 or $+1$. The rate of muon decay is λ_d. The initial condition at $t = 0$ is $N_a = N_0$, meaning that all muons have spin$= -1$, and $N_b = 0$. Then, the rate of change of population N_a and N_b are:

$$\begin{aligned} \frac{dN_a}{dt} &= -\lambda_s N_a + \lambda_s N_b - \lambda_d N_a, \text{ and} \\ \frac{dN_b}{dt} &= -\lambda_s N_b + \lambda_s N_a - \lambda_d N_b. \end{aligned} \tag{5.4}$$

After some algebra, differentiation, and substitutions of the above two equations we can decouple the differential equations and obtain for N_a:

$$\frac{d^2N_a}{dt^2} + 2(\lambda_s + \lambda_d)\frac{dN_a}{dt} + (2\lambda_s\lambda_d + \lambda_d^2)N_a = 0. \tag{5.5}$$

The roots, r_1 and r_2, of the equation above are:

$$r_1, r_2 = -(\lambda_s + \lambda_d) \pm \lambda_s. \tag{5.6}$$

Imposing the initial conditions, and $N_a(\infty) = 0$ gives us the population of muons with $\text{spin}_z = -1$ of:

$$N_a(t) = \frac{1}{2}N_0 e^{-\lambda_d t}(1 + e^{-2\lambda_s t}). \tag{5.7}$$

Similarly,

$$N_b(t) = \frac{1}{2}N_0 e^{-\lambda_d t}(1 - e^{-2\lambda_s t}). \tag{5.8}$$

The total population of the muons decreases exponentially at the rate λ_d. The muon polarization is the ratio of the number of muons with $\text{spin}_z = -1$ over the total population of muons:

$$\begin{array}{ll} P_\mu(t) = & \frac{N_a(t) - N_b(t)}{N_a(t) + N_b(t)}, \text{ and} \\ P_\mu(t) = & e^{-2\lambda_s t}. \end{array} \tag{5.9}$$

This means that the exponential depolarization rate measured in the data should be exactly a factor of two different than the spin flip time.

5.7 Validation

The simulation was tested by taking data under special conditions, generating simulated data under the same conditions, analyzing both the special data and the matching simulation with the same software, and verifying that the effects are the same in both. Validation studies done include adding extra material outside the detector, comparing hits per plane, comparing muon last plane hit distributions, comparing rates for identified secondary particles, and comparison of the energy loss and multiple scattering. This section will focus on the comparison of energy loss and multiple scattering, of positrons, between simulation and data. Comparison of other simulation and data distributions can be found throughout this thesis.

The validation of GEANT multiple scattering and energy loss was done using far upstream stops for both data and simulation. The analysis of this data was done by another graduate student, Rob MacDonald. For far upstream muon stops, the decay positrons traverse the entire detector stack. The decay positrons are fit upstream and downstream separately. The difference in momentum, Δp, and angle, $\Delta\theta$, between the upstream and downstream fits yield estimates of the energy loss and scattering, respectively. The distributions of $\Delta p \cos\theta$ from the data and simulation are shown in Fig. 5.3.

The matching of the tails of the energy loss distribution, and the scattering angle distribution have been shown to be good to better than 4.0% and 8.0% respectively. One third of our hard interaction energy loss comes from Bhabha scattering, so an estimate of the uncertainty in the hard interactions is taken as:

$$\frac{1}{3}8\% + \frac{2}{3}4\% \approx 5\%. \tag{5.10}$$

Thus 5.0% is used as a measure of how well the analysis of hard interactions in the simulation match the analysis of hard interactions in the real data. The widths of the distributions are slightly different in the simulation and the data, and this difference also appears as different endpoint resolutions as reported in Section 3.6. Intermediate interactions with $|\Delta p| < 1$ MeV/c , from this comparison look reasonable. For intermediate interactions we assume that the match between data and simulation is better than 5%, but a method for showing this has not been quantified. This accuracy seems reasonable based on the claimed accuracy of GEANT3([51], section PHYS001):

> "the cross-sections of the electromagnetic processes are well reproduced (within a few percent) from 10 keV up to 100 GeV, both for light (low Z) and for heavy materials".

A validation of the multiple scattering comes from a comparison of $\Delta\theta$ between simulation and data. The mean of this distribution represents a mean multiple scattering angle. The mean $\Delta\theta$ for the data is 49.5 ± 0.2 mrad and for the simulation is 50.23 ± 0.08. Thus there is a discrepancy of 0.73 ± 0.22 mrad in the multiple scattering, which also shows up as the slope in the percent difference between data and simulation. Figure 5.4 shows an overlay of $\Delta\theta$ in the simulation and in the data.

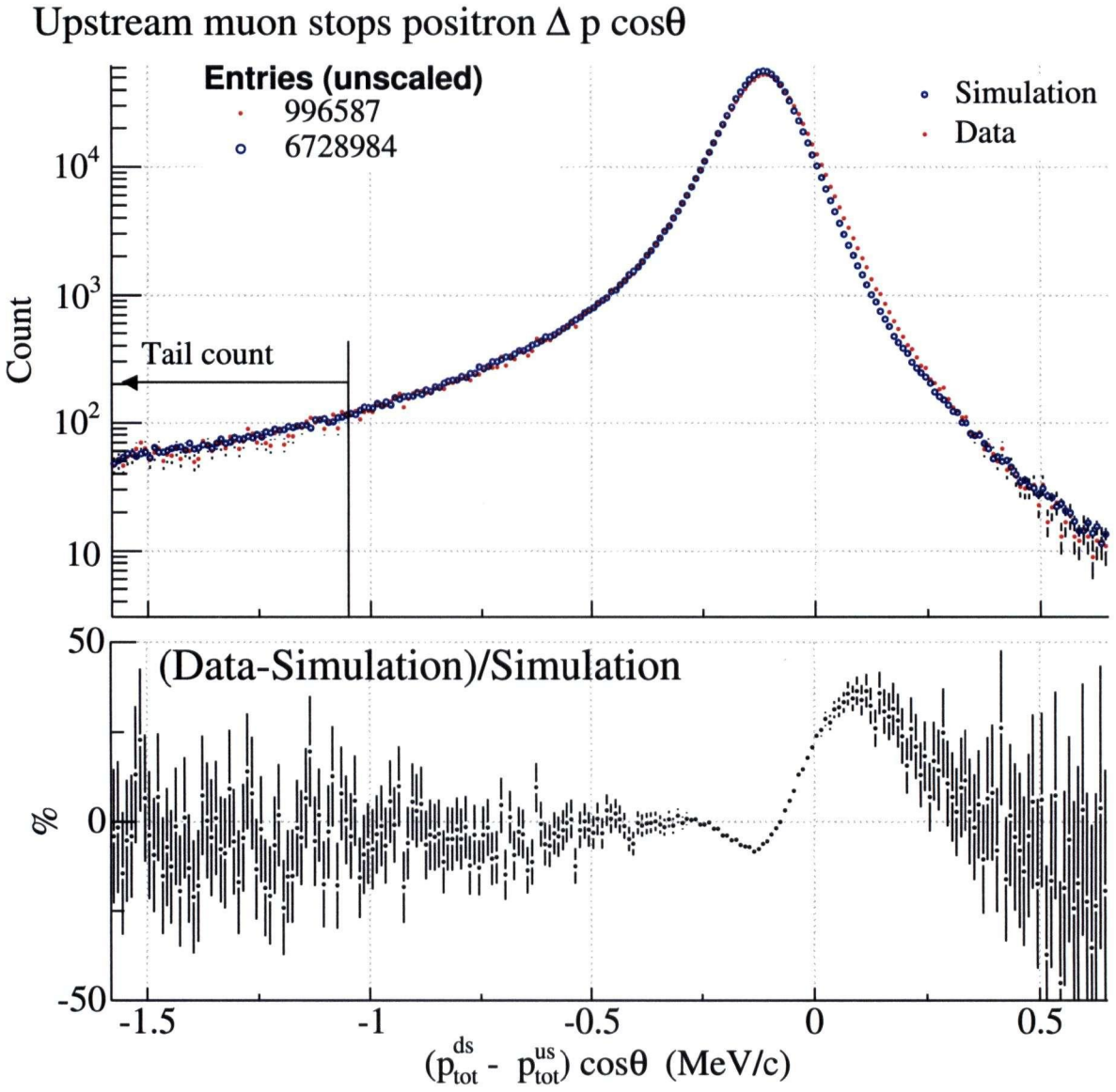

Figure 5.3: Energy losses, from an analysis of the decay positrons from far upstream muon stops, in data and simulation, are overlaid in the top plot, and shown as a percent difference in the bottom plot.

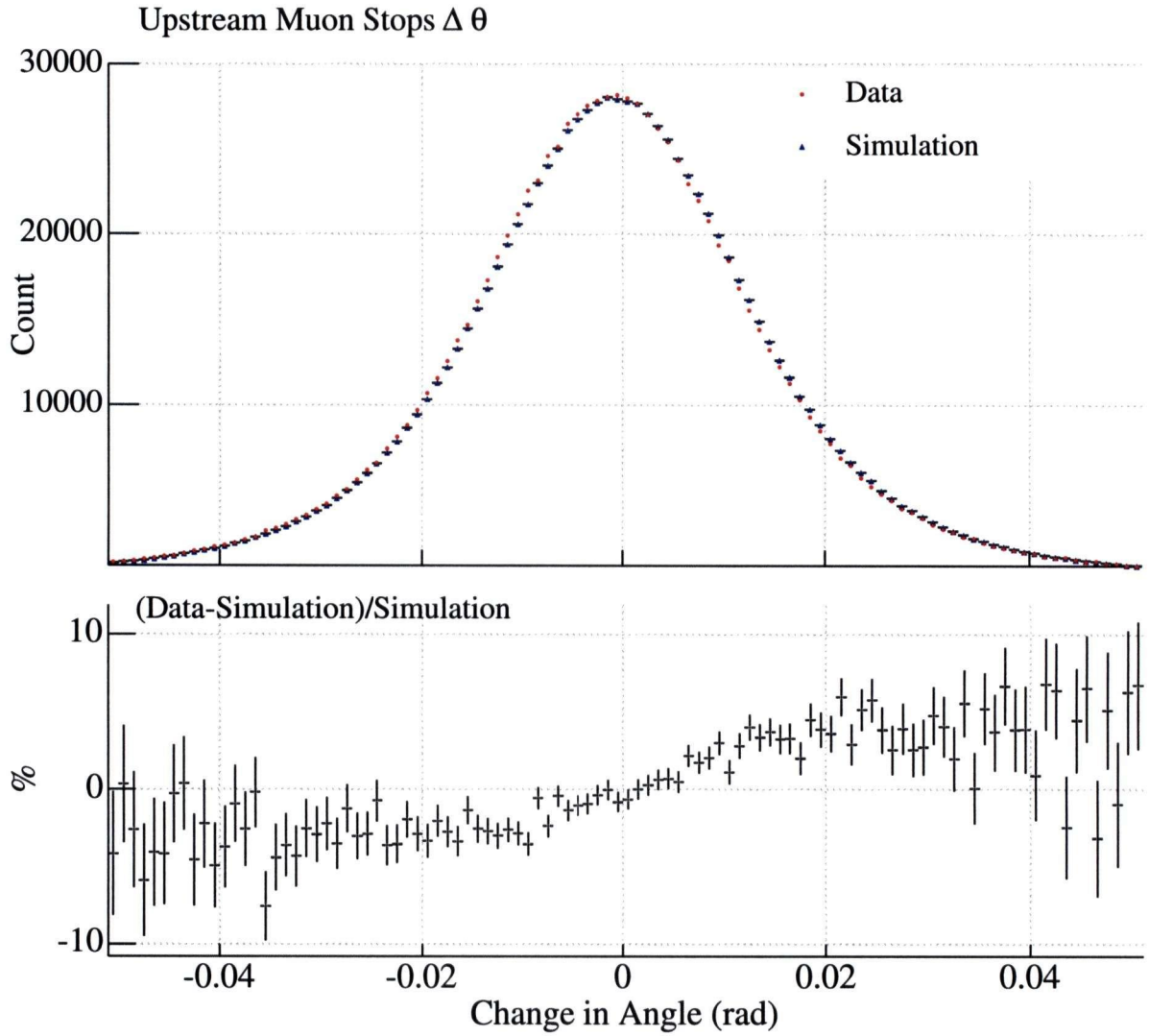

Figure 5.4: Match of multiple scattering angle in the data and simulation from an analysis of the decay positrons from far upstream muon stops. The top plot overlays the simulation and data distributions, and the bottom plot shows the percent difference between data and simulation.

Chapter 6

Systematic Uncertainty Descriptions and Estimates

In this chapter the systematic uncertainties related to the measurement of $P_\mu\xi$ are estimated. The overall systematic uncertainty is estimated as the quadrature sum of individual sensitivity measurements S_i divided by a scale factor. The scale factor comes from the change R_i introduced to measure the sensitivity to the systematic effect over the RMS change (σ_i) in the systematic effect in data. The total systematic uncertainty is thus equal to:

$$\epsilon_{sys}^{tot} = \sqrt{\sum_i \frac{\sigma_i^2}{R_i^2} S_i^2}. \tag{6.1}$$

Systematic uncertainties are divided into set dependent uncertainties, and set independent uncertainties. The set dependent uncertainties are added in quadrature with the individual set statistical uncertainties in calculating the weighted average offset of $P_\mu\xi$ from the black-box value. The detailed listing of the systematic uncertainties is given in Table 6.1. The uncertainties labelled with (ave) were considered to be set dependent. The total systematic uncertainty of $\pm 3.8 \times 10^{-3}$ is obtained for this measurement of $P_\mu\xi$. The estimate for fringe field depolarization systematic uncertainty dominates the measurement uncertainty.

In many cases the error in the sensitivity measurement was larger than the sensitivity itself, such that a meaningful sensitivity was not measured. For those cases, the random value that we determined for the sensitivity was used in the same way as the other measured sensitivities. It is expected that on average this method should give the best statistical estimate of the systematic uncertainty [62].

It should be noted that every effort was made to try to avoid double counting of the systematic uncertainty by separating effects into orthogonal uncertainties. Inevitably there will be some overlap.

The following sections discuss in detail the systematic uncertainties categorized as:

1. muon beam characteristics and polarization
2. chamber response
3. momentum calibration
4. positron interactions
5. spectrometer alignment

Category	Sensitivity S_i Value	Sensitivity S_i Error	Scale R_i/σ_i	Systematic Uncertainty
Muon beam and polarization				±3.69
Fringe field (ave)				3.40
Depolarization in stopping material (ave)				1.40
Depolarization in production target				0.21
Background muon contamination (ave)				0.18
Beam intensity (ave)	-3.0	1.7	16.3	0.18
Chamber response				±0.98
t0 variations (ave)	8.9	0.9	10	0.89
Foil bulges (ave)	2.2	1.4	10	0.22
Cell asymmetry	-0.2	1.4	1	0.22
Up-down efficiency	1.9	0.9	10	0.19
Density (ave)	2.4	1.4	14.3	0.17
Dead zone	0.2	1.4	12	0.01
Spectrometer alignment				±0.31
z	2.2	1.0	10	0.22
Rotations	8.5	0.8	39	0.22
B field to axis	1.2	1.4	40	0.03
Translations	0.1	0.8	28	0.00
Positron interactions				±0.30
Hard and intermediate interactions (ave)				0.29
Multiple scattering	-3.2	1.4	40	0.08
Outside material	1.2	2.0	60	0.02
Energy Loss	0.6	0.2	100	0.01
Momentum calibration				±0.19
End point fits				0.16
B uniformity	-0.9	0.4	10	0.09
Theoretical radiative corrections				±0.10
Total In Quadrature				±3.8

Table 6.1: Table of Systematic Uncertainties in $P_\mu \xi$ in units of $\times 10^{-3}$. The top line of each category shows the quadrature sum of the systematic uncertainty for that category. The average systematic uncertainties are given for the set dependent systematic uncertainties denoted with (ave). In the case that a sensitivity was measured using correlated analyses, the error in the sensitivity was multiplied by the square root of the fit $\chi^2/NDOF$.

For the systematic uncertainties that change from set to set, the method of obtaining the overall systematic uncertainty, and the set to set variation are discussed in the relevant sections. A tabulation of the set-to-set uncertainties is in the final section of this Chapter.

6.1 Systematic Uncertainty Due to Muon Beam Characteristics and Polarization

In bringing the muon beam to a stop at the center of the *TWIST* spectrometer, the muons can be depolarized by the combination of multiple scattering and interaction with the fringe field of the spectrometer, and by spin relaxation or other interactions in the vicinity of the muon stopping target.

This section will discuss the systematic uncertainties due to:

1. muon depolarization in the production target,
2. muon depolarization in the beamline window valve,
3. muon beam transfer through the solenoid fringe field,
4. muon depolarization at the stopping location,
5. beam contamination with background muons,
6. beam intensity and accidental particles, and
7. proton beam stability.

Note that the muon depolarization in the beamline window valve is estimated in this section, but not included in the overall table of systematic uncertainties because its effect is very small.

6.1.1 Depolarization in the Muon Production Target

This section estimates the systematic uncertainty due to depolarization in the production target. The effect is estimated to be negligible compared to the statistical uncertainty obtained with the data taken in 2003 to try to measure this effect. The 2003 data are not being used since the uncertainty in $P_\mu \xi$ from the data to data fit is too large to be useful.

The M13 beamline has $\frac{\delta p}{p}$ of 1% (FWHM) meaning that we have a range of roughly 29.4 to 29.8 MeV/c for our nominal surface muon beam momentum of 29.6 MeV/c. To obtain a conservative estimate of the depolarization in the production target we include a little extra for tails of the non Gaussian distribution. This is a range of 0.4 MeV/c.

For this momentum, $\frac{dp}{dx}$ is about 55 MeV/c/(g/cm^2) in the graphite production target described in Section 2.10. Thus the difference in thickness corresponding to 0.4 MeV/c, which is a good estimate of the effective maximum depth from which our muons are born, is 0.007 g/cm^2. Using a density of 2.26 g/cm^3, the production depth is 0.003 cm of graphite.

Using the multiple scattering formula in Equation 6.2, the multiple scattering angle in graphite can be estimated. X_0 is 42.7 g/cm^2, so $x/X_0 = 0.007/42.7 = 0.00016$, which is well below the quoted range of validity for the multiple scattering formula. However, for muons moving with velocity $\beta = 0.265$, we obtain $\theta_{space}^{RMS} = 0.0206$ rad.

$$\theta_{space}^{RMS} = \sqrt{2}\frac{13.6MeV}{\beta cp} z\sqrt{x/X_0}[1 + 0.038 \ln x/X_0]. \quad (6.2)$$

An estimate of the depolarization in the small angle approximation is $(\theta_{space}^{RMS})^2/2$. This works out to a contribution of 0.21×10^{-3} to the systematic uncertainty in $P_\mu\xi$.

6.1.2 Depolarization in the Beamline Window Valve

An 0.0003 cm thick polyester foil was inserted in the beamline to reduce the amount of beam gas making it to the end of the beamline. The density of polyester is about half the density of graphite, so using the arguments of the previous section we find $\frac{dp}{dx}$ is about 28 MeV/c/(g/cm^2), meaning the muons lose about 8 keV going through the foil. Using the PDG multiple scattering formula with $X_0 = 40.0$ g/cm^2 the value of x/X_0 is 0.000010. For muons with velocity $\beta = 0.265$, we obtain $\theta_0 = 0.0031$. Using the small angle approximation for depolarization this works out be be a contribution to the systematic uncertainty in $P_\mu\xi$ of 5×10^{-6}.

6.1.3 Fringe Field Depolarization (FFD)

This subsection describes the systematic uncertainty in $P_\mu\xi$ due to the apparent depolarization of muons passing through the fringe field of the TWIST solenoid. The systematic uncertainty is estimated from a combination of: beam position and angle uncertainty, uncertainty in the magnetic field shape in the fringe field region, and the deconvolution of the beam angle distribution widths measured with the TEC.

The final systematic uncertainty in $P_\mu\xi$ due to fringe field depolarization will be described in detail in the following sections on:

1. beam position and angle uncertainty ($\pm 3.3 \times 10^{-3}$),
2. deconvolution of the TEC beam angles ($\pm 0.7 \times 10^{-3}$),
3. magnetic fringe field shape ($\pm 0.3 \times 10^{-3}$), and
4. beam size reproduction ($\pm 0.35 \times 10^{-3}$).

The total systematic uncertainty in $P_\mu\xi$ due to fringe field depolarization is $\pm 3.40 \times 10^{-3}$. A conservative estimate has been made since a data validation of our simulation polarization estimates was not obtained.

FFD: Beam Position and Angle Uncertainty

In this section the sensitivity and systematic uncertainty in $P_\mu\xi$ due to beam position and angle is estimated. The uncertainty in the beam measurement is estimated by comparing the range of predicted polarizations in the simulation for the different beam tunes used in data taking.

To confirm the systematic uncertainty chosen, another estimate based on a best guess at the uncertainty in the TEC to yoke alignment is reviewed. In Section 2.12.3, the uncertainty in the beam position was estimated to be ±2 mm in any direction, and the uncertainty in the beam angle was estimated to be ±5 mrad.

Another measure of the uncertainty in the beam measurement comes from a comparison of the muon beam as seen inside the detector in both simulation and Data. The u and v coordinates of the muon, at the last two PCs before the muons stopping target, are available from the output of the analysis of both data and simulation. From distributions of the muon u and v coordinates, the average (<u> and <v>) and RMS (RMS u, RMS v) values can be compared between data and simulation. The comparison of these muon beam parameters is shown in Fig. 6.1. The mean positions in the data and simulation track each other fairly well, with differences in position of < 1.5 mm in <u> and < 1 mm in <v>. The RMS size of the beam is about 1.5 mm larger in simulation than in data. The uncertainty due to the poor reproduction of the beam size is discussed in Section 6.1.3. Comparing the <u> and <v> between Set 30 and Set 35 shows that the beam moves about 5 mm inside the detector when B2 is changed by 5 G. This is a consequence of the focusing effect of the solenoid field, since the beam at the TEC moves by about 10 mm when B2 is changed by 5 G.

To estimate the sensitivity to fringe field depolarization, the beam input into simulation was scanned over the range ±2 cm and ±20 mrad in both x and y. The result of this scan shows that the polarization versus beam shift can be approximated by a quadratic polynomial. The scan results for the nominal beam are shown in Figure 6.2.

The quadratic function given in Equation 6.5, where the x, y, dx and dy represent the shifts in the positions and angles, was used to fit the data.

$$P_\mu(x, y, dx, dy) = P_{max} + A((dx - x_0)^2 + (dy - y_0)^2). \tag{6.3}$$

The fit constants P_{max} and A were roughly independent of the shift in x and y, while the fit constants x_0 and y_0 were found to be functions of x and y.

Fits to x_0 versus x and y, and y_0 versus x and y can be done to find the constants in the linear equations:

$$\begin{aligned} x_0 &= x_{00} + x_{0x}\ x, \\ x_0 &= x_{00} + x_{0y}\ y, \\ y_0 &= y_{00} + y_{0x}\ x, \text{ and} \\ y_0 &= y_{00} + y_{0y}\ y. \end{aligned} \tag{6.4}$$

The overall four dimensional polynomial can then be written as:

$$P_\mu(x, y, dx, dy) = P_{max} + A[(dx - x_{00} - x_{0x}\ x - x_{0y}\ y)^2 + (dy - y_{00} - y_{0x}\ x - y_{0y}\ y)^2]. \tag{6.5}$$

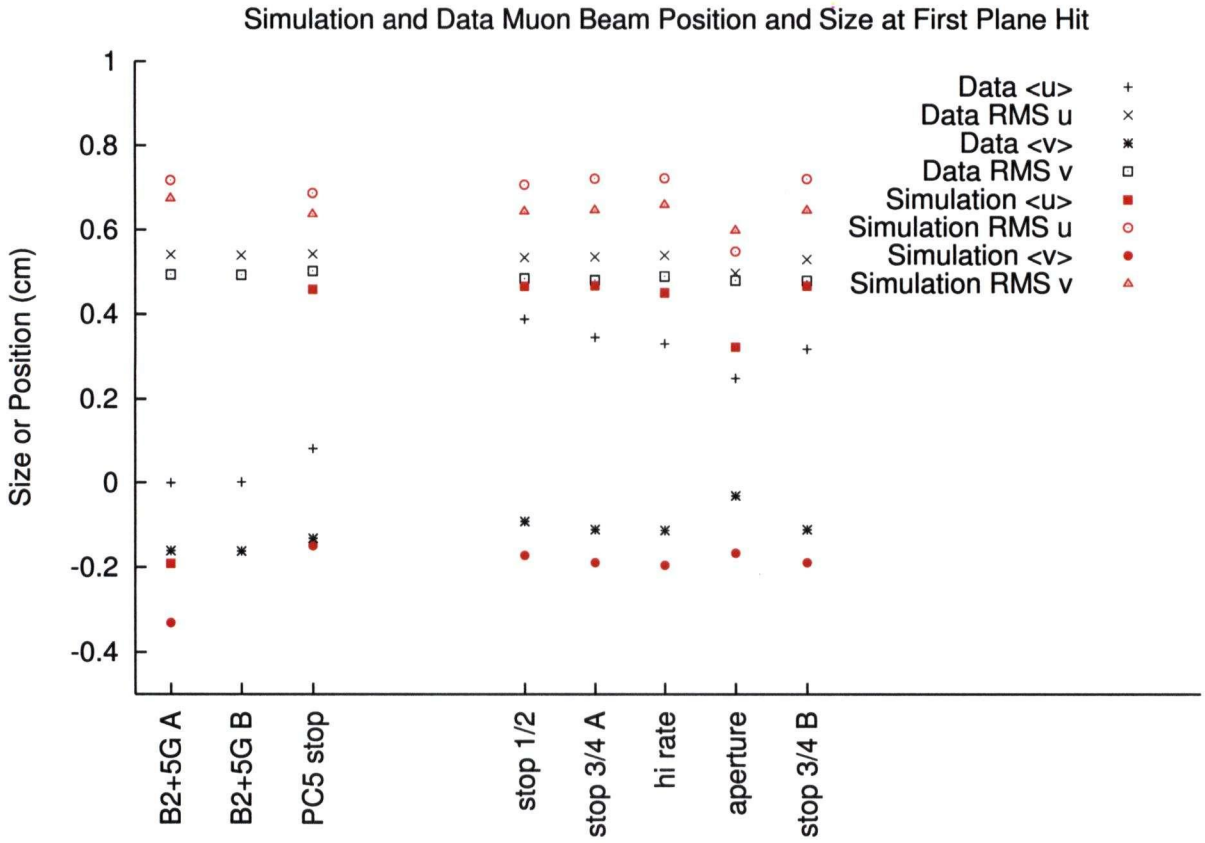

Figure 6.1: The match between the beam position mean and RMS values at the stopping target for each of the data sets considered. The units on the vertical scale are cm.

The constants in this polynomial for the standard beam tune are summarized in Table 6.2. Residuals from the polynomial fit show that the using the polynomial as an estimate of the polarization is only good to about 1.5×10^{-3}.

The four dimensional polynomial can be used to plot the sensitivity of the polarization to the estimated shifts in the beam. For an uncertainty in the beam position of ± 2 mm, and uncertainty in the beam angle of ± 5 mrad, the systematic uncertainty in $P_\mu \xi$ is ± 0.0015 for the nominal beam tune. The systematic uncertainty due to fringe field depolarization for the different beam tunes used in 2004 is summarized in Table 6.4.

A second input to the systematic uncertainty due to the beam comes from TEC runs of the same beam settings taken at different times during the 2004 data taking. Values of the average beam positions and angles from TEC measurements of the beam are summarized in Table 6.1.3. Clearly there were issues with either the alignment or efficiency of the TEC between these two measurements. The relative changes in angle and position between the nominal and B2+5 G are roughly the same, but the absolute numbers for the average beam angle are quite different. To estimate the effect of this change in the beam measurement on

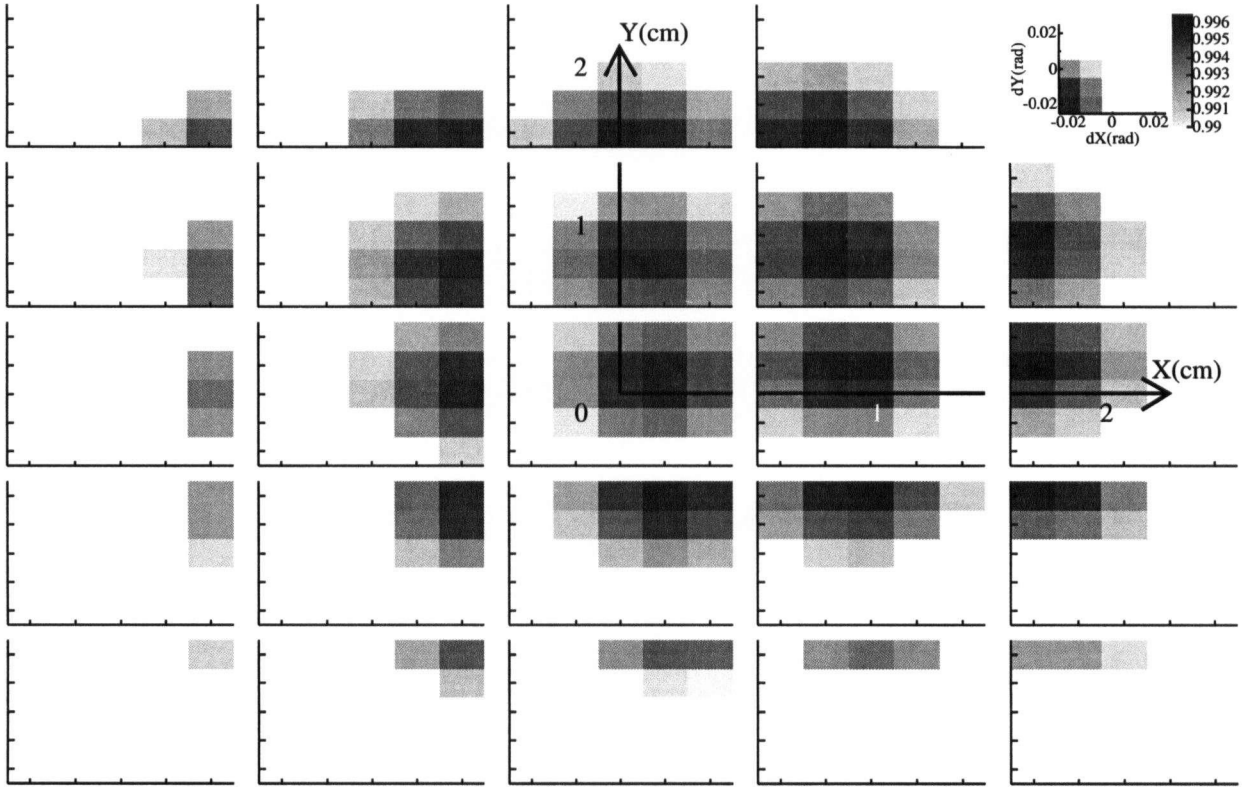

Figure 6.2: Fringe Field Sensitivity simulation Scan showing the mean spin along the z axis for muons that stop in the target, where black is the highest polarization of 0.9965, and the lightest gray is the lowest polarization of 0.99. An unshaded or white square is lower polarization than 0.99. Each of the 25 plots shown here is a polarization for each shift in dy versus dx from +20 mrad to −20 mrad. The middle plot is for an unshifted beam, plots on the first row are for the beam shifted up by 2 cm at the TEC, the second row shifted up by 1 cm, and so on filling the matrix of beam shifts in x and y from +2 cm to −2 cm.

the polarization estimate, the mean positions and angles were plugged into Equation 6.5 that is described later in this section. The larger difference in polarization of 3.3×10^{-3} between the two measurements of the beam at 949 G is an estimate of the systematic uncertainty in the value of P_μ.

In Section 7.1.1 we note that the values of $P_\mu\xi$ in the data are consistent, while the simulation predicts a difference in polarization of 6.1×10^{-3}. Since the confirmation of the simulation was not obtained yet, and there is some ambiguity in the absolute polarization based on the beam tunes available, half the difference observed in simulation, 3.1×10^{-3}, is an estimate of the systematic uncertainty in $P_\mu\xi$ that is consistent with the 3.3×10^{-3} between the two measurements of the beam at 949 G. The systematic uncertainty in $P_\mu\xi$ is thus quoted as 3.3×10^{-3} due to the ambiguity in absolute polarization predicted by the TEC beam tunes.

Parameter	Nominal tune	Aperture	B2+5 G	High rate	Units
P_{max}	0.9958	0.9976	0.9950	0.9954	
A	-9.796	-10.536	-8.548	-9.831	rad^{-2}
x_{00}	0.0075	0.0067	0.0106	0.0075	rad
x_{0x}	-0.0129	-0.0121	-0.0142	-0.0133	rad/cm
x_{0y}	-0.0032	-0.0021	-0.0041	-0.0030	rad/cm
y_{00}	0.0058	0.0038	0.0167	0.0057	rad
y_{0x}	0.0024	0.0002	0.0020	0.0025	rad/cm
y_{0y}	-0.0137	-0.0122	-0.0149	-0.0138	rad/cm

Table 6.2: Beam polarization polynomial parameters from fit to simulation scans of the different beam tunes.

B2 (gauss)	<x> (cm)	<dx> (mrad)	<y> (cm)	<dy> (mrad)	Polynomial P_μ
949	0.85	-1.1	0.87	-5.0	0.9955
946.5	0.45	-3.4	0.92	1.8	0.9952
944	0.07	-5.9	0.97	7.0	0.9929
941.5	-0.29	-8.3	1.03	10.0	0.9897
949	0.94	-1.5	0.64	-19.2	0.9922
944	0.06	-6.7	0.73	-11.2	0.9941

Table 6.3: Average beam positions and angles from TEC measurements of the beam during a B2 scan. The last two rows show the TEC measurements for the characterization runs used in the simulation.

Beam Tune	Nominal	Aperture	+5 gauss	High Rate
Systematic Uncertainty	± 0.0015	± 0.0015	± 0.0035	± 0.0018

Table 6.4: Systematic uncertainty in $P_\mu \xi$ due to uncertainty in beam position and angle for each of the beam tunes used during 2004 data collection.

FFD: Different Field Maps

This section describes the contribution to the systematic uncertainty in $P_\mu\xi$ due to uncertainty in the magnetic field map in the fringe field region. To estimate the systematic uncertainty due to the quality of the magnetic field maps, several different field maps are considered. The field maps considered are:

1. the nominal field map generated by Opera as described in Section 2.4,
2. a quarter model field map that included steel from two of the beamline quadrupoles on one of the beamline dipoles that are closest to the solenoid[40],
3. a full model 2.0 T field map that was not fully matched to the measurements of the magnetic field [43],
4. a full model 1.96 T field map from the same Opera model as map 2 of this list, but with the currents scaled [43],
5. a 1.96 T field map scaled by 0.98 from the nominal field map, but with the fringe field scaled by 0.955, where the scaling increases in z as a Gaussian that has $\sigma = 20$ cm for $z < -140$ cm, and
6. a 2.04 T field map scaled by 1.02 from the nominal field map, but with the fringe field scaled by 1.045 as in the previous item.

The largest difference in polarization as predicted by simulation for a nominal 2004 beam tune using the field maps enumerated above was $< 0.3 \times 10^{-3}$. This value is used as the systematic uncertainty in $P_\mu\xi$ due to the quality of the magnetic field map.

FFD: Deconvolution of TEC Multiple Scattering

Multiple Scattering in the different components of the TEC broadens the distribution of angles measured. Simulation was used to estimate Gaussian deconvolution factors needed to reproduce the angular distributions of the beam. The factors obtained were 0.615 for the width of the angle in x, and 0.444 for the width of the angle in y (good to about 10%.) To estimate a systematic uncertainty due to deconvolution of the beam angular distributions measured from the TEC, beam inputs with different deconvolution factors were used. A plot of the polarization predicted by the simulation versus deconvolution factor is shown in Figure 6.3. The resulting systematic uncertainty in $P_\mu\xi$ due to deconvolution of multiple scattering in the measured beam input is 0.5×10^{-3}.

The deconvolution does not account for the non-Gaussian tails that the TEC measurement has. To account for this effect, the difference in polarization, 0.5×10^{-3}, predicted by simulation using the TEC aperture characterization run without the aperture inserted in GEANT versus the same characterization run with the aperture inserted is used. If we add in quadrature the contribution to the systematic uncertainty from deconvolution of the central part of the beam, and from the non-Gaussian tails of the beam, the systematic uncertainty in $P_\mu\xi$ due to deconvolution of the TEC beam becomes $\pm 0.71 \times 10^{-3}$.

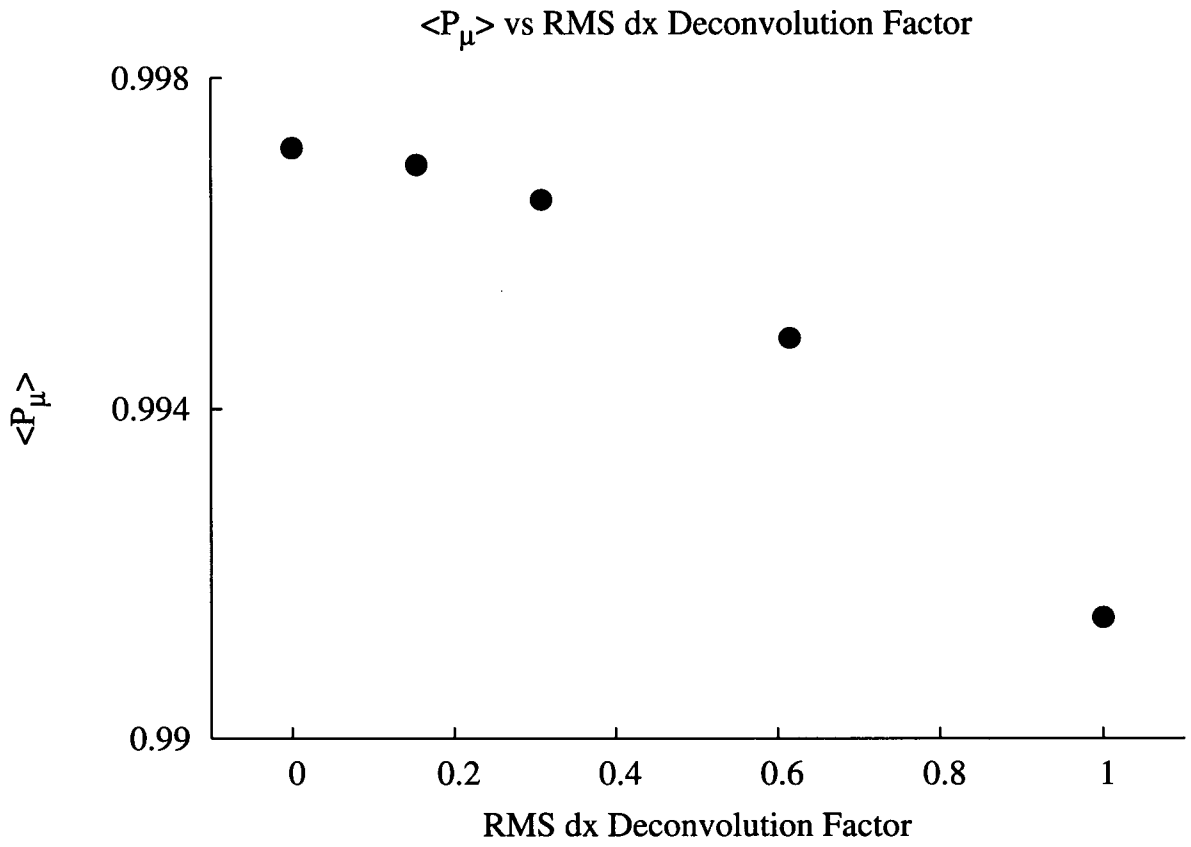

Figure 6.3: Muon polarization versus beam angular width deconvolution factor. Note that the deconvolution factor of the width of the angle in x is plotted here, but that the y deconvolution factor was changed at the same time in the proportion x/y:0.615/0.444.

FFD: Muon Beam Size

The simulated muon beam has been observed to be 1.5 mm larger at the stopping target than the muon beam in data. The RMS beam size at the target versus at the TEC for a scan of different starting beam sizes in simulation, and for data sets 35, 37, and 38 are shown in Fig. 6.4. A scan of the beam size in simulation was done, starting with the beam input file from set 35 for the angle distributions, but imposing a two dimensional (2D) Gaussian for the y versus x profile. The means of the profile were the same as the beam in set 35. While a 2D Gaussian does not include the tails of the real beam, or the correlation between x and y of the real beam, the polarization predicted by the beam, with a Gaussian width the same as the real beam, was found to match at the 10^{-4} level.

The point with zero beam size was simulated using a pencil beam started at $x = y = dx = dy = 0$ at the location of the TEC. It is observed that the pencil beam from the simulation is larger at the stopping target than the real beam in data. To try to understand

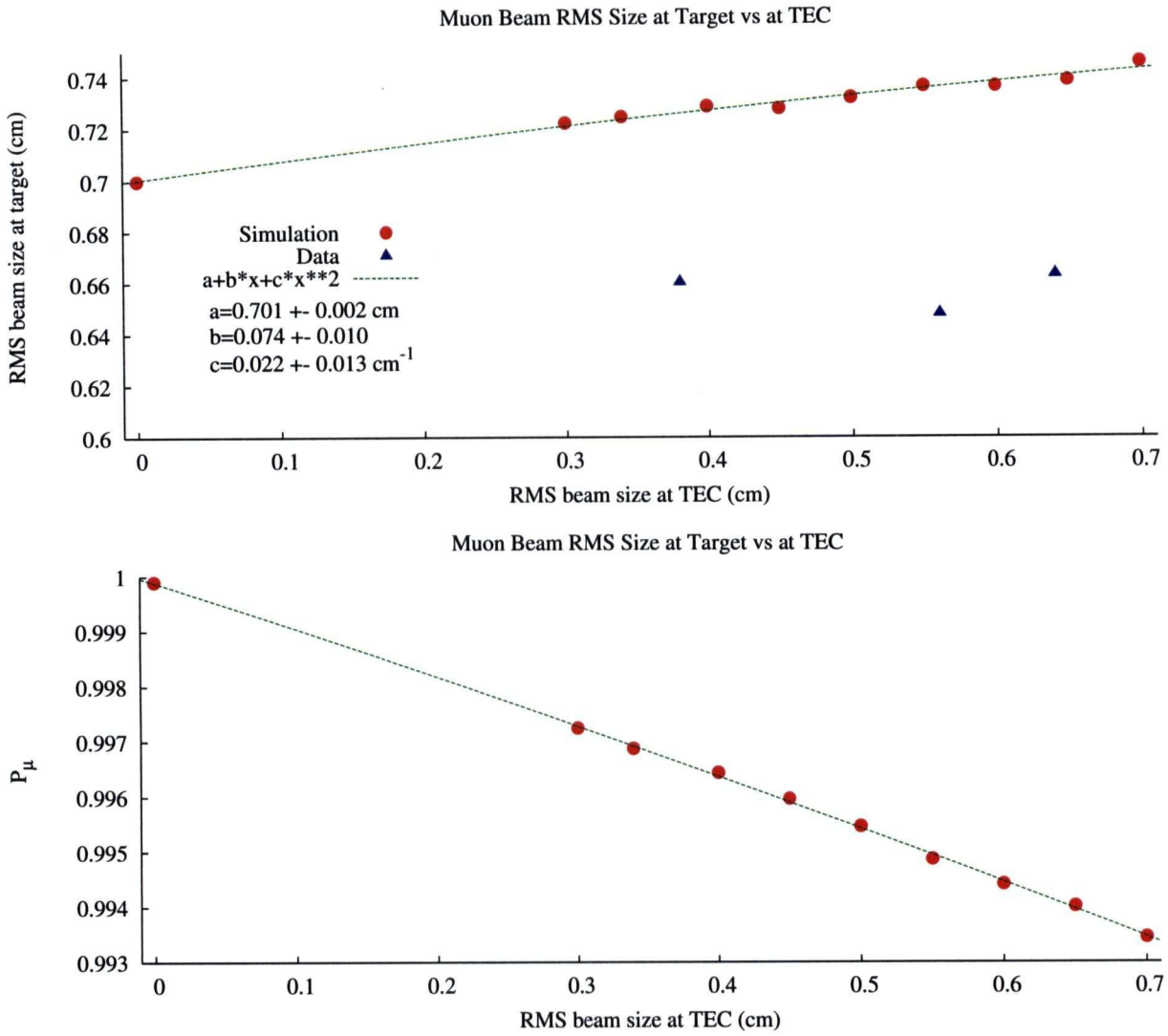

Figure 6.4: The top plot shows the muon beam size at the stopping target versus at the TEC, where the simulation points are solid circes and the data points are solid triangles. The bottom plot shows the muon polarization predicted by the simulation for different muon beam sizes at the TEC.

the source of the large simulation beam size at the stopping target two simulation tests were done. A pencil beam, with all physics processes turned off, was simulated. The result of this simulation was that the muon beam size was zero at the muon stopping target as expected. Then a pencil beam with all physics on, except multiple scattering turned off, was simulated. A muon beam size of 0.045 cm was obtained from this test. The conclusion of these tests is that the muon beam size in simulation is due to the simulation of multiple scattering for muons. Thus multiple scattering of low energy muons in our simulation is predicting a beam size at the stopping target that is larger than in data.

The uncertainty in the final polarization estimate due to a discrepancy in the simulation multiple scattering of muons is very small. As a rough estimate of the mean multiple scattering angle with focusing of the solenoid field, consider the beam size of the pencil beam after about one meter of scattering before coming to a stop: $\theta_0 \approx 0.7$ cm /100 cm ≈ 7 mrad. Using the small angle approximation, $1 - |P_\mu| \approx (\theta_0)^2/2$, we obtain a systematic uncertainty in $P_\mu\xi$ of 2×10^{-5}.

To estimate the systematic uncertainty due to the uncertainty in the beam size, the beam size outside the TEC is used since the multiple scattering makes the beam size inside the detector too large in the simulation. A plot of the predicted polarization versus beam size is shown in Fig. 6.4. The nominal RMS beam size is 0.55 cm at the stopping target, or 0.65 cm at the TEC. Since these beam sizes are roughly the same, we take the uncertainty in how well the TEC measures the beam size as the uncertainty in beam size. The resolution of the TEC is about 250 μm, resulting in a systematic uncertainty in $P_\mu\xi$ due to beam size of 0.35×10^{-3}.

6.1.4 Muon Depolarization at the Stopping Location (MDSL)

This section will introduce physics mechanisms that could result in muon depolarization due to interactions in material. The systematic uncertainty due to muon depolarization in gas or Al stopping target is then estimated as the uncertainty due to the extrapolation of a time dependent depolarization to zero decay time. This estimate assumes there is no unobservable depolarization on a time scale < 250 ns.

MDSL: Mechanisms for Muon Depolarization in Materials

Down to about 30 keV the energy loss of muons is mainly due to ionization of atoms along the path of the muon which does not depolarize the muons. Below 30 keV, the thermalization of muons depends strongly on the material. In nonmetals, the muons can be captured to form a bound state of a muon and an electron (muonium, written chemically as Mu), which can undergo spin exchange with the electron resulting in depolarization of the muons. In metals there is no Mu formation. Muons in metals will either stop at an interstitial site between metal atoms, or very rarely take the place of an impurity in the metal lattice. The conduction electrons, whose spins should align with the magnetic field of the TWIST solenoid act to screen the muon from Mu formation [63].

At the 99% level, there is no depolarization in a high purity metal target if there is a huge holding field such as we have in TWIST. However at the 99.9% level this is less certain. The muon creates a quasifree state in Al where conduction electron concentration is $\simeq 2 \times 10^{23}$ cm^{-3}. The polarized muon state is not stable because the energy difference between the parallel and anti-parallel spin states of a muon in a 2 T magnetic field is $\simeq 10^{-6}$ eV while the thermal energy at $T = 300$ K is $kT \simeq 3 \times 10^{-2}$ eV. Muon spin relaxation can only occur by interaction with the conduction electrons, nuclear moments of the Al, or with paramagnetic impurities in the metal. This section will present an analysis of the possible relaxation time dependence due to these interactions.

Interactions of the muon spin with conductive electrons is called Korringa relaxation [64]. Conduction electrons create a large hyperfine magnetic field at the site of the muon which can be considered as a fluctuating local field with a correlation time $\tau_c \simeq 10^{-13}$ s in Al [65]. This short correlation time results in a relaxation rate that has an exponential form. The Korringa relaxation rate does not depend on the magnetic field. Significant relaxation rates of $\lambda > 0.001 \mu s^{-1}$ have been measured for muons in Cd, Sn, Pb, As, Sb, and Bi [66]. The authors explained the measured relaxation rates to be due to Korringa relaxation since the λ values increase with temperature as predicted. In our Al target with a longitudinal field $H_L = 2$ T, the muon relaxation rate was measured to be $\lambda = 0.00155$ μs^{-1}. This relaxation rate is most likely to be due to Korringa relaxation (exponential).

Nuclear dipole moments of Al produce magnetic fields, H_d, of few gauss on a muon fixed in a crystal cell. According to many μ^+SR references the dipole-dipole interactions cause muon spin relaxation rates of $\lambda_d = 0.1$ to 0.3 μs^{-1} in an orthogonal magnetic field. A longitudinal field, H_L, decreases the amplitude of the relaxation by the factor $(H_d/H_L)^2$ [67]. The reduction of the relaxation rate at $H_L = 2$ T is on the order of $< 10^{-6}$. The above is correct for a muon fixed in a crystal cell. Diffusion of the muon creates a magnetic field

on the muon which varies in both space and time. As a result, the muon relaxation rate decreases and becomes exponential.

Our high purity Al stopping target has the following impurities in ppm: Cu 0.3, Fe 0.3, Mg 1.2, and Si 0.8. Iron is the only paramagnetic impurity that can cause a relaxation. It is unlikely that this can cause much depolarization because we have only one Fe atom for every 3×10^6 atoms of Al. Hence the probability for a muon to reach an Fe atom is very low. If a muon does reach the vicinity of an iron atom, then the magnetic moment from the Fe atom creates a magnetic field $H_e \simeq 1$ kG at a distance of one Al lattice cell period ($\simeq 4$ Å). This magnetic field corresponds to a muon Larmor precession with frequency of $\omega_0 \simeq 10^8$ s^{-1}. The interaction causes a very fast muon relaxation if the muon is fixed near the Fe and the Fe electron spin is also fixed. The electron spin of an iron impurity in Al fluctuates with time $\tau_c < 10^{-10}$ s[68]. The fluctuations decrease the relaxation rate, and the relaxation dependence becomes exponential when $\omega_0 \cdot \tau_c \ll 1$ [67]. We have $\omega_0 \cdot \tau_c \simeq 10^{-2}$, therefore this unlikely interaction with an iron impurity causes an exponential relaxation. A relaxation rate of $\sigma \simeq 0.02$ μs^{-1} has been obtained in Al at $T > 100$ K with Fe admixture of 10 ppm by Hartmann *et al.* [69]. Our data also have $\sigma \simeq 0.02$ μs^{-1} when fitting to a Gaussian depolarization rate. The depolarization rate independence in Al due to the increased iron concentration in the Al of Hartmann is direct evidence that the measured muon relaxation rate is not due to the Fe impurity. The relaxation rate of Hartmann was measured in an orthogonal magnetic field. The rate independence from longitudinal versus orthogonal magnetic field up to $H_L = 2$ T is direct evidence of Korringa relaxation of the muon spin in Al.

High energy muons can create defects in matter. The paramagnetic defects can produce significant magnetic fields on a stopped muon. The defect in the electron configuration recovers in $\sim 10^{-11}$ s in metals [70]. The fast recovery can only cause a fast muon relaxation. A muon can also displace atoms in a crystal cell. The displaced atom configuration changes very slowly. The average distance between a stopped muon and the last displaced atom in graphite, for example, is 9000 Å [71]. The effect of this interaction on the muon relaxation rate is negligible.

In summary the only practical form for muon spin relaxation in our high purity Al target is Exponential; the dominant process being Korringa relaxation by interaction of the muon with conduction electrons.

MDSL: Materials in the Vicinity of the Muon Stopping Target

In the *TWIST* analysis, muons with a hit in PC6 and not in PC7 are considered to have stopped in the stopping target. While this is often the case, we can use our GEANT simulation to study how often the muons stop in other materials near the stopping target (proportional chambers PC5 to PC8.) The proportional chambers consist of: aluminized Mylar foils (or 99.99% purity Al between PC6 and PC7), CF4/i-C4H10 gas, and Gold plated Tungsten wires. A plot from a simulation of where the muon stops versus z coordinate reveals the fraction of muons stopping in different materials. We label the muon stopping fractions as f_j^i, where i=5,6,7 labels the selection of last proportional chamber hit by the muon, and

j=Metal(m), Other(o), Gas(g), Plastic(p) labels the material. Figure 6.5 shows the simulated distribution in z of muons stopping in the chambers around the stopping target.

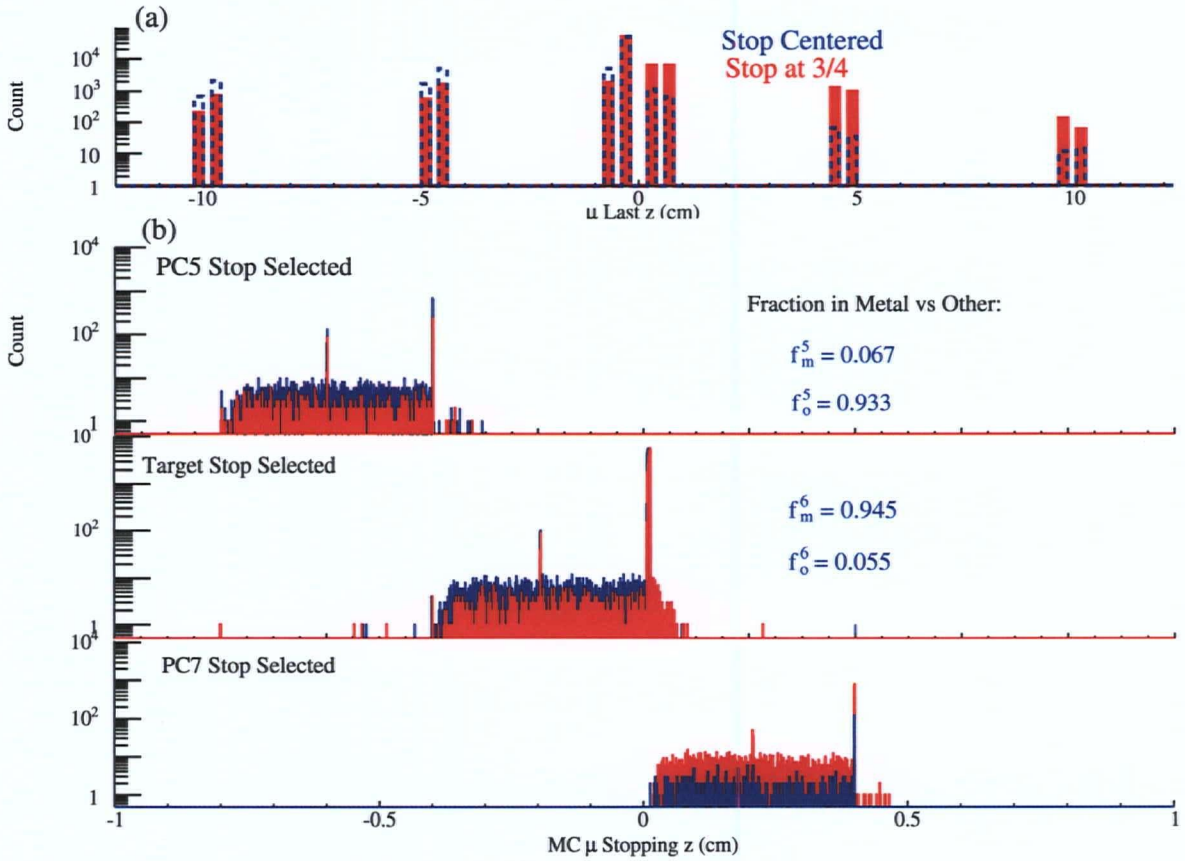

Figure 6.5: (a) The simulated distribution in z coordinate of muons stopping in chambers around the muon stopping target. (b) Expanded view of the muon stopping z coordinate for selection of PC5, PC6 and PC7 as the last plane hit by the muon. The last hit in PC5 is at top, PC6 is in the middle, and PC7 is at bottom. In both (a) and (b) muons with the Bragg peak centered in the muon stopping target are shown in blue, and those stopping at 3/4 are shown in red.

By knowing the fraction of muons stopping in each material and measuring P_μ from the muon decay spectrum from different selections of the muon's last plane hit, we can estimate the level of this effect. The fraction of muons stopping in different materials depends on where the muon Bragg peak is centered. The stopping fraction in different materials when the muon's last hit occurred in PC 6 is shown in Figure 6.6. The fraction stopping is plotted versus the mean muon stopping position.

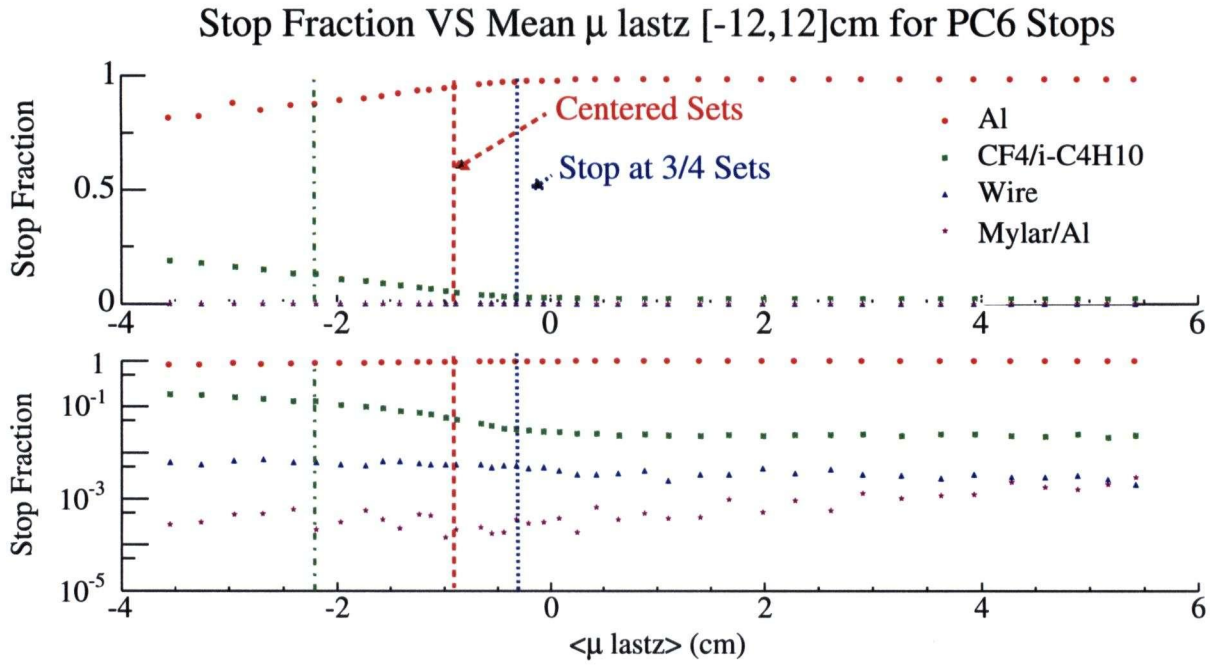

Figure 6.6: Fraction of muons stopping in aluminum (Al), gold plated tungsten wire, CF4/i-C4H10, and aluminized Mylar foil for muons with last plane hit in PC6, versus the mean muon stopping z coordinate between -12 cm and 12 cm from the last plane hit information. The mean muon stopping z coordinate for: data set 32 is shown as a green line, data sets with the Bragg peak centered as a red line, and the data sets stopping at 3/4 as a blue line.

MDSL: Estimate from Extrapolation Error

A decay-time dependency of the depolarization was observed for muons stopping in an Al target. Plots of the polarization estimate from an asymmetry analysis of the 2004 data and simulation are shown in Figure 6.7. A Gaussian depolarization with a sigma of 54.4 μs was included in the simulation to match the observed depolarization in 2004 data. A Gaussian form was chosen before it was decided that only an exponential form was possible. The difference in shape between a Gaussian and and exponential for decay times from 1050 ns to 9000 ns is indistinguishable at the level of statistics used in this measurement. Note that the average spin from muon stops is known exactly in the simulation so this error can be corrected.

The depolarization rate cannot be explained solely by muons that stop in gas rather than in Al. Models for depolarization in metal are either of an exponential or Gaussian form. However, calculations shown earlier in this section imply that the only practical form is an exponential shape in Al since the effects of the other models are very small.

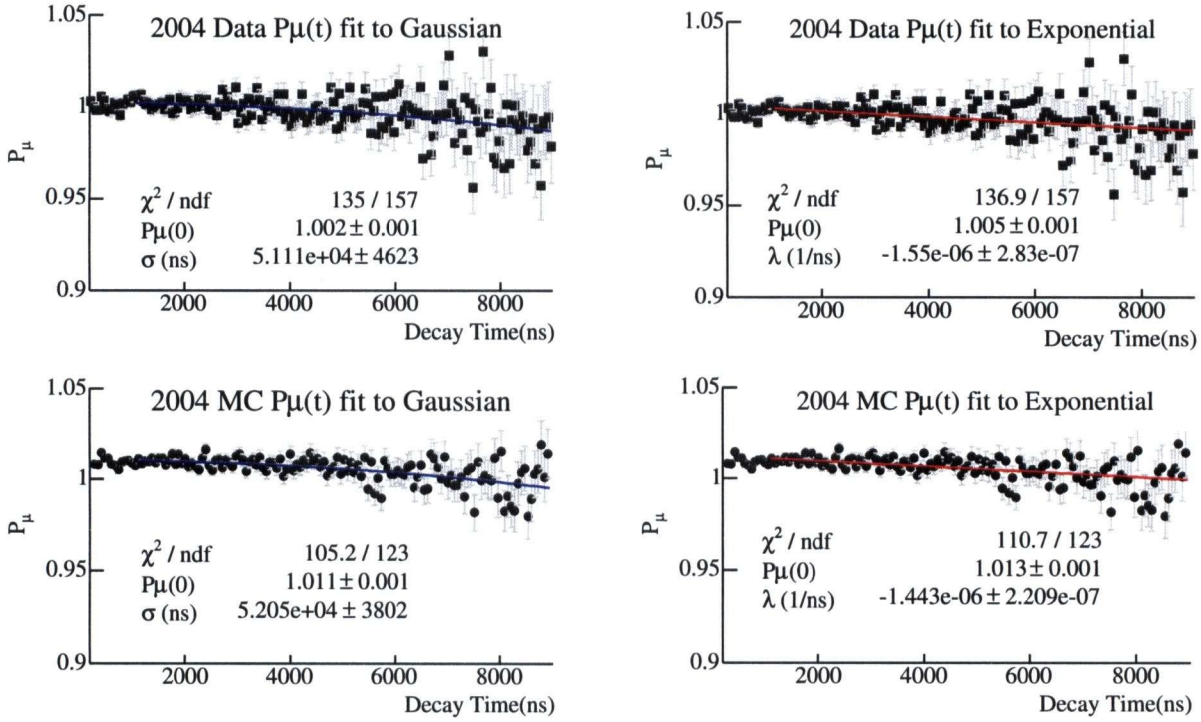

Figure 6.7: Polarization estimate from an asymmetry analysis of the 2004 data at the top, and 2004 simulation at the bottom. The distributions are fit to a Gaussian on the left and to an exponential on the right. The fit excludes decay positrons before a decay time of 1050 ns to avoid the potential bias from extra muon hits in the upstream decay positrons.

Jodidio *et al.*, measured a depolarization rate of $(-0.43 \pm 0.34) \times 10^{-3}$ μsec^{-1} for their Al target at 1.1 T [14]. This rate is about 3.5 times smaller than the $(-1.55 \pm 0.28) \times 10^{-3}$ μs^{-1} for our muon stops. The difference in rate is attributed to the 2.5 to 5.5% of the muons that stop in the gas before our stopping target. Attempts were made to determine separate slopes for our Al and gas depolarizations, but this did not work well because the method was too sensitive to the exact shape of the stopping distribution. Since about 2/3 of our depolarization must come from the gas stops it is uncertain whether the shape of the depolarization is Gaussian or exponential.

The difference between the two model extrapolations is 2.3×10^{-3}. Half of the difference is the *correction* applied to simulation to data fits, since the simulation was generated with a Gaussian form, while in reality the shape is most likely something between Gaussian and exponential. An estimate of the extrapolation uncertainty is $\sqrt{2}$ times the extrapolation uncertainty, since the final fits were to distributions from simulation which have equal statistics

to the data. The uncertainty in $P_\mu \xi$ due to extrapolation is: $\pm\sqrt{2}(0.001) = \pm 1.4 \times 10^{-3}$. The sign of the correction reduces the simulation polarization, so that the correction is a positive shift in data to simulation differences in $P_\mu \xi$. To better illustrate the sign of the correction the depolarization versus decay time in data and simulation with the different models is shown in Figure 6.8.

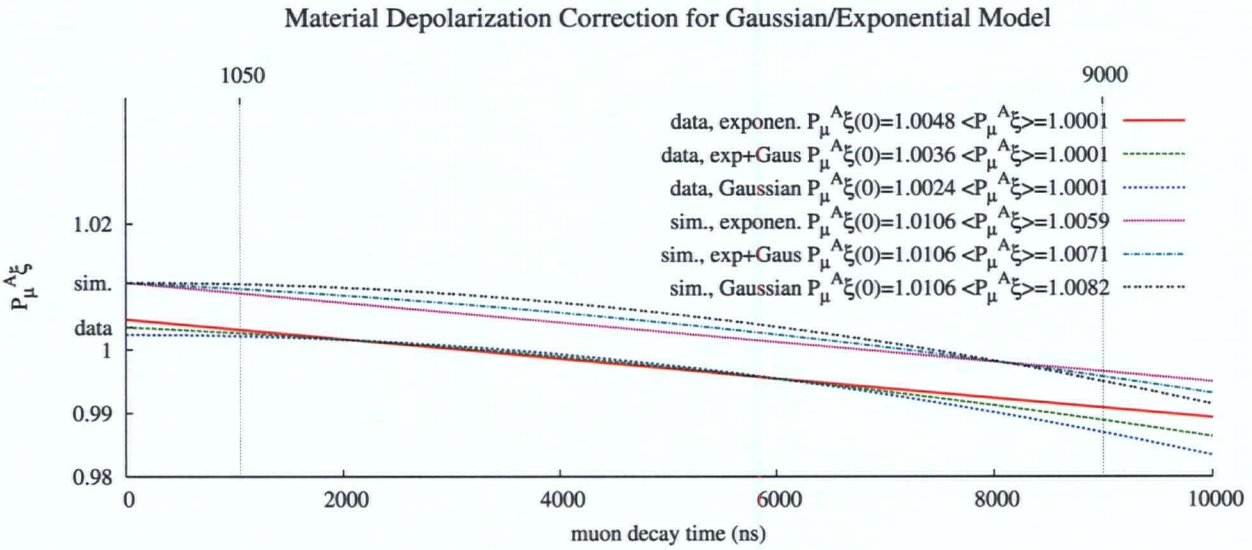

Figure 6.8: Depolarization versus decay time for exponential and Gaussian model functions used in the asymmetry analysis. The fit parameters from data are used for all of the slopes, and the fit values from data and simulation are used for the polarization at zero time. For the simulation, the zero time polarization was taken from the fit to a Gaussian distribution, since that is how the simulation was generated. Notice that the data will be either Gaussian, exponential or something in-between; but, fitting data to simulation, the average polarization for an exponential in simulation, between 1050 ns and 9000 ns, is lower than the polarization for a Gaussian by 0.00023. Thus the sign of the correction reduces the simulation polarization, so that the correction is a positive shift in data to simulation differences in $P_\mu \xi$.

6.1.5 Background Muon Contamination

Another contribution to the depolarization is contamination from "background" muons. Strong evidence for muons with a different polarization, and longer range than surface muons, is found in the 2002 data set with muons stopped further upstream than the nominal target position. In this set, a reduced polarization is observed for those muons whose last hit was in PC7 or PC8.

It is expected that nearly all of the surface muons will stop by the end of the target module. Stops observed further downstream than PC7 and PC8 have a probability, increasing with plane number, of being due to the "background" muons. An estimate for the background muon contamination is made in the following way. The data were modeled in GEANT as a combination of a standard GEANT run with polarized surface muons, and a special run with muons arising from 29.6 MeV/c pion decays in the M13 channel and beam package area upstream of the TWIST chambers. Figure 6.9 shows the distributions of muon last plane hit for data and simulation before and after adding pions to the beam.

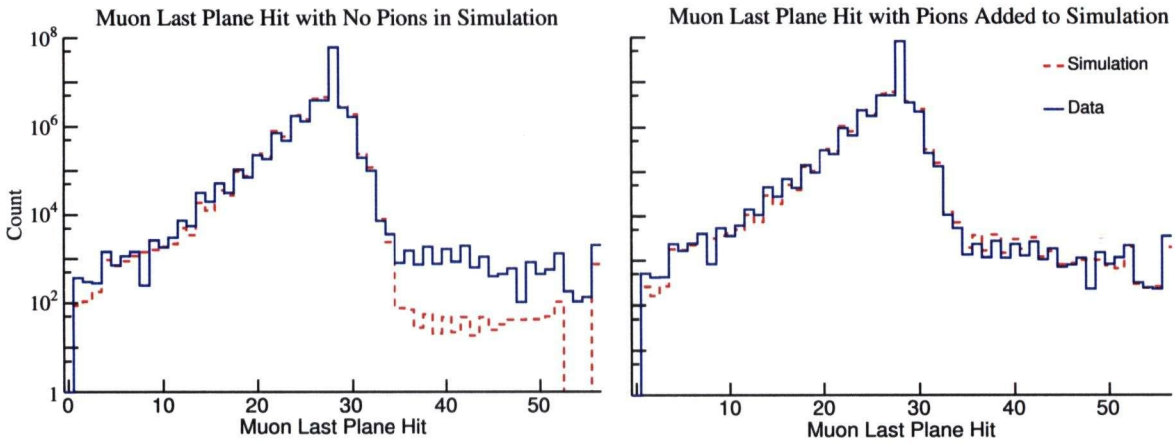

Figure 6.9: Overlay of the data set 35 and matching simulation last plane hit histogram before adding muon stops from pions in the beam on the left. The same histograms, but with pions added at to the simulation to match the data is shown on the right.

The fraction of muon stops due to the pions, relative to surface muons, is summarized for the 2002, 2003, and 2004 data in Table 6.5. The maximum polarization change is calculated for the case where the background muons have polarization opposite to surface muons. These estimates show that the systematic uncertainty in $P_\mu \xi$ due to background muons in the 2003 and 2004 data is less than ± 0.00018.

6.1.6 Beam Intensity and Coincident Accidental Particles

To estimate a systematic uncertainty in $P_\mu \xi$ due to beam rate and coincident particles, the 2002 data was used. A spectrum fit of low rate data, with a muon rate of 1.18 kHz, to high

Data Type	f_{PC5}	f_{target}	f_{PC7}	$\max \Delta P_\mu$
2002 Nominal (Set 2)	0.009106	0.000364	0.000669	0.00072
2002 Upstream (Set 4)	0.009027	0.002793	0.012078	0.00240
2003 Nominal (Set 14)	0.000134	0.000013	0.000040	0.00003
2004 Nominal (Set 35)	0.001110	0.000088	0.000798	0.00018

Table 6.5: Fractions of background muons relative to surface muons for muons stopping in PC5, the target, and PC7. For the target stops, the maximum effect on the polarization is estimated.

rate data, with a muon rate of 4.7 kHz, yielded a sensitivity in $P_\mu \xi$ of $(-3.0 \pm 1.7) \times 10^{-3}$.

For the 2004 data sets the rate was about 3 kHz. The largest RMS beam rate was 215Hz from data set 37. Although accidentals have a quadratic dependence, the rate of accidentals in coincidence with a trigger has a linear dependence. The scaling of the sensitivity is also assumed to be linear. The scale factor is the ratio of the changes in beam rate: $\frac{3.5}{0.215} = 16.3$. The systematic uncertainty in $P_\mu \xi$ due to beam intensity is therefore 0.18×10^{-3}.

6.1.7 Proton Beam Stability

The effect of muon beam movement, as the proton beam on the production target was moved, was also considered. The result is that $<dy_\mu>/dy_p \approx 0.25$, and $<dx_\mu>/dx_p \approx 0.5$. Movement of the proton beam by ± 1 mm resulted in a change in the muon beam angle $<dx>$ of 0.2 mrad, and the change in $<dy>$ of 1.3 mrad

Monitoring of the proton beam position is done using low intensity proton target scans, where about 1 μA of proton beam is steered both vertically and horizontally. Vertical steering of the protons is done with steering magnet labeled 1ASM4 (SM4), and horizontal steering with 1ASM5 (SM5). The calibration of the movement of the beam is with "protect monitor" plates located 2.5 mm to either side of the nominal proton beam path. The setting of these steering magnets is monitored in our slow controls. The variation in position of the proton beam over the production data taking period estimated from these history plots is 0.25 mm vertically and 0.1 mm horizontally.

From these numbers, the maximum movement of the muon beam due to proton beam movements is 0.063 mm vertically and 0.025 mm horizontally. The change in angle of the muon beam due to the movement of the proton beam is within 0.08 mrad vertically and 0.01 mrad horizontally. The final result is that the systematic uncertainty in $P_\mu \xi$ due to the proton beam stability is $\pm 0.02 \times 10^{-3}$.

6.2 Systematic Uncertainty Due to Chamber Response

This section describes the systematic uncertainty due to the drift and proportional chamber response. Six sources are considered: time variations in the wire to wire timing (t_0 variations), changes to the space to time relations (STR) from density variations, foil bulge due to changes in differential pressure between the chamber gas and cradle helium, the asymmetry of the wire positions relative to the foils due to construction, dead zone due to a recovery time after a muon passes through the chambers, and a difference in the upstream versus downstream chamber efficiency.

Two other effects that were considered, but not included in the final estimate of the systematic uncertainty were a corner of the cell drift time uncertainty, and cross talk removal. They were not included because they were measured to be negligible, or would introduce double counting.

6.2.1 Wire to Wire Time Variations

To estimate the possible time variation in the wire to wire time zero, calibration runs were taken at the beginning and end of the run period. The beginning and end calibration runs were taken with the magnetic field off, with a single trigger. From these calibration runs two different calibration files were made. The end of run time calibration run was done after a disaster that disabled half of the chambers. For the end of run calibration file, the times for the missing planes used times from a different beginning of the run time calibration.

To measure the sensitivity of the muon decay parameters to t_0 variations, a calibration file scaled by ten times the difference in the beginning and end of run time calibrations was used. The large changes in time calibrations caused the helix track fits have much worse χ^2. The change in $P_\mu\xi$ obtained from fitting the exaggerated time shift analysis spectrum to a normal analysis spectrum was $(8.9 \pm 0.9)\times10^{-3}$. The resulting systematic uncertainty is 0.89×10^{-3}. A second sensitivity, with a calibration file scaled by 5 times the difference in beginning and end of run, showed that this systematic uncertainty scales linearly.

6.2.2 Chamber Foil Bulge

The shape of the chamber cathode foils depends on the differential pressure between the chamber gas and the He gas of the cradle holding all of the chambers. The differential pressure of the chambers was monitored and controlled by the gas system. To measure the level of foil bulge, several nominal data runs were taken at different differential pressures. The average helix fit drift time difference, for tracks that go through the center of the chambers, relative to the average helix fit drift times for tracks that go through the radially distant part of the chamber, was found to be sensitive to the foil bulge. Run to run monitoring of this fit time difference shows that the variation in foil bulge was controlled to better than 50 μm.

To measure the sensitivity of the muon decay parameters to the chamber foil bulge, a simulation set was generated with the STR calibration changed as if the foils were moved outward by 500 μm. A fit of the decay positron spectrum from this exaggerated bulge to a nominal decay positron spectrum yielded a change in $P_\mu\xi$ of $(2.2 \pm 1.4) \times 10^{-3}$. The systematic uncertainty, in $P_\mu\xi$, due to time variations in the foil bulge, is estimated to be 0.22×10^{-3}.

6.2.3 Chamber Cell Asymmetry

Surveys of the constructed chambers show that the spacing between the wire plane and cathode foils was not the same on both sides of the wire. On average the cathodes were found to be shifted by about 150 μm from their nominal 2 mm spacing from the wire planes. With the solenoid field on, the position of the cathode foils was also determined using normal decay positron data. Using the bulge calibration data, from runs with different bulges, a relationship between a fit time difference to a foil shift was obtained. The time difference, used for the cathode foil position estimate, was the difference between the average helix fit time in one half of the chamber cell to the average time in the other half of the chamber cell.

To investigate the effect of these cathode foil shifts, the foil shifts *measured in software* were simulated. STR files were changed half plane by half plane to match the measured shifts. A fit of the muon decay distribution from the shifted cathode foil simulation set to a simulation set with symmetric planes gave a change in $P_\mu\xi$ of $(-0.2 \pm 1.4) \times 10^{-3}$. Since this shift of the cathode foils is thought to match the real detector, there is no scaling of this sensitivity. The sensitivity is used as the systematic uncertainty.

6.2.4 Density Variations

History plots of the density variation for each 2004 data set show that the largest RMS change in density was $\pm 0.7\%$ from data set 38. To estimate the effect of density changes, a simulation was generated with the temperature changed by 10% (from 300 K to 270 K), providing a scaling factor of 14.3. The muon stopping distribution was not adjusted to compensate for the change in density, so there is some double counting. Since this systematic uncertainty is small, the stopping distribution contribution was not included. A fit of the changed temperature simulation set to a nominal simulation set gave a change in $P_\mu\xi$ of $(2.4 \pm 1.4) \times 10^{-3}$ which translates to a systematic uncertainty of 0.17×10^{-3}.

6.2.5 Muon Dead Zone

As the muon passes through the upstream half of the detector, before coming to a stop in the stopping target, it deposits large ionization in the chambers. The resulting electron avalanches near the wires take time to recover as the positive ions drift back to the cathode planes. These dead zones only affect decay positrons that go upstream and pass near where the muon made hits in the chambers. The muon deadzone therefore causes an upstream-downstream efficiency difference for decay positrons. The dead zone was measured

by projecting helical fits to the decay positrons back to a wire that had a muon hit. For each muon hit the wire efficiency versus distance away from the muon hit is estimated as a function of time after the muon track. The dead zone measured in the data had a lifetime of 3 μs, and its size was 0.056 cm for the DCs and 0.146 cm for the PCs.

A measurement of the muon decay parameter sensitivities to the muon dead zone was made by introducing a dead zone, with $\sigma = 5$ cm, and exponential lifetime of 3 μs, for both the PCs and DCs. A fit of the decay positron spectrum from the exaggerated dead zone simulation to a spectrum from a simulation run with no dead zone yielded a change in $P_\mu \xi$ of $(0.2 \pm 1.4) \times 10^{-3}$.

To determine the scaling of the sensitivity, a small statistics simulation with the dead zone as measured in data was done to count the number of decay positron hits removed by the dead zone. The number of hits removed from the exaggerated dead zone simulation was also counted, and the estimate of the scaling was the ratio of the hits in each of these runs. The resulting scaling factor was: 11.7 for the PC where the muon stops, 25.8 for the DCs, and 47.6 for the far upstream PCs. A conservative estimate of the systematic uncertainty, in $P_\mu \xi$, due to the muon dead zone, is 0.01×10^{-3} using the scaling factor of 11.7.

6.2.6 Upstream versus Downstream Efficiency

The difference in the average number of degrees of freedom in the track fits in the upstream versus downstream directions, for tracks with the same energy and angle, is used to estimate an upstream versus downstream efficiency difference. The difference between the upstream and downstream average number of degrees of freedom, in data versus simulation, is 0.18. The average data and simulation degrees of freedom, for different decay positron momenta and angle, are shown in Figure 6.10.

To estimate the sensitivity of the muon decay parameters, due to a difference in upstream versus downstream efficiency, a data set was analyzed with 5% of its downstream DC hits thrown away at the unpacking stage of the analysis. This upstream downstream inefficiency change, compared to a normal analysis of the same data, gave a sensitivity of $(1.9 \pm 0.9) \times 10^{-3}$, where the error in the sensitivity was rescaled, since the fit was correlated.

The lowered efficiency run has about 1.8 NDOF less downstream compared to the standard run. Given that the difference between simulation and data is 0.18 NDOF the scaling of the sensitivity is 10; the systematic uncertainty in $P_\mu \xi$ due to the difference in upstream and downstream efficiency is ergo 0.2×10^{-3}.

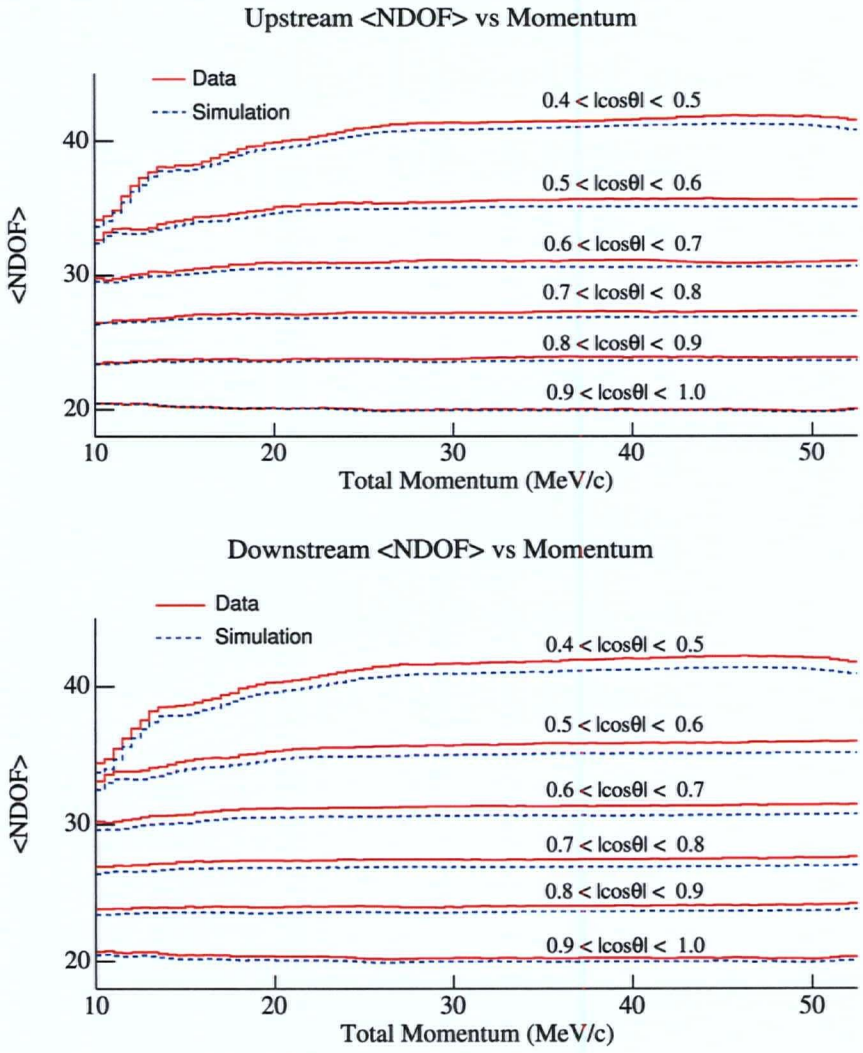

Figure 6.10: Mean helix fit number of degrees of freedom (NDOF) versus momentum for different ranges of $\cos\theta$. The blue dashed line of each $\cos\theta$ range is from simulation, and the and the red solid line is the data. The distributions for upstream decays are shown in the top plots, and the downstream decays are shown in the bottom plots.

6.3 Systematic Uncertainty Due to Momentum Calibration

The systematic uncertainty in the momentum calibration comes from two contributions. One contribution is due to how well we can do our endpoint energy calibration. The other factor is how well our measured magnetic field map represents reality.

6.3.1 Endpoint Fits

The method of doing endpoint fits to obtain a momentum calibration is presented in Section 3.6. The sensitivity to the momentum calibration is measured by fitting a decay positron spectrum that has the momentum calibration properly applied to a spectrum where one of the energy calibration parameters (α_u, α_d, or β) was shifted by 100 keV/c. When measuring the sensitivity to β, the values of α_u and α_d were changed to follow the correlation observed in Figure 3.6.2.

With the end point β fixed to zero, the uncertainty σ_i for β is obtained from the discrepancy of 2 G in 20000 G in the shape of the field map in the tracking region. This gives an uncertainty at the endpoint momentum in β of 5.3 keV/c. Endpoint fits with β fixed have uncertainty in α of about 1 keV/c, as summarized in Section 3.6.2. The sensitivity, scaling factor, and systematic uncertainty contribution from each of the energy calibration parameters is summarized in Table 6.6. The resulting systematic uncertainty in $P_\mu\xi$ is 0.16×10^{-3}.

	Sensitivity		Scale	Systematic
Parameter	S_i value	S_i error	R_i/σ_i	Uncertainty
α_u	-15.75	0.08	100	0.16
α_d	0.649	0.004	100	0.01
β	-0.46	0.31	20	0.02
Total				0.16

Table 6.6: Energy calibration sensitivities and systematic uncertainties in units of $\times 10^{-3}$. The total is the quadrature sum of the individual systematic uncertainties.

6.3.2 Magnetic Field Map Accuracy

Inaccuracies in the magnetic field map lead to inaccuracies in the determination of the decay positron momentum. To quantify this effect, a modified magnetic field map was produced by distorting the standard field simulation as follows:

$$\Delta B_z = -(0.006 \text{ G/cm}^2)\, z^2 - (0.00004 \text{ G/cm}^3)\, z^3 - (1.25 \text{ G/cm})\, r. \qquad (6.6)$$

A nominal data set was analyzed with the distorted field map, and the resulting decay positron spectrum was fit to the standard analysis of the same data set. The resulting sensitivity to $P_\mu \xi$ was $(-0.9 \pm 1.6) \times 10^{-3}$.

The distorted field map differs from the nominal 2 T field map by up to 40 G at the extremes of the tracking volume. Differences between an Opera generated field map, and the measured field map are 2 G at the extremes of the tracking region. A conservative scaling factor of 10 gives a systematic uncertainty in $P_\mu \xi$ of 0.09×10^{-3}.

6.4 Systematic Uncertainty Due to Positron Interactions

The systematic uncertainty due to positron interactions includes four effects: a discrepancy between the simulation and data energy loss, hard and intermediate interactions, multiple scattering, and backscattering from material outside the detector. A systematic uncertainty due to the target thickness is described, but not included in the final table of systematic uncertainties because its contribution is negligible.

6.4.1 Energy Loss

The energy loss systematic effect has to do with an unexplained difference of 7 keV/c between our simulation and data energy loss at the endpoint momentum. This 7 keV/c difference was measured using a special data set, where muons were stopped upstream in the trigger scintillator, and the first four PCs. The decay positrons that went downstream through all of the DCs were then fit twice with our helix fitting code; once to the upstream half of the track, and once to the downstream half of the track. The difference in momentum between these two track fits is called Δp in this section.

The systematic uncertainty estimate comes from looking at the difference in slope, between data and simulation, in $(\Delta p)\cos\theta$ versus p as shown in Figure 6.11. The difference in slope is (7 keV/c)/(50 MeV/c) $= 1.4 \times 10^{-4}$.

To obtain the sensitivity to the difference in the slope, defined as α_1 in Section 3.6, an energy calibration with $\alpha_1 = 0.014$ was performed, giving a scaling factor of 100. The sensitivity after rescaling the error, since the fit was correlated, was $(0.64 \pm 0.20) \times 10^{-3}$. The resulting systematic uncertainty in $P_\mu\xi$ is 0.01×10^{-3}.

6.4.2 Hard and Intermediate Interactions

One of the positron interaction systematic uncertainties has to do with how well we can validate the simulation of hard and intermediate interactions. Hard interaction events are arbitrarily defined here to be events in which the decay positron loses more than 1 MeV/c of momentum from where it is generated to where it goes through the last DC. Intermediate interactions are those events whose decay positrons have lost less than 1 MeV/c.

In simulation the ratio of the reconstructed decay positron distribution, to the thrown distribution, shows how large a correction factor is needed to account for hard and intermediate interactions. The ratio of of reconstructed over thrown distributions in $\cos\theta$: for all events, events that lose < 1 MeV/c, and those events that lose > 1 MeV/c is shown in Figure 6.12.

Muon decay spectrum fits of the reconstructed to thrown distributions for all events, and for events that lose less than < 1 MeV/c were done to estimate the size of the correction. Plots of the change in $P_\mu\xi$ are shown in Figure 6.13. Note that the sign needs to be flipped for the systematic, because of the order in which the fit was done.

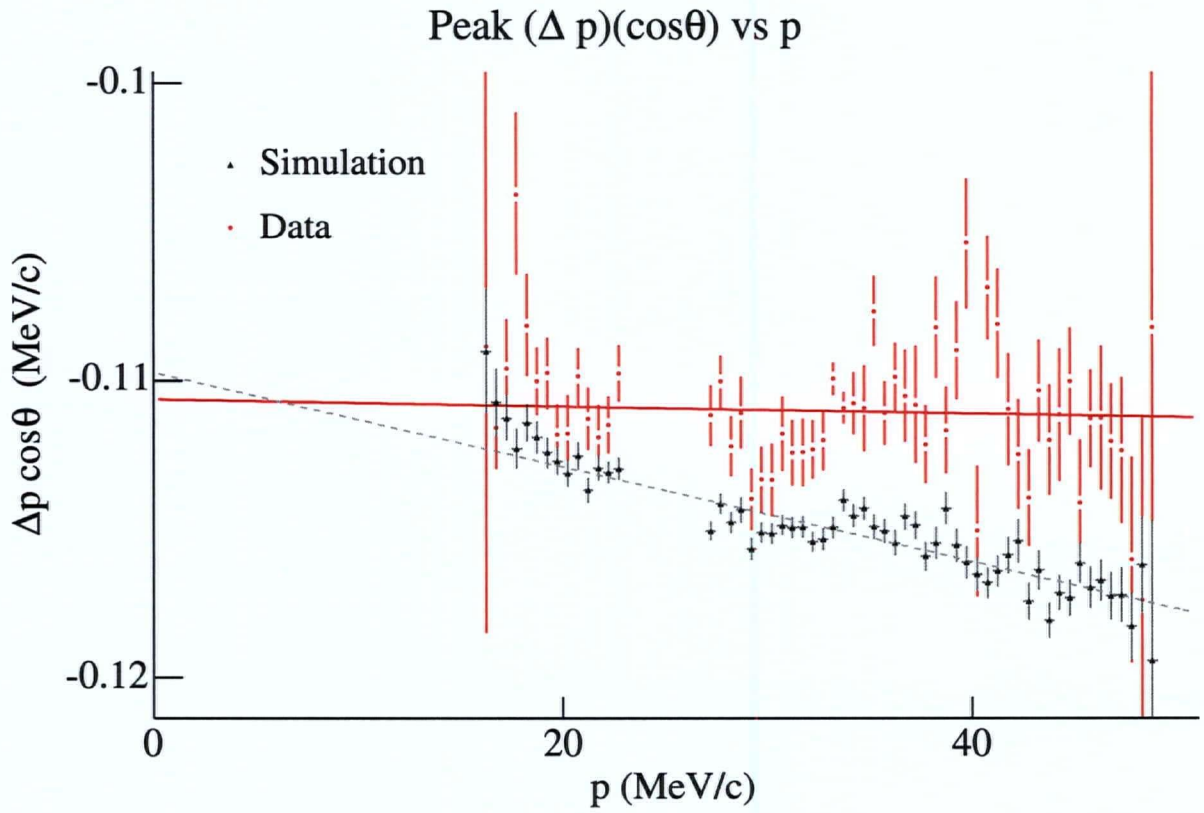

Figure 6.11: Comparison of $\Delta p \cos\theta$ versus p in Data and simulation. Δp comes from the difference in upstream and downstream fits to positrons from a data set with muon stopping upstream in the trigger scintillator and PCs.

Fits of the decay positron spectrum for hard interaction events, to the spectrum for all thrown events, failed because the shape of the distribution of hard interaction events was too different from that of the muon decay spectrum shape. An estimate the hard interaction contribution to the systematic uncertainty is the difference between fits to all events, and fits to intermediate interaction events. Since this estimate is not very robust, a different method for obtaining the final systematic uncertainty is described near the end of this section. The size of the corrections from the spectrum fit results are listed in Table 6.7 for $P_\mu \xi$. The size of the correction depends on the location of the muon stopping Bragg peak in the stopping target.

The hard interaction systematic uncertainty is estimated using a fit of a nominal simulation set, to an simulation set where the cross section for Bremsstrahlung was increased by ten times. In this fit, the difference in $P_\mu \xi$ was $(17.9 \pm 1.4) \times 10^{-3}$. Using the 5% discrepancy in hard interactions, estimated in Section 5.7, the the scaling factor for this sensitivity is $10/0.05 = 200$. This gives an estimate of $(0.09 \pm 0.01) \times 10^{-3}$ for the systematic uncertainty in $P_\mu \xi$ due to hard interactions.

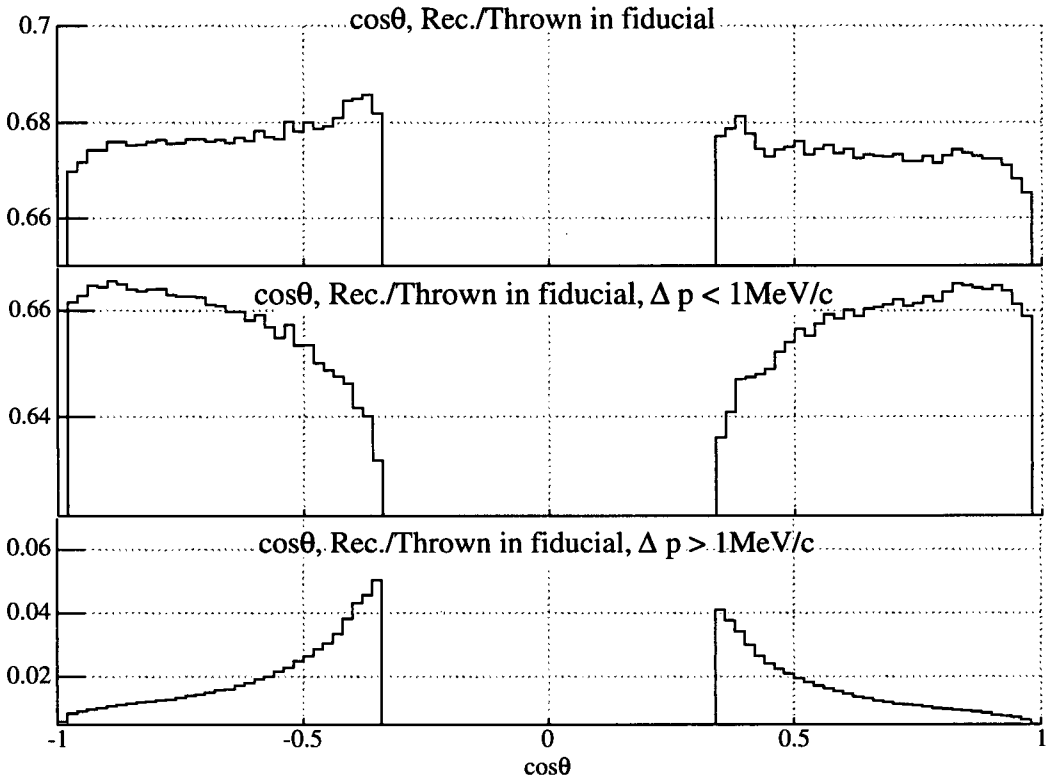

Figure 6.12: Reconstructed over thrown yield versus $\cos\theta$ for events in the fiducial $p_{total} < 50.0$ MeV/c, $p_\perp < 38.6$ MeV/c, and $p_z > 13.7$ MeV/c. The top plot is for all events, the middle plot is for events where the decay positron loses less than 1 MeV/c, and the bottom plot is for positron energy loss greater than 1 MeV/c. The plots are for a muon stopping distribution centered in the target.

Given that our simulation is validated to 5% for intermediate interactions, and using a systematic uncertainty in hard interactions of 0.00009, we obtain a systematic uncertainty in $P_\mu\xi$ of:

$$0.63 \times 10^{-3} \text{ for PC5 stops,}$$
$$0.35 \times 10^{-3} \text{ for centered stops, and}$$
$$0.12 \times 10^{-3} \text{ for stops at 3/4.}$$

An average systematic uncertainty in $P_\mu\xi$ weighted by the number of datasets with each stopping distribution is 0.29×10^{-3}. For plots and a description of the validation of our simulation refer to Section 5.7.

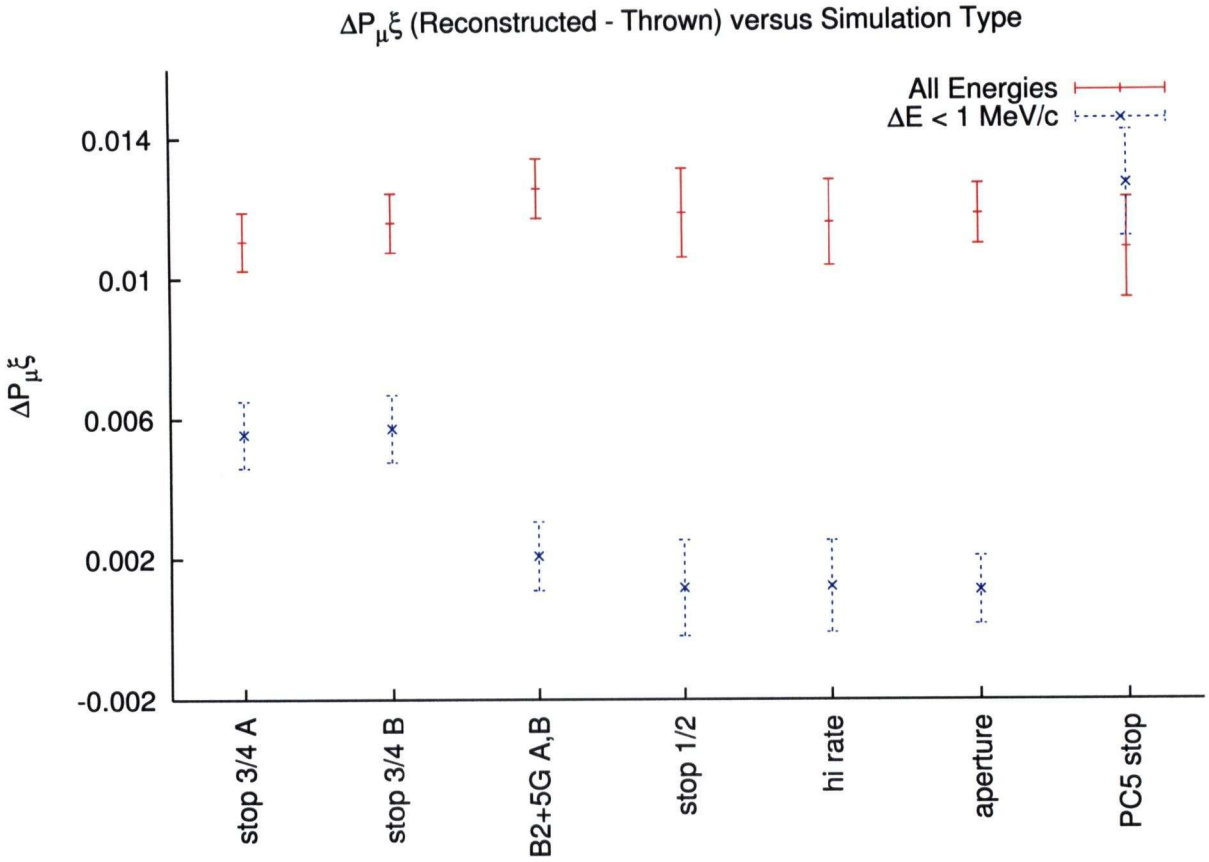

Figure 6.13: $\Delta P_\mu \xi$ from spectrum fits to distributions of $\cos\theta$ versus total momentum of reconstructed to thrown decay positron distributions. Michel fits to all events are shown as '+' and the fits to events with decay positrons that lose less than 1 MeV/c are shown as 'x'. Points 1 and 2 are for muons stopping centered, points 3 to 6 are stopping at three-quarters, and point 7 is for muons stopping further upstream.

6.4.3 Multiple Scattering

The sensitivity of $P_\mu \xi$ to multiple scattering was measured by smearing the reconstructed positron angle in the analysis of a standard simulation set. This smearing took the form:

$$\Delta\theta = \frac{k}{|\vec{p}|\sqrt{\cos\theta}}. \tag{6.7}$$

The resulting decay positron spectrum was fit to the unsmeared spectrum from the same simulation set yielding a sensitivity of $(-3.2 \pm 1.4) \times 10^{-3}$.

The inaccuracy in the simulation of multiple scattering is 0.7 mrad as described in Section 5.7. The constant k was chosen so that a typical 30 MeV/c momentum track at 45° had a $\Delta\theta$ of 30 mrad. The systematic uncertainty is -0.08×10^{-3}.

μ Location in Target	$\Delta P_\mu \xi$ Inter.	$\Delta P_\mu \xi$ Hard
PC 5 stops (upstream)	-0.0125	0.0015
centered ($\frac{1}{2}$)	-0.0068	-0.0037
$\frac{3}{4}$	-0.0015	-0.0105

Table 6.7: $\Delta\xi$ corrections due to intermediate and hard interactions for each of the three different muon stopping locations of data.

6.4.4 Material Outside the Detector

Materials outside the tracking volume acted as surfaces for the decay positrons to undergo a backscattering. In particular, components of the beam package were a source of deltas and backscatters caused by a decay positron. The systematic uncertainty due to such extra particles was calculated by collecting a set of data with additional material introduced downstream of the detector.

The spectrum from a data set with extra material was fit to a spectrum from a data set without the extra material yielding a change in $P_\mu\xi$ of $(1.2 \pm 2.0) \times 10^{-3}$. The extra material added was an 0.65 cm thick aluminum plate mounted on an 0.59 cm thick plastic plate about 80 cm downstream of the central stopping target. The effect is scaled by the ratio of extra particles due to the aluminum divided by the difference between data and simulation in nominal conditions.

$$\frac{R_i}{\sigma_i} = \frac{N_{Al}^{\text{Extra Particles}}}{|N_{\text{Data}}^{\text{Extra Particles}} - N_{\text{Simulation}}^{\text{Extra Particles}}|} = 60. \tag{6.8}$$

The resulting systematic uncertainty is 0.02×10^{-3}. Note that outside the nominal fiducial region differences between the simulation and data backscattering have been observed. The difference is predicted to be due to backscattering from the solenoid yoke which was not present in the production simulation. Plots showing the distribution of decay positron angle and energy for events identified as having a backscatter or beam positron correlated in time with the decay positron are shown in Figure 6.14.

6.4.5 Stopping Target Thickness

The muon stopping target is 71 ± 1 μm of high purity Al. The systematic effect, due to the 1 μm uncertainty, is approximated using a simulation generated with a 125 μm Mylar stopping target with graphite layers of 30 μm on each side. The resulting decay positron spectrum was fit to a spectrum created with 10 μm layers of graphite. Using the very rough approximation that the extra 40 μm of graphite is equivalent to 40 μm of Al, this corresponds to a scaling factor of 40. The resulting target thickness systematic uncertainty in $P_\mu\xi$ is $(0.02 \pm 0.03) \times 10^{-3}$.

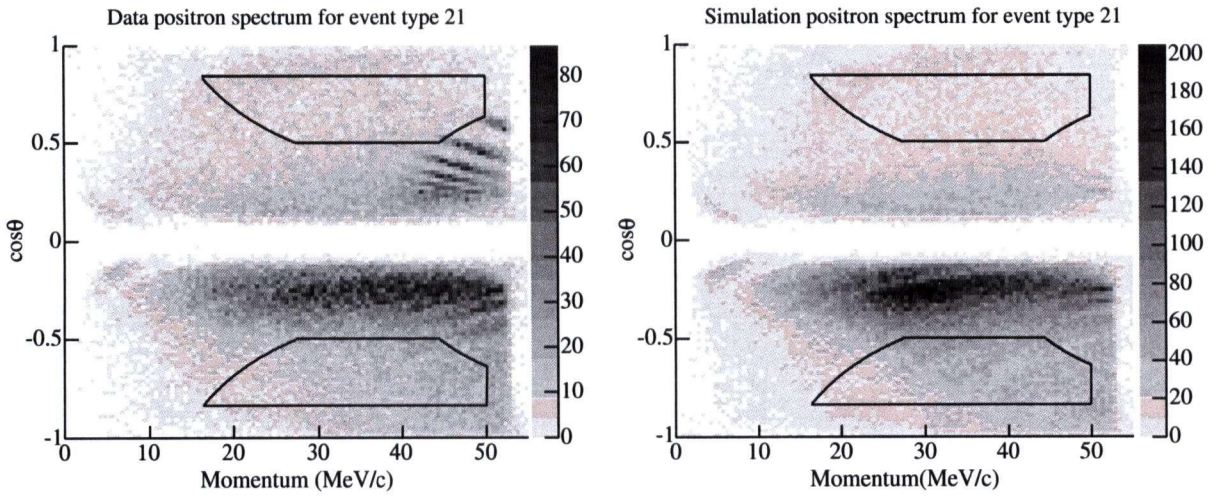

Figure 6.14: Distribution of decay positron $\cos\theta$ versus total momentum in MeV/c for events identified as having a backscatter or beam positron correlated in time with the decay positron. The left plot is from data, and the right plot is from simulation.

6.5 Systematic Uncertainty Due to Spectrometer Alignment

The following subsections describe and quantify the systematic uncertainties related to the spectrometer alignment. The systematic uncertainty due to spectrometer alignment comes from: how well the chamber translations in x, y, z and angle are corrected to match their true positions, and the degree to which the misalignment between the magnetic field axis to the chamber axis is treated.

6.5.1 Longitudinal Alignment

The alignment of the planes in z is by construction. The spacing of the chambers was precisely measured and controlled by the special Sital spacers. The precision of the chamber spacing is 30 μm longitudinally. To measure the sensitivity of the muon decay parameters to a longitudinal misalignment of the chambers, random offsets of ten times the chamber spacing precision were introduced in the analysis of a simulation set. The resulting systematic uncertainty in $P_\mu\xi$ is 0.22×10^{-3}.

6.5.2 Rotational Alignment

The rotational alignment systematic was found by analyzing a data set with an alignment file containing random rotational offsets 10 times the 0.01° precision of the rotational alignment corrections. The systematic uncertainty in $P_\mu\xi$ due to the rotational alignment is 0.22×10^{-3}.

6.5.3 Magnetic Field Alignment

The accuracy of the alignment of the magnetic field axis to the chamber axis is 0.02 mrad, but the mismatch between upstream and downstream is 0.1 mrad for the 2004 data.

To measure the sensitivity a misalignment of the magnetic field of 0.25 degrees (4.4 mrad) was introduced in the simulation. A fit of the reconstructed decay positron spectrum of the misaligned simulation to a nominal set gave a sensitivity of $(1.2 \pm 1.4) \times 10^{-3}$.

Using a scaling factor of 40 (4 mrad/0.1 mrad) for the 2004 data gives the systematic uncertainty in $P_\mu\xi$ of 0.03×10^{-3} due to the misalignment of the magnetic field.

6.5.4 Translational Alignment

The translational alignment systematic uncertainty was investigated by analyzing a nominal data set with an alignment file containing random translational offsets 28 times the 10 μm precision of the translational alignment corrections. The resulting muon decay spectrum fit yields a systematic uncertainty in $P_\mu\xi$ of $< 0.01 \times 10^{-3}$.

6.6 Set-Dependent Systematic Uncertainties

The set-dependent systematic uncertainties are summarized in this section. Several of the set to set variations were estimated in the relevant sections of this chapter. In several cases the value is the same for all sets, however those systematic uncertainties are independent set to set. Table 6.8 summarizes the set to set systematic uncertainties.

	Set							
Effect	30	31	32	35	36	37	38	39
Fringe field depolarization				3.3				
Depolarization at stopping location				1.4				
Background muons				0.18				
Beam intensity	0.04	0.05	0.06	0.17	0.08	0.18	0.04	0.05
T0 variations				0.89				
Foil bulges	0.22	0.33	0.40	0.20	0.26	0.24	0.33	0.24
Density	0.06	0.12	0.02	0.06	0.05	0.02	0.17	0.06
Hard and intermediate interactions	0.37	0.37	0.64	0.37	0.37	0.16	0.16	0.16
Total in quadrature	3.7	3.7	3.8	3.7	3.7	3.7	3.7	3.7

Table 6.8: Set-dependent systematic uncertainties for each effect and set in units of 10^{-3}. In several cases the value is the same for all sets; however those systematic uncertainties are independent set to set.

Part III

Results and Conclusion

Chapter 7

Results

7.1 Blind Fit Results

7.1.1 Blind Fit for $P_\mu \xi$

Our datasets alone appear to have no significant difference in polarization according to the asymmetry analysis and spectrum fits. The $\Delta P_\mu \xi$ value for fits of each 2004 data set to its respective simulation, where the fringe field depolarization was removed from the simulation, is shown in Figure 7.1.

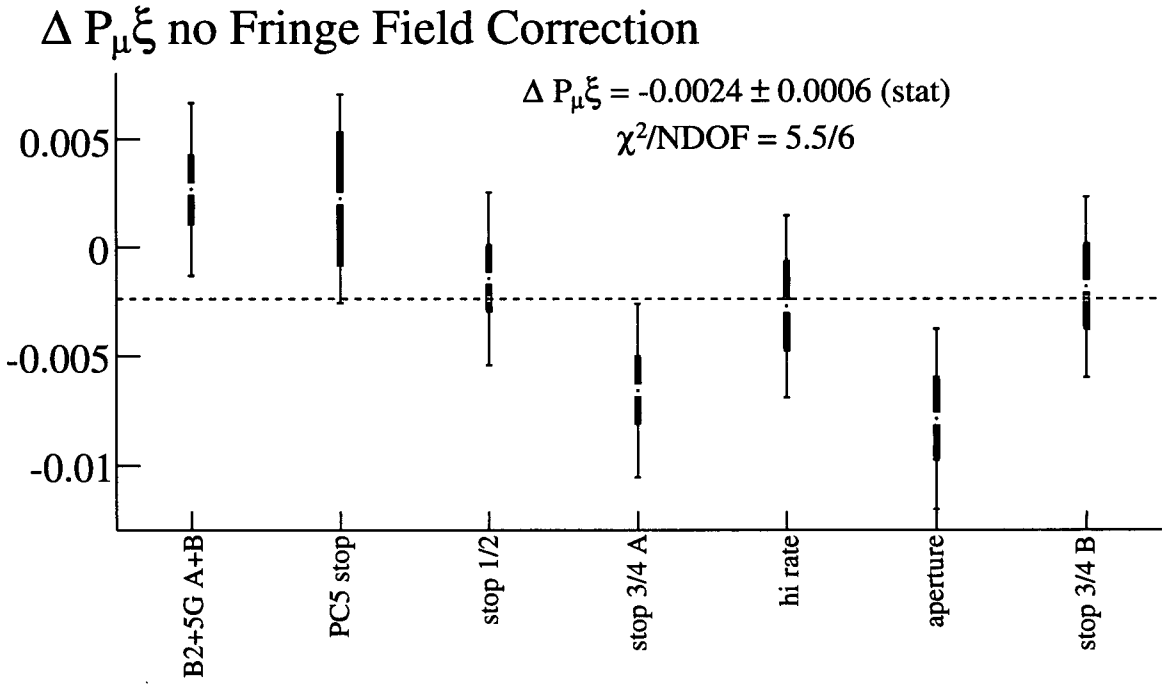

Figure 7.1: $\Delta P_\mu \xi$ from 2004 data to simulation spectrum fits with fringe field depolarization correction removed from the simulation. Statistical uncertainties are the thick red error bars, and the quadrature sum of statistical and set to set systematic uncertainties are the thin black error bars.

The difference in polarization obtained between the production simulation set with B2+5G and the production simulation set with an aperture inserted is 6.1×10^{-3}. The

consistency of the data, and difference in polarization of the simulation is one reason for the conservative estimate in the uncertainty in fringe field depolarization given in Section 6.1.3. The raw $\Delta P_\mu \xi$ values from simulation to data fits with the production simulation depolarization values are shown in Figure 7.2.

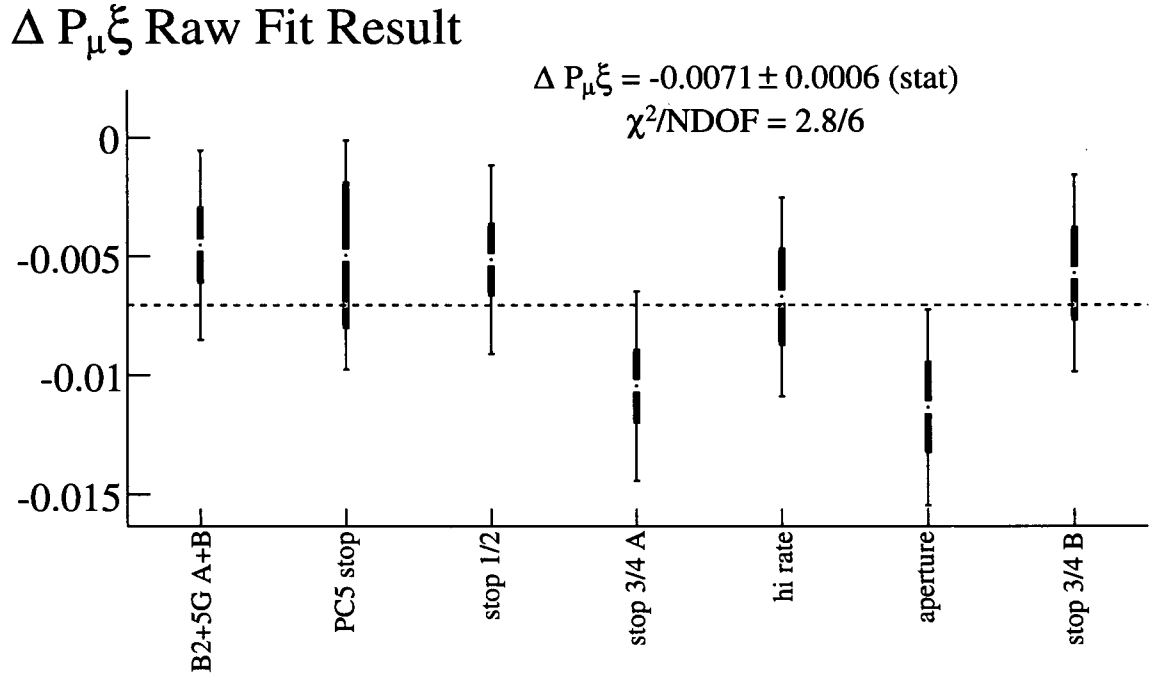

Figure 7.2: $\Delta P_\mu \xi$ from 2004 data to simulation fits, with simulation fringe field of production running.

A number of corrections need to be made to the polarization used in the production simulation. These corrections are for:

1. an error that shifted the beam profiles by one bin (1 mm) which predicts a slightly different correction, on the order of 0.1×10^{-3}, for each simulation beam,
2. ambiguity in the depolarization model choice between Gaussian and exponential depolarization rates (0.0012) described in Section 6.1.4, and
3. using the correct beam characterization for each set (-0.0016 to 0.0025).

The numbers in brackets, in the enumeration of corrections above, is the size and sign of the correction added to $\Delta P_\mu \xi$. For the last item, the production simulation was run without the final beam selection so corrections were needed to use the predicted depolarization for the beam measured for each data set. The largest correction is for an error in the selection of the beam tune to use for Set 32 (PC5 stops). An overall offset in all of the beam depolarization

measurements was due to improvements in the TEC calibrations and analysis. The largest differences were from better rejection of multiple tracks with improvements in the TEC analysis code, and the use of a time-of-flight (TCAP) cut to reject beam positrons which had low efficiency for detection but which could leave enough ionization to register false tracks.

The signs of the corrections were determined by deciding if the correction increased or decreased the predicted polarization in the simulation. Since data to data fits say that the data sets are consistent, taking out the polarization put into the simulation should make the data to simulation fits more consistent as shown in Fig. 7.1. By checking the sign needed to take out the polarization estimated by the simulation, the sign for the corrections was verified.

Table 7.1 gives the raw results of simulation to data fits and the result with corrections applied. A plot of the final corrected values for $\Delta P_\mu \xi$ from the black box value is shown in Figure 7.3. The difference in $P_\mu \xi$ from the black box value is therefore measured to be $(-6.5 \pm 0.6) \times 10^{-3}$. To determine the average difference in $P_\mu \xi$, set to set systematic uncertainties summarized in Table 6.8 were added in quadrature with the statistical uncertainty for each set. The final result is:

$$\Delta P_\mu \xi = (-6.5 \pm 0.6(\text{stat}) \pm 3.8(\text{syst})) \times 10^{-3} \tag{7.1}$$

Set	Description	Raw $\Delta P_\mu \xi$	χ^2/NDOF	Corrected $\Delta P_\mu \xi$
30+31	B2+5G A+B	-4.5 ± 1.5	2007 / 1887	-4.5 ± 1.6
32	PC5 stop	-5.0 ± 3.0	1906 / 1887	-1.3 ± 3.0
35	stop $\frac{1}{2}$	-5.1 ± 1.4	1876 / 1887	-5.3 ± 1.4
36	stop $\frac{3}{4}$ A	-10.5 ± 1.4	1900 / 1887	-10.7 ± 1.3
37	hi rate	-6.7 ± 1.9	1932 / 1887	-7.1 ± 1.9
38	aperture	-11.4 ± 1.8	1896 / 1887	-9.0 ± 1.8
39	stop $\frac{3}{4}$ B	-5.7 ± 1.9	1841 / 1887	-5.9 ± 1.6
	Average	-7.1 ± 0.6		-6.5 ± 0.6

Table 7.1: Table of simulation to data $\Delta P_\mu \xi$ fit results in units of $\times 10^{-3}$. The corrected average has χ^2/NDOF = 3.0/7 when including set to set systematic uncertainties.

Fit residuals are reasonably flat inside the fiducial. Fit residuals for the data set with muons stopping centered in the target are shown in Figure 7.4. Residuals for the fits to the other data sets look identical.

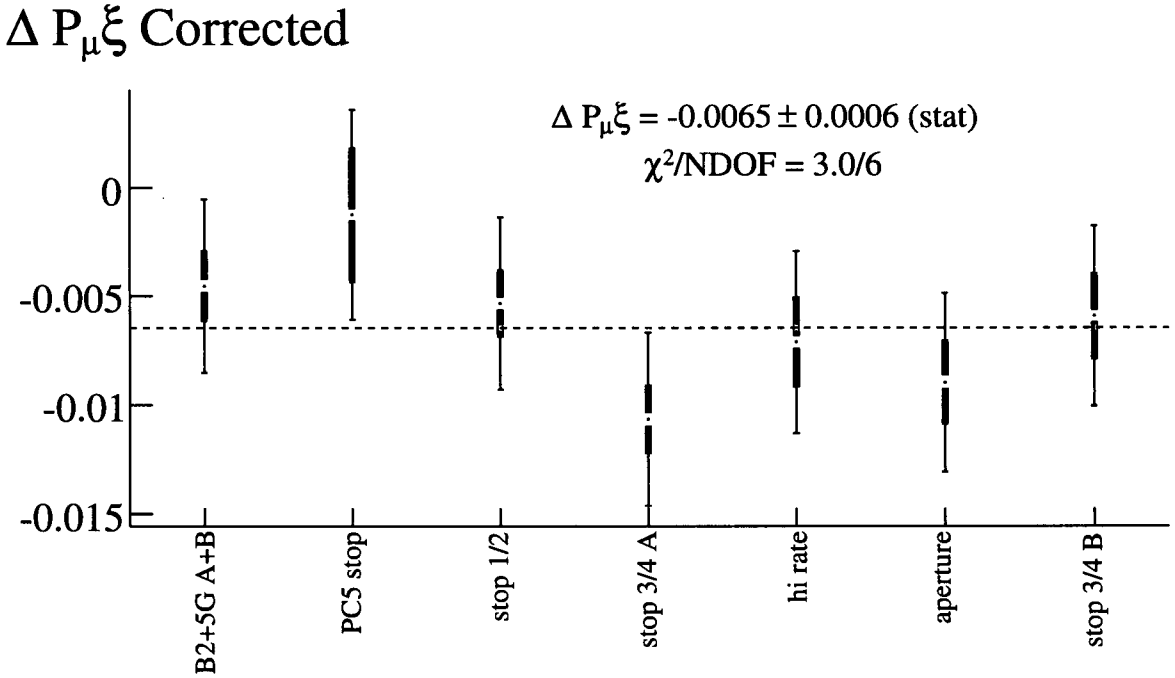

Figure 7.3: $\Delta P_\mu \xi$ from 2004 data to simulation fits, with all of the required corrections applied. The thick red error bars are statistical only, and the longer thin black error bars include the set to set systematic uncertainty added in quadrature with the statistical uncertainty.

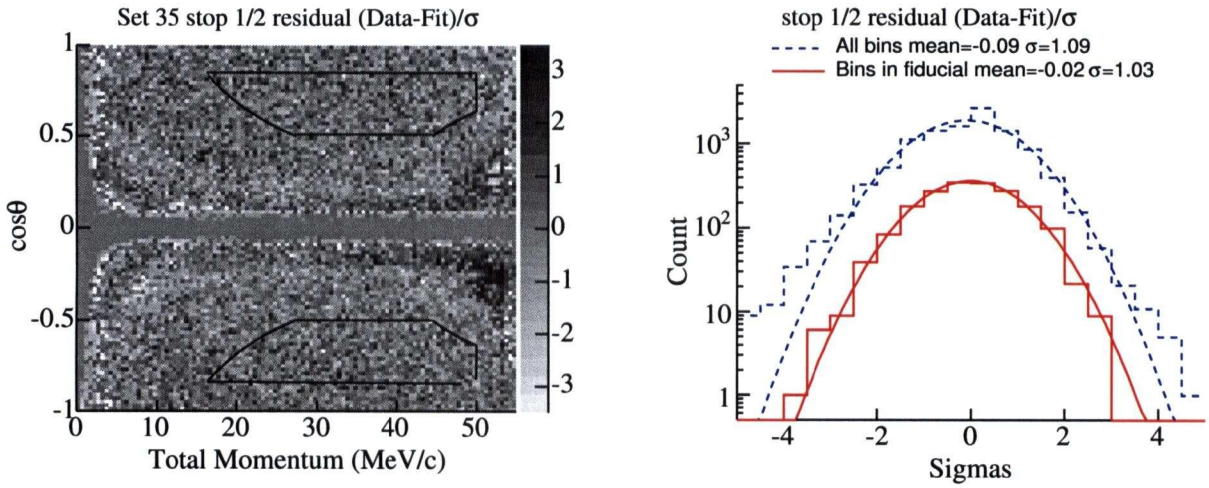

Figure 7.4: Data minus fit residuals, (data-fit)/sigma, for the data set with muons stopping centered in the target. Residuals are plotted for each bin in $\cos\theta$ versus total momentum on the left, and as a histogram on the right. Residuals for the fits to the other data sets look identical.

	ρ	$P_\mu\xi\delta$	$P_\mu\xi$
ρ	1.00	0.31	0.18
$P_\mu\xi\delta$	0.31	1.00	0.41
$P_\mu\xi$	0.18	0.41	1.00

Table 7.2: Correlation coefficients between the spectrum fit parameters.

	ρ	δ	$P_\mu\xi$
ρ	1.00	0.11	0.18
δ	0.11	1.00	-0.56
$P_\mu\xi$	0.18	-0.56	1.00

Table 7.3: Correlation coefficients between the spectrum fit parameters after conversion to the $P_\mu\xi$, δ parameterization.

7.1.2 Blind Fit Results for ρ and δ

Fits to the muon decay spectrum simultaneously measure all of the muon decay parameters. The parameter η was fixed to the black box value, while the values of ρ and $P_\mu\xi\delta$ were allowed to vary to account for the fairly large correlations between the parameters. The correlation coefficients between the fit parameters are shown in Table 7.2. $P_\mu\xi$ is correlated to both ρ and $P_\mu\xi\delta$ making the three parameter fit desirable.

It is interesting to note that when converting the fit results to obtain the value of δ, there is an anti-correlation between $P_\mu\xi$ and δ. This anti-correlation appears because the value of δ comes from the division of the parameters:

$$\delta = \frac{P_\mu\xi\delta}{P_\mu\xi} \tag{7.2}$$

where the quantity $P_\mu\xi\delta$ has a relatively small uncertainty, and $P_\mu\xi$ has a relatively large uncertainty. The correlation coefficients in the parameters, after conversion to the $P_\mu\xi$, δ parameterization, are listed in Table 7.3.

The average difference from the black box value of ρ is $(-5.0 \pm 0.3) \times 10^{-3}$, where the consistency of the ρ values between datasets has $\chi^2/\mathrm{NDOF} = 6.3/7$. The average difference from the black box value of δ is $(10.5 \pm 0.5) \times 10^{-3}$, where the consistency of the δ values between datasets has $\chi^2/\mathrm{NDOF} = 7.1/7$. The uncertainties reported for ρ and δ are statistical only. These data are being re-analyzed by Rob MacDonald with an improved analysis code to extract more precise values for ρ and δ. The analysis improvements are expected to have little effect on the result for $P_\mu\xi$, since the re-analysis cannot fix the uncertainties in the muon polarization. Set to set values of the deviation of ρ and δ from the black box value are listed in Table 7.4.

Set	Description	ρ	δ
30+31	B2+5G A+B	-4.6 ± 0.7	8.8 ± 1.2
32	PC5 stop	-2.6 ± 1.5	9.0 ± 2.4
35	stop $\frac{1}{2}$	-5.8 ± 0.7	11.0 ± 1.2
36	stop $\frac{3}{4}$ A	-5.6 ± 0.7	11.0 ± 1.2
37	hi rate	-4.0 ± 1.0	13.1 ± 1.6
38	aperture	-4.6 ± 0.9	11.6 ± 1.5
39	stop $\frac{3}{4}$ B	-5.5 ± 0.9	8.7 ± 1.5
	Average	-5.0 ± 0.3	10.5 ± 0.5

Table 7.4: Table of simulation to data ρ and δ fit results in units of $\times 10^{-3}$. These values of ρ and δ are from the same fits for $P_\mu \xi$ reported in the previous section.

Description	$\Delta\rho$	$\Delta\delta$	Δ P$_\mu\xi$	χ^2/NDOF
stop $\frac{3}{4}$ to Gaussian	-0.1 $\pm$ 0.9	-1.3 $\pm$ 1.5	1.7 $\pm$ 1.8	1950/1887
stop $\frac{3}{4}$ to exponential	0.9 $\pm$ 0.9	-2.4 $\pm$ 1.5	-0.5 $\pm$ 1.8	2005/1887
stop $\frac{3}{4}$ to Gaus+exp	0.5 $\pm$ 0.7	-1.9 $\pm$ 1.2	0.7 $\pm$ 1.5	1984/1887

Table 7.5: Fit consistency results in units of $\times 10^{-3}$, after using the correct sign correction for Gaussian versus exponential depolarization models.

7.2 Consistency Check and Unblinding

Once the black box is opened, final fits and consistency checks need to be performed. Three re-fits need to be done with $\eta = -0.0036 \pm 0.0069$ to determine the true central values and uncertainty due to η. The values of ρ and δ should come out to be consistent, within 2σ, of the previous *TWIST* measurements of these parameters.

A consistency check will be to generate a new simulation with the muon decay parameters set to the central values measured, but with $\eta = -0.0036$. This simulation will be analyzed with the same analysis and cuts as was done for the simulation that matches one of the data sets. A fit of the resulting simulation decay positron spectrum to the positron spectrum from data should be consistent with zero (within 2σ). If the result is more than 2σ away, another simulation sample will be tried to make sure this was not unlucky.

7.2.1 Consistency Check Results

To obtain zero difference between a data set and simulation, the simulation had to be changed so that no corrections needed to be done at the end. This was done by: adding two equal statistics simulations, one with Gaussian depolarization, and the other with exponential depolarization; using the final beam characterization; and, using an updated simulation with the beam tune shift bug fixed.

The consistency check was done using a simulation to match data set 36, which was the first muon stops at 3/4 data set. The result of the consistency check revealed an error in the sign of the correction for the Gaussian versus exponential depolarization rate. The results in this thesis have been updated to describe and use the correct sign for this correction. The consistency check results, with the correct sign for all of the corrections are summarized in Table 7.5.

7.2.2 Uncertainty due to Eta

Fits with the value of η changed by ± 0.0069 resulted in changes in P$_\mu\xi$ of ± 0.00011. Since this is negligible compared to the systematic uncertainties in this measurement of P$_\mu\xi$, it will be left off the final uncertainty estimate.

7.3 Final Results

The hidden values, of the muon decay parameters, in the simulation were revealed to be: $P_\mu\xi = 1.00678$, $\delta = 0.74218$, $\rho = 0.75440$, and $\eta = 0.00266$. These unblinded values of the muon decay parameters were included in a refit of each data set to the matching simulation set. The final value of $P_\mu\xi$ for each of the data sets included in this analysis is shown in Figure 7.5. The weighted average value of $P_\mu\xi$ is:

$$P_\mu\xi = 1.0003 \pm 0.0006 \text{ (stat)} \pm 0.0038 \text{ (syst)}, \tag{7.3}$$

with a $\chi^2/NDOF$ of 3.0/6. The other muon decay parameters in the fit, ρ and δ, are shown in Figure 7.6. The weighted average value of: ρ from these fits is 0.7493 ± 0.0003 (stat), with a $\chi^2/NDOF$ of 6.3/6; δ from these fits is 0.7526 ± 0.0005 (stat), with a $\chi^2/NDOF$ of 7.1/6. The value of δ is uncomfortably far, 2.2 σ, from a first measurement of δ from *TWIST*. Since this measurement is concerned with $P_\mu\xi$, the fit value for δ is what it is.

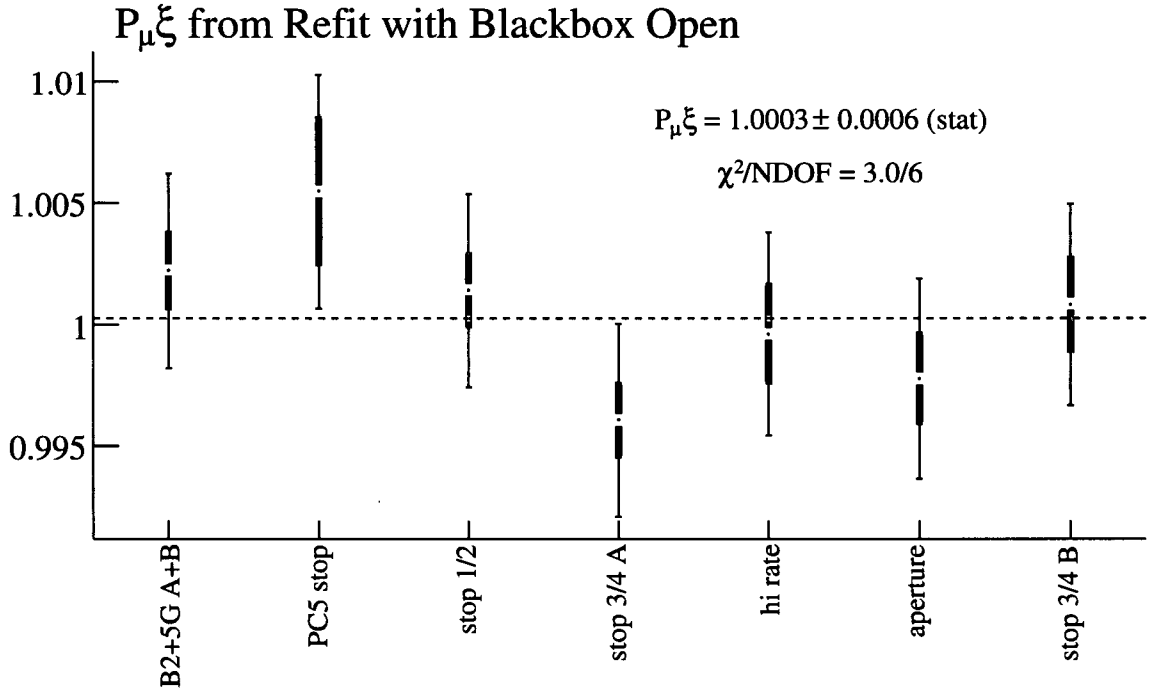

Figure 7.5: $P_\mu\xi$ measured in each of the 2004 data sets. The statistical uncertainty is shown as the thicker red error bars, and the quadratic sum of statistical and set to set systematic uncertainties is shown as the thinner black error bars.

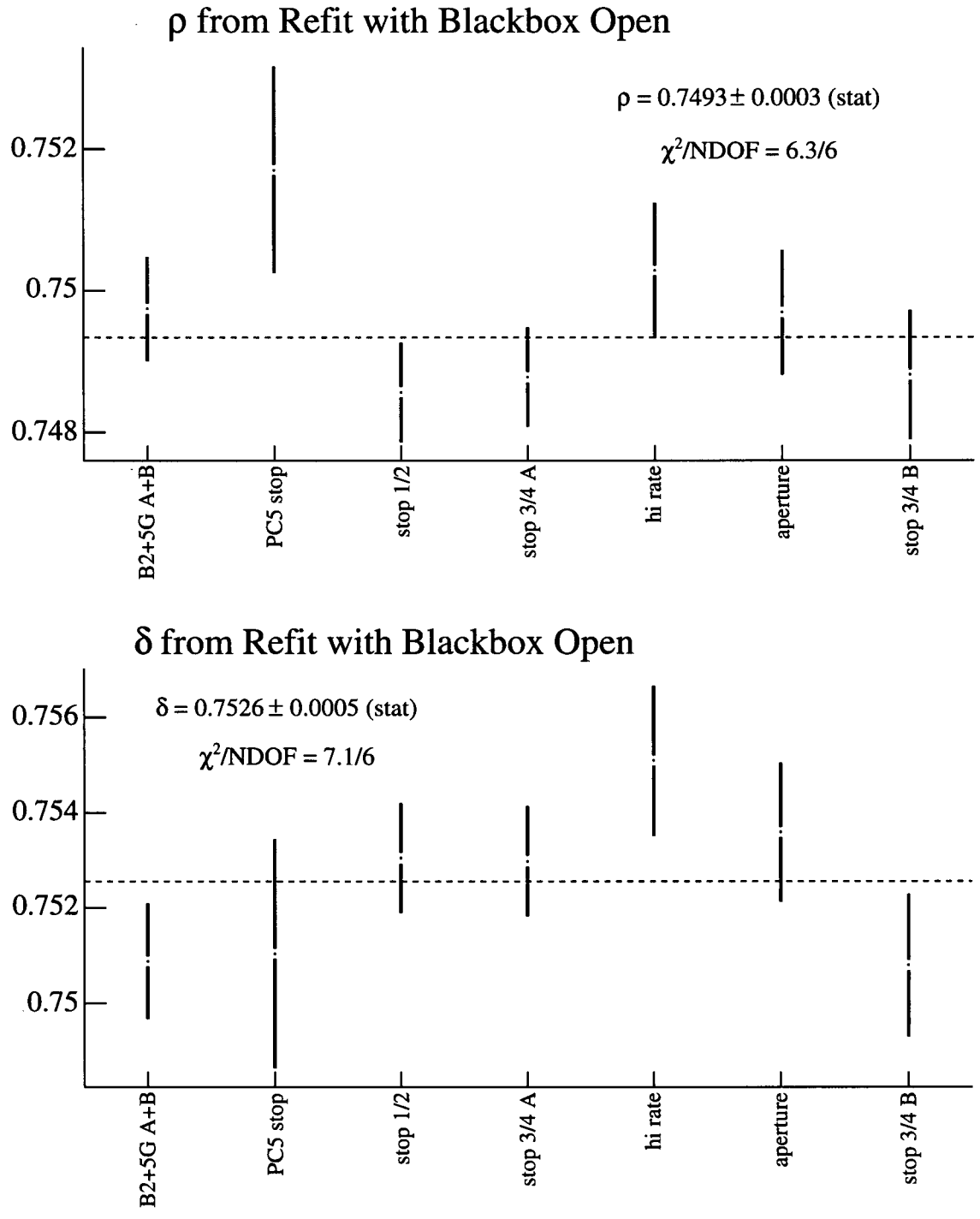

Figure 7.6: The values of ρ are shown in the top plot, and the values for δ are shown in the bottom plot. Only the statistical uncertainty is shown, because the measurements of ρ and δ have not been completed.

7.3.1 Left-Right Symmetric Model Limits

The left-right symmetric models were reviewed in Section 1.7.2. Since a value of $P_\mu\xi$ greater than one has been measured, tighter limits on LRS models have been obtained. The central value slightly greater than one means there are no most likely values of the LRS model parameters, only limits on the values of LRS model parameters can be set. Also, since the measured value of $P_\mu\xi$ is consistent with one, there is no evidence for LRS models or against the Standard Model. Limits on the LRS model parameters, ζ and m_2, are shown in Figure 7.7. These limits are softer than those found by indirect measurements, but at some level are evidence against LRS models.

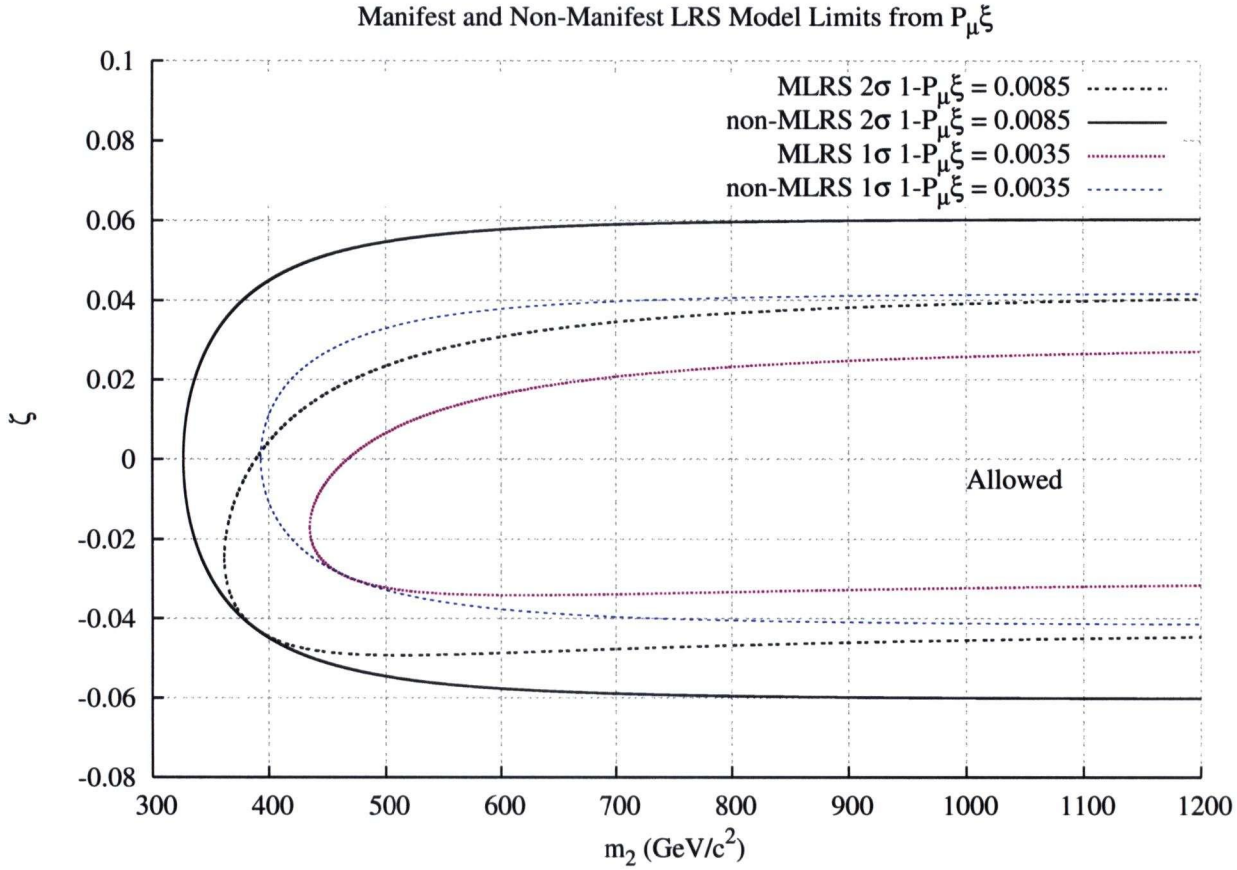

Figure 7.7: LRS model limits on ζ and m_2 from this measurement of $P_\mu\xi$.

Chapter 8

Future Improvements and Conclusion

8.1 Future Improvements

To improve the precision on the measurement of $P_\mu\xi$ the systematic uncertainties on the muon polarization need to be reduced. Improved alignment of the TEC to the solenoid field axis, and to the $\mathcal{TWIST}$ chamber axis should reduce the uncertainty in the fringe field depolarization. More confidence in the polarization estimate will come when the measured changes in polarization, for changes in the muon beam, are reproduced by the same changes made in the simulation.

The second largest systematic uncertainty, which is due to muon depolarization in material can be reduced by better determining the shape of the relaxation versus time. Confirmation that the relaxation is partially due to the muon stops in chamber gas can be investigated by obtaining a larger statistical sample of muon stops in gas. An analysis involving the pulse width from muons in the PC chambers before the muon stopping target may help select muon stop events from target stop events. In addition higher statistics in the simulation will help reduce this uncertainty by $\sqrt{2}$. Another strategy to investigate this systematic uncertainty is to obtain samples of muon stops in different high purity metals.

8.2 Conclusion

The muon decay parameter $P_\mu\xi$ was measured with the $\mathcal{TWIST}$ spectrometer to be 1.0003 $\pm$0.0006(stat) $\pm$0.0038(syst). The uncertainty has been measured to be a factor of two better than a previous direct measurement. The level of uncertainty is similar to that obtained by indirect measurements, and, hence confirms the limits on the mass and mixing angle of a possible W boson coupling to right handed leptons. Rather than a lower limit, which the indirect measurements obtain, this thesis presents a central value for $P_\mu\xi$. No deviation from the standard model prediction is observed.

Bibliography

[1] S. Neddermeyer and C. D. Anderson. *Phys. Rev.* **51**, 884 (1937).

[2] H. Yukawa. *Proc. Phys-Math. Soc. Japan* **17**, 47 (1935).

[3] S.Tomonaga and G.Araki. *Phys. Rev.* **58**, 314 (1940).

[4] M.Conversi, M.Pancini and O.Piccioni. *Phys.Rev.* **71**, 209 (1947).

[5] C.Lattes *et al. Nature* **159**, 694 (1947).

[6] B.M.K. Nefkens and J.W. Price. *The Neutral Decay Modes of the Eta-Meson* (2005), nucl-ex/0202008.

[7] F. Halzen and A.D. Martin, *Quarks & Leptons: An Introductory Course in Modern Particle Physics*, John Wiley & Sons, Inc. (1984).

[8] S. Eidelman et al., *Physics Letters* **B 592**, 1 (2004).

[9] A. Zee, *Phys. Rev.* **D 68**, 093002 (2003).

[10] C.A. Gagliardi *et al.* "Global analysis of muon decay measurements," hep-ph/0509069 (2005).

[11] W. Fetscher and H.-J. Gerber, *Precision measurements in muon and tau decays*, in *Precision tests of the standard electroweak model*, World Scientific, (1995).

[12] I. Beltrami *et al.*, Phys. Lett. **B194**, 326 (1987).

[13] J. Imazato *et al.*, Phys. Rev. Lett. **69**, 877 (1992).

[14] A. Jodidio *et al.*, Phys. Rev. **D34**, 1967 (1986), Phys. Rev. **D37**, 237 (1988).

[15] J.R. Musser *et al.* Phys. Rev. Lett. **94**, 101805 (2005).

[16] A. Gaponenko *et al.* Physical Review **D 71**, 071101(R) (2005).

[17] M. Goldhaber, L. Grodzins, and A. W. Sunyar. *Phys. Rev.* **109**, 1015-1017 (1958).

[18] V. Bargman, L. Michel, and V.L. Telegdi. *Phys. Rev. Lett.* **2**, 435 (1959).

[19] J. D. Jackson. *Classical Electrodynamics – 3rd ed.* John Wiley & Sons, New York (1998).

[20] J. Lindhard *et al.*, Mat.-Fys. Medd. **28**, No. 8 (1954), **33**, No. 14 (1963).

[21] H. H. Anderson and J. F. Ziegler, "Hydrogen Stopping Powers and Ranges in All Elements", The Stopping and Ranges of Ions in Matter, Vol. **3** (1977).

[22] W. H. Barkas and M.J. Berger, "Tables of Energy Losses and Ranges of Heavy Charged Particles", NASA-SP-3013 (1964).

[23] G. W. Ford and C. J. Mullin, "Scattering of Polarized Dirac Particles on Electrons", Phys. Rev. **108**, 477 (1957).

[24] C. K. Iddings *et al.*, Phys. Rev. **135**, 1388 (1964).

[25] V. L. Lyuboshits, "Depolarization of fast particles travelling through matter", Sov. J. Phys. **32**, 362 (1980). V. L. Lyuboshits, "Spin rotation associated with the deflection of a relativistic charged particle in an electric field", Sov. J. Nucl. Phys., **31**, 509 (1980).

[26] P. Depommier, "Muon depolarization in multiple scattering", *TWIST* Technical Note 100 (2005).

[27] P. Herczeg, Phys. Rev. **D34**, 3449 (1986).

[28] B. Kayser, F. Gibrat-Debu, F. Perrier, "The Physics of the Massive Neutrinos", World Scientic, Singapore (1989).

[29] Y. Fukuda *et al.* [Super-Kamiokande Collaboration], Phys. Rev. Lett. **81**, 1562 (1998), hep-ex/9807003.

[30] M. C. Sanchez *et al.* [Soudan 2 Collaboration], Phys. Rev. D **68**, 113004 (2003), hep-ex/0307069.

[31] M. Ambrosio *et al.* [MACRO Collaboration], Phys. Lett. B **566**, 35 (2003), hep-ex/0304037.

[32] E. Aliu *et al.* [K2K Collaboration], Phys. Rev. Lett. **94**, 081802 (2005), hep-ex/0411038.

[33] B. T. Cleveland *et al.*, Astrophys. J. **496**, 505 (1998).

[34] M. Altmann *et al.* [GNO Collaboration], Phys. Lett. B **490**, 16 (2000), hep-ex/0006034.

[35] J. N. Abdurashitov *et al.* [SAGE Collaboration], J. Exp. Theor. Phys. **95**, 181 (2002), astro-ph/0204245.

[36] S. Fukuda *et al.* [Super-Kamiokande Collaboration], Phys. Lett. B **539**, 179 (2002), hep-ex/0205075.

[37] S. N. Ahmed *et al.* [SNO Collaboration], Phys. Rev. Lett. **92**, 181301 (2004), nucl-ex/0212021.

[38] R.S. Henderson *et al.* Nucl. Instr. and Meth. A **548**, 306-335 (2005), hep-ex/0409066.

[39] Opera3D simulation software, http://www.vectorfields.com/.

[40] C. Boucher-Veronneau, "The TWIST Solenoid Magnetic Field", TWIST Co-op student report,

`https://twist.phys.ualberta.ca/forum/view.php?bn=twist_papers&key=1091051979`

(2004).

[41] G. Marshall, Private Communication, TRIUMF (2005).

[42] Y. Davydov *et al.*, Nucl. Instr. and Meth. **A461**, 68 (2001).

[43] S. Fotoohi, "The TWIST Solenoid Magnetic Field", Co-op student report (2005).

[44] C.J. oram *et al.*, Nucl. Instr. and Meth. **179**, 95 (1981).

[45] R. Veenhof, *GARFIELD.* Version 7.10.

[46] G. Sheffer, Private Communication, TRIUMF (2005).

[47] R. Poutissou *et al.*, Proceedings of the 13th IEEE-NPSS Real Time Conference 2003, Montreal, QC, (2003).

[48] A. Gaponenko. "A Precision Measurement of the Muon Decay Parameter Delta", Ph.D. thesis, University of Alberta (2005).

[49] F. James, "Fitting tracks in wire chambers using the Chebyshev norm instead of least squares," *Nucl. Instr. Meth.* **211**, 145 (1983).

[50] G. Lutz, "Optimum track fitting in the presence of multiple scattering," *Nucl. Instrum. Meth.* **A273**, 349 (1988) .

[51] R. Brun *et al.*, *GEANT3 Users Guide, CERN Program Library W5013* (1994). Version 3.21/14 (2002).

[52] R. E. Behrends, R. J. Finkelstein, and A. Sirlin. "Radiative corrections to decay processes," Phys. Rev. **101**, 866 (1956).

[53] S. M. Berman. "Radiative corrections to muon and neutron decay," Phys. Rev. **112**, 267 (1958).

[54] A. B. Arbuzov. "First-order radiative corrections to polarized muon decay spectrum," Phys. Rev. **112**, 267 (2002).

[55] A. Abrbuzov, A. Czarnecki, and A. Gaponenko, "Muon decay spectrum: Leading logarithmic approximation," Phys. Rev. **D65**, 113006 (2002), hep-ph/0202102.

[56] A. Arbuzov and K. Melnikov, "Corrections to electron energy spectrum in muon decay," Phys. Rev. **D66**, 093003 (2002), hep-ph/0205172.

[57] A. Arbuzov, "Higher order QED corrections to muon decay spectrum," JHEP **03**, 063 (2003), hep-ph/0206036.

[58] A.B. Arbuzov, "Virtual and soft pair corrections to polarized muon decay spectrum," JETP Lett. **78**, 179 (2003), hep-ph/0301114.

[59] V. Selivanov, "Accurate GARFIELD calculations of DC4 at B=0," *TWIST* Technical Note 81, TRIUMF (2003).

[60] K. Olchanski, "Tuning of GEANT ionization clustering to data" (2003). *TWIST* internal communication, the General forum, key=1053913884.

[61] P. Gumplinger, "Private Communication", September 2005.

[62] R. Barlow. "Systematic Errors: facts and fictions" (2002), hep-ex/0207026.

[63] Brewer, Jess. Private Communications. University of British Columbia (2002).

[64] J. Korringa, Physica **16**, 601 (1950).

[65] A.Abragam, The Principles of Nuclear Magnetism, Oxford, 355 (1961).

[66] S.F.J. Cox *et al.* Physica B **594**, 289 (2000).

[67] R.S. Hayano *et al.* Phys. Rev. B **20**, 850 (1979).

[68] E.W. Collings, F.T. Hedgcock, Phys. Rev. **126**, 1654 (1962).

[69] O. Hartmann *et al.* Phys. Rev. B **37**, 4425 (1988).

[70] W. Schilling, Hyperfine Int. **4**, 636 (1978).

[71] D.C. Brice, Phys. Lett. A **66**, 53 (1978).

[72] L. Michel, Proc. Phys. Soc. **A63**, 514 (1950).

[73] C. Bouchiat and L. Michel, Phys. Rev. **106**, 170 (1957).

[74] T. Kinoshita and A. Sirlin, Phys. Rev. **108**, 844 (1957).

[75] W. Fetscher, H.-J. Gerber, and K.F. Johnson, Phys. Lett. **B173**, 102 (1986).

[76] P. Langacker and S.U. Sandar, Phys. Rev. **D40**, 1569 (1989).

[77] E. Frlež *et al.*, Phys. Rev. Lett. **93** 181804 (2004).

[78] G. Prézeau *et al.*, hep-ph/0409193.

[79] J. Peoples, Columbia University, thesis, Nevis Report No. 147 1966 (unpublished).

[80] B.A. Sherwood, Phys. Rev. **156**, 1475 (1967).

[81] D. Fryberger, Phys. Rev. **166**, 1379 (1968).

[82] S.E. Derenzo, Phys. Rev. **181**, 1854 (1969).

[83] F. Liu, Texas A&M University, thesis, 1994 (unpublished).

[84] [Los Alamos TPC experiment proposal]

[85] H. Burkard *et al.*, Phys. Lett. **160B**, 343 (1985).

[86] N. Danneburg *et al.*, Phys. Rev. Lett. **94**, 021802 (2005).

[87] B. Balke *et al.*, Phys. Rev. **D37**, 587 (1988).

[88] J. R. Musser. "Measurement of the Michel Parameter rho in Muon Decay", Ph.D. thesis, Texas A&M University, (2005).

[89] S. Sakata and K. Inoue. *Proc. Phys-Math. Soc. Japan* **24**, 843. 1942.

[90] R.E. Marshak and H.A. Bethe. *Phys.Rev.* **72**, 506. 1947.

Appendix A

Personal Contributions to $\mathcal{TWIST}$

This thesis described all aspects of $\mathcal{TWIST}$ experiment, and in this appendix I will describe the specific contributions that I have made to the design, construction and operation of $\mathcal{TWIST}$, as well as the detailed data analysis leading to an improved determination of $P_\mu\xi$.

A.1 Contributions to Design and Building

I began my Ph.D. working on $\mathcal{TWIST}$ during the final stages of the construction of the $\mathcal{TWIST}$ spectrometer. My contributions at this stage included wrapping cables, preparing cathode foil frames for gluing, and the stretching and gluing of chamber foils. I helped design and wire the trigger electronics before the first data were collected with $\mathcal{TWIST}$.

A.2 Contributions to Operation of $\mathcal{TWIST}$

During the collection of the data presented in this thesis, I took shifts running the experiment, acted as the run coordinator, and was one of the experts on the gas system operation. At the beginning of the running period I helped find and correct various electronics problems, and updated the map files which relates the TDC slot and channel numbers to the physical plane and wire numbers.

A.3 Contributions to Analysis of $\mathcal{TWIST}$ Data

My contributions to the $\mathcal{TWIST}$ simulation include code to produce realistic muon beam profiles, code to simulate different muon depolarization in material versus time, and code to investigate muon beam collimators.

In the $\mathcal{TWIST}$ analysis code, I developed and validated the pattern recognition code used in this thesis to select muon decay events. I developed the asymmetry versus decay time analysis to investigate material dependent depolarization. I was responsible for the generation of the simulation data, and the processing of both the simulation and real data on the Westgrid cluster, using scripts developed by other $\mathcal{TWIST}$ participants. Part of this responsibility involved ensuring that the data were of sufficient quality by looking at the detailed time histories of various quantities, and checking the validity of the calibration files used for the analysis of these data.

Since this analysis was the basis of my thesis, I worked on many other small jobs that were required to complete this $P_\mu\xi$ analysis.